MICROPOROUS MEMBRANES FOR OIL-WATER SEPARATION AND DESALINATION

By

DIAKO MAHMODI

Bachelor of Science in Chemical Engineering
Amir Kabir University of Technology
Tehran, Iran
2009

Master of Science in Chemical Engineering
Razi University
Kermanshah, Iran
2011

Submitted to the Faculty of the
Graduate College of the
Oklahoma State University
in partial fulfillment of
the requirements for
the Degree of
DOCTOR OF PHILOSOPHY or EDUCATION
December, 2022

MICROPOROUS MEMBRANES FOR OIL-WATER

SEPARATION AND DESALINATION

Dissertation Approved:

Dr. Seokjhin Kim

Dissertation Adviser

Dr. Alan Tree

Dr. Joshua D. Ramsey

Dr. Mark Krzmarzick

ACKNOWLEDGEMENTS

Foremost, I would like to express my sincere gratitude to my advisor Dr. Seokjhin Kim for the continuous support of my Ph.D. study and research, and for his patience, motivation, and enthusiasm. His guidance helped me in all the time of research and writing of this thesis. I want to extend my gratitude to the Faculties in the Department of Chemical Engineering for sharing their immense knowledge through the coursework.

Besides my advisor, I would like to thank the rest of my committee members: Profs Alan Tree, Joshua D. Ramsey, and Mark Krzmarzick, for their encouragement, insightful comments, and hard questions.

I thank my fellow lab mates in Kim's Research group: Shailesh Dangwal and Anil Ronte for the exciting discussions, for the sleepless nights we were working together before deadlines, and for all the fun we have had in the last four years. In addition, I would like to thank my friends at OSU: Saeed Manouchehri, Anirban Ghosh, and Sushobhan Pradhan.

Last but not the least, I would like to thank my family: my mom and siblings, for their tremendous support. I would not have achieved any of my degrees without the immeasurable sacrifices they made and the support they gave me.

I dedicate my dissertation to #Mahsaamini in solidarity with all brave Iranian women and men who fight for freedom. Women, Life, Freedom (ژن، ژیان،ئازادی)

Name: DIAKO MAHMODI

Date of Degree: DECEMBER, 2022

Title of Study: MICROPOROUS MEMBRANES FOR OIL-WATER SEPARATION AND DESALINATION

Major Field: CHEMICAL ENGINEERING

Abstract: Water supply sustainability is one of the biggest challenges of the century, necessitating efficient and economical technologies for water purification. One of the most critical technologies in our world is filtration because it tremendously helps to tackle water scarcity issues. Conventional filtration technologies such as distillation, condensation, coagulation, and adsorption are demanding energy and their operational conditions are complicated. Therefore, it is necessary to explore a cost-effective and energy-efficient method for the filtration process. Membrane-based water treatment technology is a promising technique because of its efficiency in terms of cost and separation performance. However, the membranes are suffering from fouling phenomena and fabricating membranes with fouling-resistance properties is important. In the first study, NaA zeolite was fabricated on a stainless steel mesh by secondary growth method through optimizing aluminum/silicon ratio (ASR) to effectively separate oily water. The NaA zeolite-coated mesh was tested for various oils, including olive oil, mineral oil, and diesel to assess the effect of the type of oil on oil/water separation efficacy. In the second study, ZnO atomic layer deposition (ALD) modified membranes were developed for treating produced water. ZnO ALD coating helped improve membrane hydrophilicity and antifouling property and reduced the roughness and pore size of the membranes by improving hydrophilicity and decreasing roughness. In the third study, mixed matrix membranes were developed by embedding hydrophilic nanoparticles (MIL-101(Cr)-NH2) into cellulose acetate (CA) matrix to enhance hydrophilicity to treat dye/salt solution. This helped counter fouling problems that membranes face when used to treat industrial wastewater by enhancing hydrophilicity. In the fourth study, super hydrophilic silica nanoparticles (Si NPs) were used to modify tubular α-alumina membranes to improve their performance in terms of flux, oil rejection, and antifouling properties. The prepared membranes were applied for oil/water emulsion treatment. The Si NPs leaching decreased from the surface of the α-alumina tubular membrane by using polyvinyl alcohol (PVA) as a pre-treatment step. By coating Si NPs, the surface roughness decreased, leading to lower fouling since traps on the membrane surface for containment decreased with decreasing membrane roughness.

TABLE OF CONTENTS

Chapter Page

Chapter Page

LIST OF TABLES

Table Page

LIST OF FIGURES

Figure Page

Figure Page

Figure Page

CHAPTER I

INTRODUCTION

The availability of clean water has been an important issue around the globe. The safety and maintenance of clean water sources are critical to the environment, societal concerns, and to human health. Oil spills attract the attention of the public because of their negative impact on human health, the environment, and regional economics [1]. Consequently, the development of oil/water separation technology has been a worldwide goal and challenge [2]. Various methods for water purification have been proposed, such as coagulation, adsorption, air flotation, and sorption [3-5]. However, these methods have drawbacks, such as high cost, large machinery, and low efficacy [6, 7]. Membranes have been widely used in oil-water separation and desalination (the process by which the dissolved mineral salts in water are removed) due to their high separation capability and facile operation conditions [8, 9]. Micro/nano and ultra-filtration membranes have also been utilized for water treatment [10]. Typically, microporous membranes, regardless of their construction, suffer from fouling, which reduces the permeation efficiency. Membrane fouling is a process by which the particles, colloidal particles, or solute macromolecules are deposited or adsorbed onto the membrane pores or onto a membrane surface by physical and chemical interactions or mechanical action, which results in smaller or blocked membrane pores.

Although membranes are attractive due to their effective selectivity, affordable cost, easy handling, and low energy consumption, the membranes are prone to fouling by natural organics, proteins, and biofilms and corresponding decreases in flux over time. To remove foulants on the membrane surface, chemical rinsing is a proposed remedy, but the strong chemical can damage the membrane structure and decrease its lifetime [10]. Generally, there are two major categories of membrane materials: Organic (polymeric), and inorganic (ceramic) materials. Organic membranes are composed of modified organic polymers, while inorganic membranes are ceramic and metals-based [13]. Inorganic membranes have shown excellent thermal and chemical stability compare to polymeric membranes, and as well as greater fouling-resistant properties due to the inherent hydrophilic of inorganic material [14].

Although polymer membranes have exhibited lower resistance to higher temperatures and harsh chemicals than inorganic membranes, they have been widely used for wastewater treatment due to their facile preparation, lower cost, lower energy requirement, and flexibility in membrane configuration [15]. Currently the local governing bodies or industries are using membrane technology for water filtration [15]. The current membranes have high energy requirements and require chemical usage for cleaning. The chemical usage increases the hazardous toxic material release to the environment [15]. The current work is about treatment of oil-in-water emulsion and dye/salt solution using ceramic and polymeric membranes, respectively. Significant efforts have been made to reduce membrane fouling [16-19]. For instance, Ju et al. [16] synthesized the fouling-resistant poly (ethylene glycol) diacrylate (PEGDA) membrane for oil/water separation. This membrane showed higher permeation and lower oil fouling than uncoated polysulfone (PSF) ultrafiltration membranes. Although water permeability increased from 10 to 150 L μm/ (m2 h bar), the prepared polymeric membranes were not tolerated for harsh environmental conditions such as acidic, basic, and hot solutions [17]. Vatanpour et al. [20] improved the cellulose acetate (CA) membrane by incorporating ZnO graphitic carbon nitride nanocomposite to obtain pure water flux

(PWF) of 51.3 LMH, which was 2.1 times greater than pristine CA at same given driving force, while demonstrating highest rejection rate for synthetic textile wastewater containing Blue 3R dye. Although, the modified cellulose acetate (CA) membrane showed lower fouling ratio than the pristine cellulose acetate (CA), the membranes were applied only for one synthetic textile wastewater containing Blue 3R dye with high molecular weight (789.4 Da). The synthetic textile wastewater could not be a perfect model for real textile wastewater since it contains dyes with lower molecular weight that effect immensely the performance of membranes in terms of dye rejection and antifouling properties.

In Aim I, NaA zeolite was coated on a stainless steel mesh by secondary growth method through optimizing aluminum/silicon ratio (ASR) to effectively separate oily water. Zeolite membranes have attracted significant attention due to their high surface area, unique molecular sieving properties, and various pore sizes [21, 22]. Zeolites consist of aluminum, oxygen, and silicone with tetrahedral crystalline framework, which produces discrete pore sizes [23]. In addition to that, zeolite membranes are inherently hydrophilic which results in lower oil fouling. Hydrophobic membranes are intrinsically vulnerable to oil fouling since hydrophobic materials are prone to adsorbing on the membrane surface due to their oleophilic properties [24, 25]. Using hydrophilic-material-coated meshes for oil/water separation is promising because they repel oil droplets and facilitate the removal of oil foulants. Materials such as hydrogel [26], ZnO [27], and TiO2 [28, 29] have been coated on meshes to enhance hydrophilicity for oil/water separation. In spite of the aforementioned membranes' high oil rejection efficiencies, their structures are not compatible in hot, acidic, and basic solutions [30, 31]. Zeolite membranes are favorable because of their chemical, mechanical, thermally stable, and corrosion resistant properties [32].

In Aim II, ZnO atomic layer deposition (ALD) membranes were prepared for treating produced water. The ALD technique improved membrane hydrophilicity and reduced the roughness and pore size of the membranes. The applicable methods to endow hydrophilicity are hydrophilic

nanoparticle coatings, such as TiO_2 [33], Al_2O_3 [34], SiO_2 [35], graphene oxide [36], zeolite [37], and Fe_3O_4 [38] on the surface and inside the pores of the membrane. However, it is worth mentioning that such coatings can suffer from agglomeration that drastically decreases the performance of the membranes [39]. Alternatively, surface modification methods have been utilized, such as plasma treatment [40], dip coating [41], surface grafting [42], interfacial assembly [43], and surface deposition [44]. However, these traditional modification methods suffer from low stability, fragile membrane structure, restricted suitable substrates, and non-uniform surface [45]. To overcome such issues, atomic layer deposition (ALD) has emerged as a promising tool to fabricate membranes with controllable pore size and uniform structures. ALD has three advantages over conventional methods. First, the ALD process is compatible with a wide range of substrates [45]. Second, ALD generates a uniform coating over uneven supports, which not only keeps the original pore structure of the support but also reaches complete coverage [45]. Third, ALD allows for unprecedented control of the thickness of the coating, and can be tuned from nanometers to micrometers [45, 46].

In Aim III, superhydrophilic silica nanoparticles (Si NPs) were coated on tubular α-alumina membranes to improve their performance in terms of flux, oil rejection, and antifouling properties. Membranes made out of ceramic materials such as alumina, zirconia, titania, and silica have attracted far more attention than other materials because of their biological stability and thermal, chemical, and mechanical resistances [47-49]. Alumina membranes are highly chemically inert and thus can be employed in over a wide pH range [50]. Muller et al. [51] applied an α-alumina membrane with a pore size of 0.8 μm for oil/water emulsion separation with oil droplet size and concentration of 4 μm and 250 ppm, respectively. Muller et al. reported stable permeability and a rejection rate of 30 L m^{-2} h^{-1} bar^{-1} and 30 %, respectively [51]. Hua et al. [52] studied the performance of α-alumina membrane with a 50-nm pore size for oily wastewater treatment with a

a500 ppm oil concentration. The results showed stable permeability and rejection rate of 63.9 L m^{-2} h^{-1} bar^{-1} and 98.1%, respectively [52].

Grafting and coating are two commonly used methods for modifying membranes to improve their fouling properties and enhance the efficiency of operation [53]. Zhang et al. grafted a Zwitterionic monolayer onto an α-alumina ceramic membrane, which immensely improved its flux and antifouling properties for O/W emulsion separation [54]. The main disadvantage of hydrophobic coatings is the rapid increase in membrane fouling resulted in high tendency of oil component to deposit on hydrophobic surface, which stops the filtration process and leads to a rise in operational costs [52]. Although anti fouling membranes were synthesized using coating hydrophilic nanoparticles for oil/water emulsion, there is a gap to study nanoparticles leaching from membrane surface during oil water filtration operation. This work describes the effects of modifying α-alumina membranes with different loadings of hydrophilic fumed Si NPs to improve the hydrophilicity of the membranes and increase their performance characteristics. In addition, Si NPs leaching from surface of the α-alumina membranes were studied.

In Aim IV, modified cellulose acetate (CA) membranes were prepared by embedding hydrophilic MIL-101 (Cr)-NH2 nanoparticles into cellulose acetate (CA) matrix to enhance its hydrophilicity to treat dye/salt solution. Among various polymers, cellulose acetate (CA) is one of the most commonly utilized polymers due to its unique specification such as high selectivity, low cost, outstanding biocompatibility, durability, thermal stability, and abundance in nature [55, 56]. CA is somewhat hydrophilic due to hydroxyl groups in its structure, providing better film-forming and oleophobic properties [57, 58]. This template is best used for directly typing in your content. However, you can paste text into the document, but use caution as pasting can produce varying results. Although CA shows some hydrophilic property, membrane fouling regarding CA is still considered one of the biggest issues because of inadequate hydrophilicity allowing solute

molecules to stick to the surface. Therefore, membrane modification is necessary to enhance membrane performance [11, 12].

Fouling in NF membrane is the major challenge limiting their application in large scale. Making membrane more hydrophilic is found to be an effective way to mitigate fouling, hence not drastically reducing flux. Polymer blending, where hydrophilic nanoparticles are directly mixed into the polymer matrix is a facile technique applied for membranes preparation that is easily implemented in the current commercial fabrication techniques [13].

To improve hydrophilicity, nanoparticles are embedded into the polymer blend, called mixed-matrix membranes, which help improve membrane performance such as permeability, and fouling-resistant property, increasing membrane longevity [14, 15]. Organic nanoparticles are a promising alternative because of their higher interaction with polymers, which could be attributed to ample hydrophilic functional groups in them. These hydrophilic groups enhance hydrophilicity and fouling-resistant of the prepared membranes. These nanoparticles include metal-organic framework [16], chitosan [17], polystyrene [18], and polydopamine [19].

Aim I: Fabricate zeolite membranes with tunable hydrophilicity for oil-water mixture separation.

Significance: NaA zeolite-coated membranes with tunable hydrophilicity were prepared using a secondary growth method and used for high-level oil/water separation and then calculate and test the zeolite-based membranes to evaluate the oil/water separation efficiency, reusability, regenerability, and stability.

The strategies are listed below followed by an illustration of the synthetization of the NaA zeolite coated mesh, shown in Figure 1.1.

Task 1: NaA zeolite membranes preparation by secondary growth method through optimizing aluminum/silicon ratio (ASR).

Task 2: Characterization of NaA zeolite membranes.

Task 3: Study performance of the fabricated membranes by measuring oil rejection rate and flux.

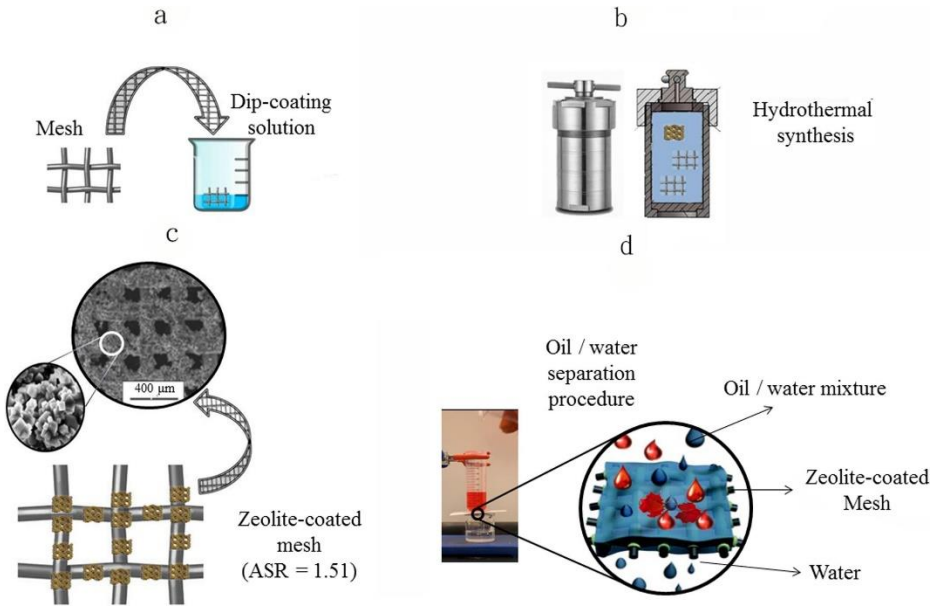

Fig. 1.1 Schematic illustration of the synthetization of the NaA zeolite coated mesh (a) dip-coating, (b) hydrothermal synthesis, (c) zeolite-coated mesh, and (d) oil/water separation procedure.

Aim II: Improving antifouling property of alumina microfiltration membranes by using atomic layer deposition technique for produced water treatment.

Significance: ALD technique as a new approach was utilized to develop ZnO-coated alumina membranes with tunable hydrophilicity. ALD membranes were fabricated with a different number of ALD cycles, and performance parameters like pure water flux, total organic carbon (TOC) rejection, and anti-fouling property will be investigated. As shown in Fig. 1.2, nitrogen was used as a carrier gas and DI water as the oxidizer and diethylzinc, Zn(C2H5)2, (Strem Chemicals Inc., >95%, Newburyport, MA, USA) as the Zn source. Samples were prepared with 20, 40, 60, 80, 100 and 120 cycles. The ZnO ALD reaction as the following,

$$Zn\,(C_2H_5)_2 + H_2O\,(g) \longrightarrow ZnO + 2C_2H_6\,(g)$$

The tasks are listed below followed by the schematic of membrane coating process using ALD technique.

Task 1: Improved the pristine α-alumina membrane by coating ZnO using the ALD technique.

Task 3: Characterization of the ZnO ALD membranes.

Task 2: Study the anti-fouling property of the prepared membranes.

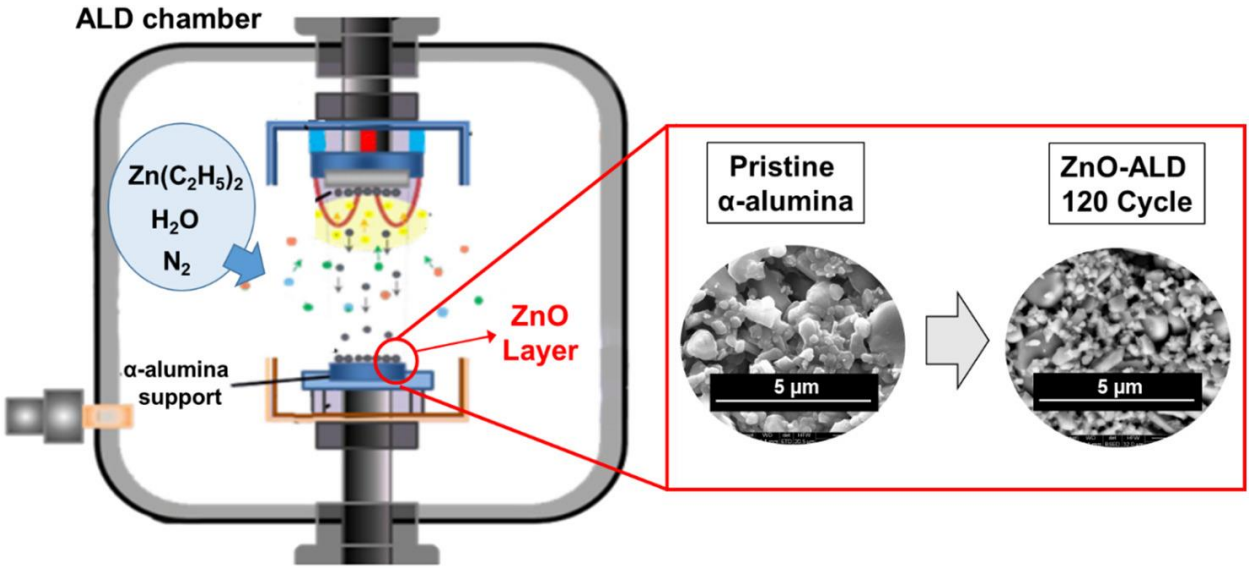

Fig. 1.2 Schematic of membrane coating process using ALD technique.

Aim III: Improving cellulose acetate (CA) mix matrix membranes by incorporating hydrophilic MIL-101-NH_2 nanoparticles for treating dye/salt solution.

Significance: Mixed matrix membranes were developed by embedding hydrophilic nanoparticles (MIL-101 (Cr)-NH2) into cellulose acetate (CA) matrix to enhance hydrophilicity. The major goals of this study are mentioned as follows: (1) To achieve enhanced efficiency and antifouling properties of synthesized membranes; (2) To synthesize new CA/MIL-101(Cr)-NH_2 membranes utilizing phase inversion; (3) To determine the optimal concentration of synthesized

nanoparticles (MIL-101(Cr)-NH2), which were incorporated in the CA matrix. Figure 1.3. exhibited the CA/MIL-101(Cr)-NH_2 membranes preparation steps using the phase inversion technique. First, a certain amount of the fillers (0.01, 0.05, 0.1, 0.2, 0.5, and 1 wt.%) relative to the CA were added to DMF and the solution sonicated for 30 min. Next, PEG (3 wt.%) and the CA (18 wt.%) were loaded into the solution by stirring at 30 °C for 24 h.

The resulting membrane sheets were immediately immersed in a distilled water bath as nonsolvent at room temperature. After coagulation, the resulted membranes were rinsed and placed in fresh distilled water until tested.

The three tasks are listed below followed by an illustration of CA/MIL-101(Cr)-NH_2 membrane preparation steps as shown in Figure 1.3.

Task 1: Synthesizing MIL-101(Cr)-NH_2 nanoparticles and CA/MIL-101 (Cr)-NH_2 membranes using the phase inversion method.

Task 2: Characterization of MIL-101(Cr)-NH_2 nanoparticles and the prepared membranes.

Task 3: Study the performance of the prepared membranes for treating salt/dye solution.

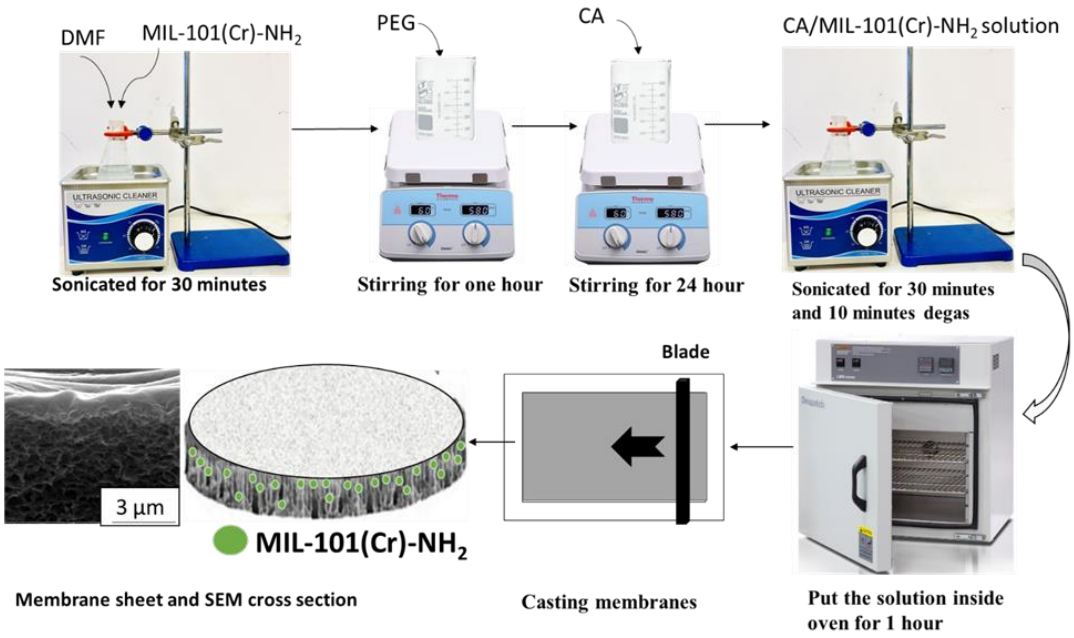

Fig. 1.3 CA/MIL-101(Cr)-NH_2 membrane preparation steps.

Aim IV: Improving antifouling property of alumina tubular microfiltration membranes by coating hydrophilic silica nanoparticles for oil/water emulsion treatment.

Significance: Super hydrophilic silica nanoparticles (Si NPs) was coated on tubular α-alumina membranes to improve their performance in terms of flux, oil rejection, and antifouling properties. Initially, the α-alumina tubular membrane was washed with DI water to remove dust and pollutants and then dried in an oven at 60 °C overnight. A coating solution was prepared by dispersing the hydrophilic silica NPs into deionized water and stirred for two hours to form a homogeneous silica-NPs solution at various weight percentages of 0.25%, 0.5%, 1%, and 3%. Before coating Si NPs on the surface of the α-alumina tubular membrane, a pre-treatment process was applied using a PVA solution. For the pre-treatment process, as shown in Fig. 1.4a and b, the α-alumina tubular membrane was immersed in 10 wt.% PVA solution [20] and then dried in the oven at 60 °C overnight, respectively. The pre-treatment process was repeated several times to make sure most of the void and vacant sites of the pristine α-alumina tubular membrane were filled with PVA. Fig. 1.4c shows that the pre-treated membranes were then immersed in Si NPs solution at various weight

percentages of 0.25%, 0.5%, 1%, and 3% several times and dried for a day. Finally, as exhibited in Fig. 1.4d, the fabricated membranes were then calcinated at 550 ºC for 3 hours to remove PVA (PVA melting point is 200 °C) and form mesoporous Silica coated membranes.

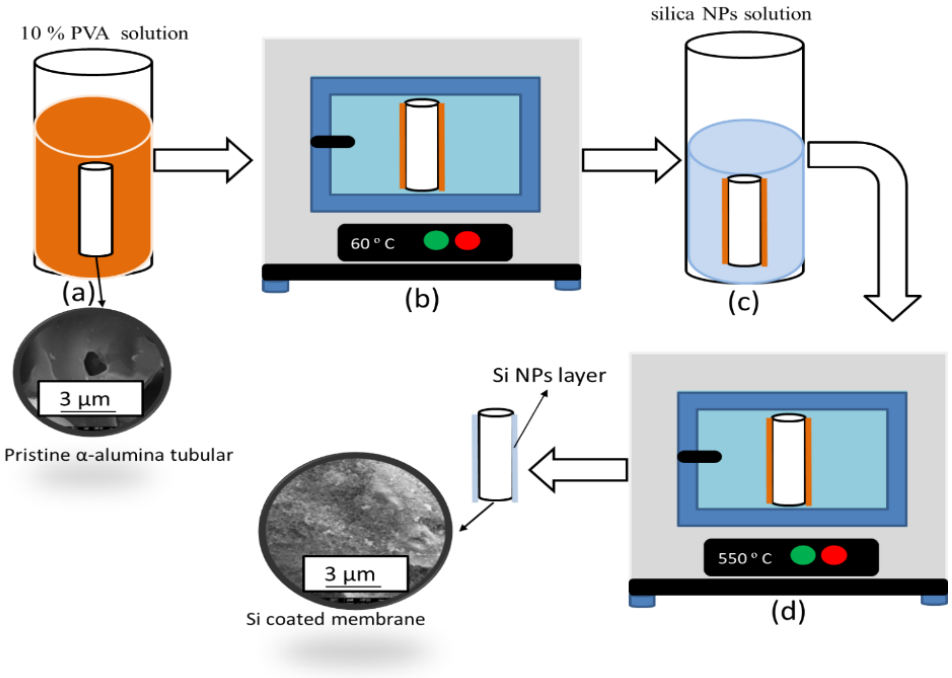

Fig. 1.4 The schematic of the Si NPs coating on α-alumina tubular microfiltration membranes.

The tasks of the modified Si NPs coated on tubular α-alumina were listed below followed by schematic of the Si NPs coating on α-alumina tubular microfiltration membranes.

Task 1: Incorporate silica nanoparticles into inorganic membranes for oil/water emulsion separation in a cross-flow system.

Task 2: Characterization of the prepared membranes and study Si leaching from surface of membranes.

Task 3: Study the performance of the prepared membranes in terms of flux, oil rejection rate, and anti-fouling behavior in a cross-flow system.

CHAPTER II

LITERATURE REVIEW

2.1. Water and wastewater treatment process

Due to climate changes that are critical for our global population, the significance of water as a necessary asset for humankind is inevitable. Water demand has tremendously increased recently and based on an estimation the water demand for the whole globe will be reached to 6900 billion m^3 by 2030 [21, 22]. This amount is more than water available to most nations by approximately 64%. Thus, to tackle this water sacristy, using filtration systems to recycle water for reusing should be a priority. For example, if companies that consume huge amount of groundwater in industrial processes (oil and gas companies, textile manufacturers, laundries, breweries, etc.) treat their wastewater to a level for reuse, it will be the most promising method to decrease groundwater consumption and tackle water scarcity issues [21, 22]. Unlike the conventional techniques, such as coagulation/flocculation, biological treatment, and settling, and media filtration, the pressure driven membrane technology is more efficient and cost effective. Pressure driven membrane processes (microfiltration, ultrafiltration, nanofiltration, reverse osmosis) can be applied to reject a wide range of components [21, 23].

For example, the pressure driven membranes are used to remove components ranged from suspended solids (microfiltration process) to small organic compounds and ions (reverse osmosis process). However, the membrane process should be selected based on wastewater and water type. In other words, choose the rational pressure driven membrane process helps not only improve quality of treated water, but also decrease the cost of filtration process [24].

2.2. Pressure-driven membranes

Membrane filtration is a robust technique to remove particles in liquid solutions or gas mixtures. This technique has a wide range of applications ranging from dairy processing to wastewater treatment. The membranes act as a barrier that removes larger particles, while allowing smaller molecules to pass through the membrane into the permeate [25]. The driving force for pressure-driven membrane processes is the pressure difference between the feed and permeate side to pass feed through the membrane. Containments are removed according to different mechanism such as size, shape, and charge. Pressure-driven membrane processes can be categorized their characteristics (pore size) or applied pressure on membranes. The four main techniques of pressure-driven membrane filtration are Microfiltration (MF), Ultrafiltration (UF), Nanofiltration (NF), and Reverse Osmosis (RO), in order of decreasing pore size and operational pressure (Fig 2.2) [25, 26]. As shown in Fig 2.1, the pore size of microfiltration membranes ranges from 0.1 to 10 μm. They are mainly applied for removing large particulates, colloids, and bacteria from feed streams [26]. Ultrafiltration is similar to microfiltration in terms of process, but with smaller pore sizes ranging from 0.01 to 0.1 μm. UF membranes are used in the removal of viruses and polypeptides. These type of membranes are immensely applied in protein concentration and wastewater treatment industries. NF membranes are similar to reverse osmosis membranes in terms of structure. They are both have a dense layer (<1 μm) on top of a porous layer (50 to 150 μm) for small ion selectivity [22, 27]. NF membranes are able to remove multivalent salts and uncharged solutes, while allowing some monovalent salts to pass through. Unlike RO, NF membranes operate at lower pressures, making them an ideal option in terms of cost and also achieving an optimal combination of flux

and rejection. The pore size of RO membranes are smaller NF membranes and are able to reject all monovalent ions while allowing water molecules to pass through in aqueous solutions [23].

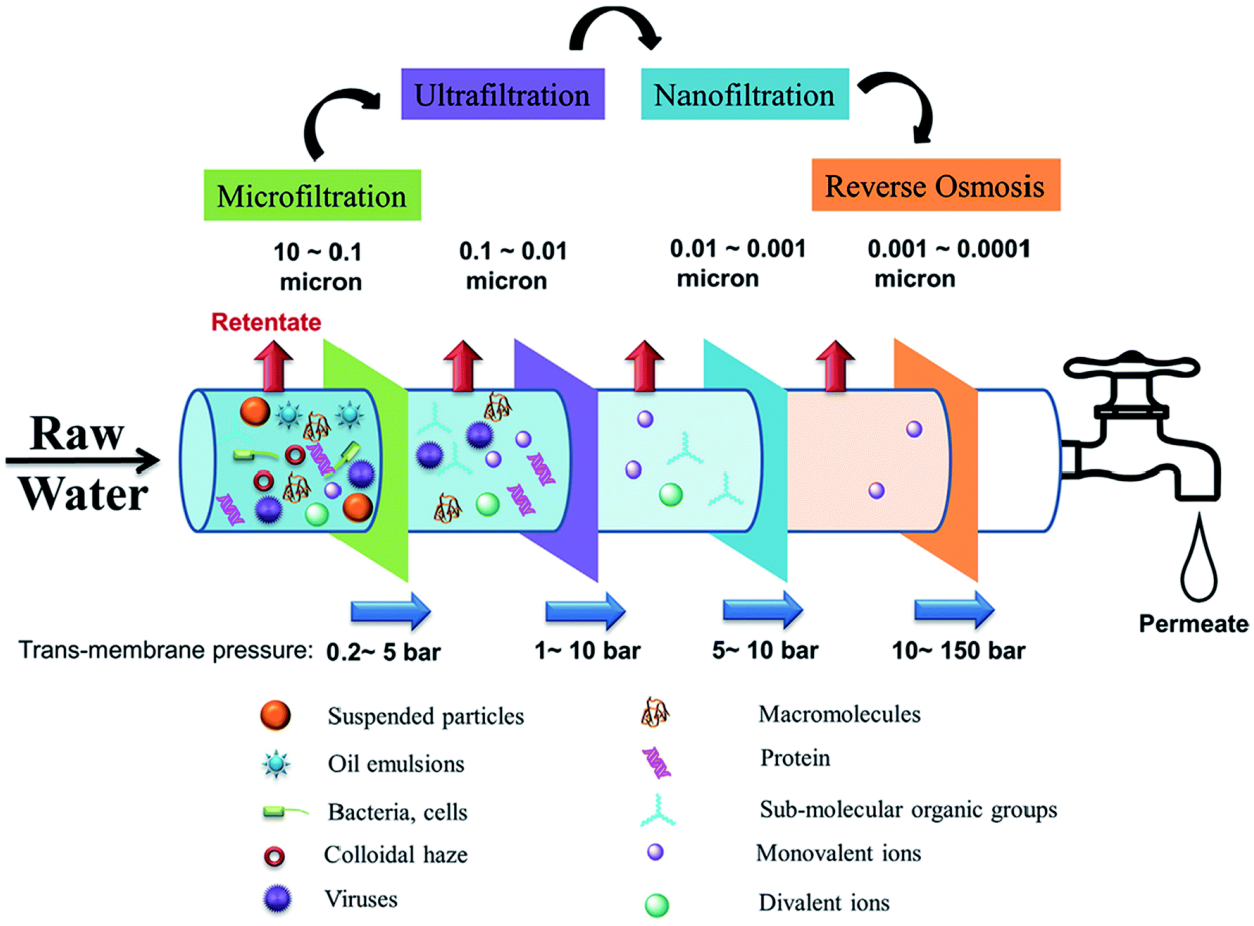

Fig. 2.1 Pressure-driven membrane process for water treatment technologies [25].

2.3. Ceramic membranes

In the early 1960, ceramic membranes were discovered and used for alcohol treatment and gas separation [76]. Generally, ceramic membranes are widely divided into porous and rigid ceramic membranes. The porous ceramic membranes are widely utilized in water treatment and have asymmetric structure including a thin selective layer (top layer), and a permeable support layer

(Fig.2.3). The ceramic membranes are categorized into cylindrical (hollow fiber and tubular) shape and flat sheets in terms of geometrics and configuration (Fig. 2.2) [77]. Among these two types of ceramic membranes, tabular and hollow-fiber ceramic membranes are immensely used in wastewater treatment because these membranes have higher active surface area, mechanical strength, and packing density [77, 78].

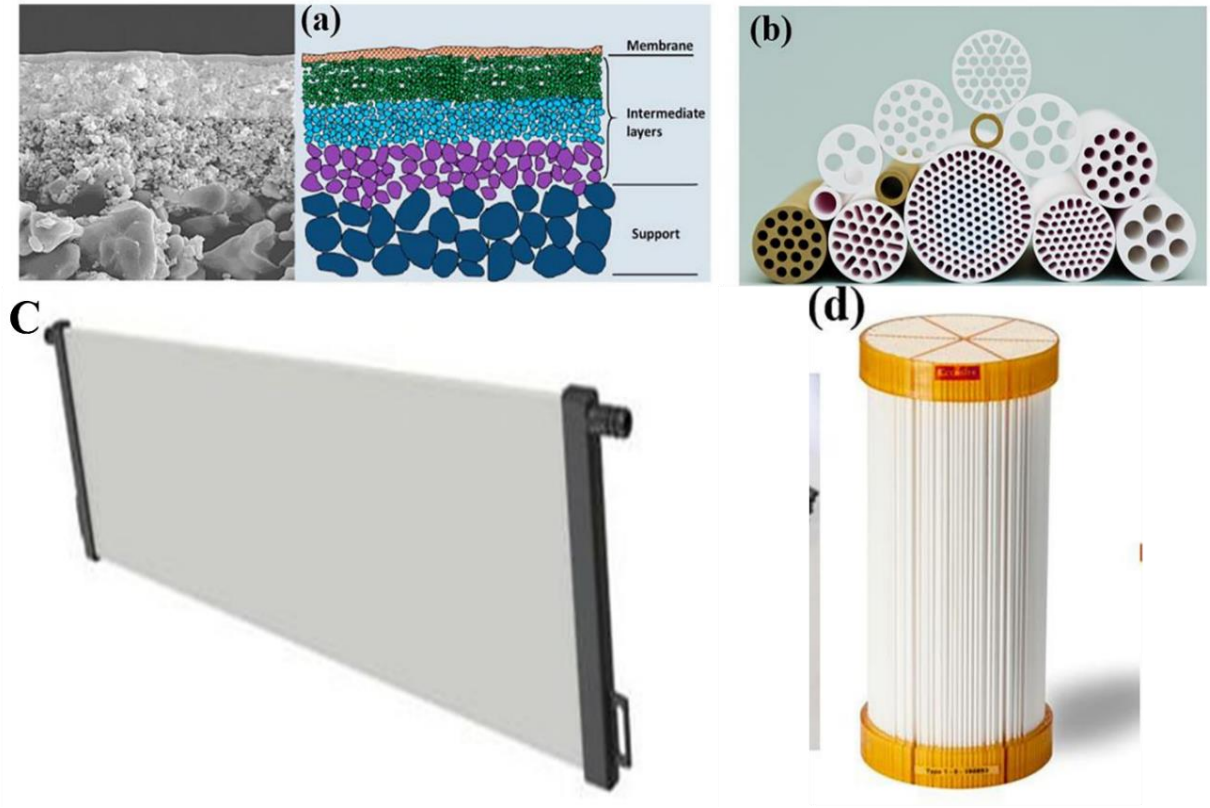

Fig. 2.2 The schematic (a) cross-section, (b) tubular (c) flat sheet, and (d) hollow fiber of the ceramic membrane [28].

One of the most significant advantage of ceramic membranes over polymeric membranes is that the ceramic membranes are tolerated in harsh environmental conditions, such as strongly acidic, basic and hot solutions [29, 30]. The ceramic membranes are thermally stable up to 280° C (in some cased with specially designed up to approximately 700° C) and have fantastic corrosion-resistance. Finally, the ceramic membranes have a long operational life, and high membrane flux [29]. On the other hands, the most disadvantage of ceramic membrane is that they are relatively more expensive

than polymeric membranes. It is hard to deal with the ceramic membranes because of their brittleness property. In addition, the ceramic membranes have low rejection and modification process to adjust pore size is a complicated process [30].

2.4. Polymeric membranes

Polymeric membranes are relatively the first option for industrial applications since they are very cost-friendly and efficient. Unlike the ceramic membranes, it is very easy to control and adjust pore size of the membranes during different formation techniques, such as mixed matrix and interfacial polymerization. We usually select a polymer Selection of a polymeric membranes depends heavily on feed that is supposed to be filtered [31]. Cellulose acetate (CA), polyacrylonitrile (PAN), polyimide, polycarbonate (PC), polyethylene (PE), and polypropylene (PP), and polytetrafluoroethylene (PTFE) are common types of polymeric membranes. Generally, the performance of polymeric membranes is improved by embedding nanofillers like metal/metal oxide or CNTs. Among various membrane processes such as reverse osmosis (RO), nanofiltration (NF), and ultrafiltration (UF), NF membranes have been widely applied for textile wastewater treatment, as they showed substantial benefits for salt and dye rejections [32]. Cellulose acetate (CA) is one of the most commonly utilized polymers due to its unique specification such as high selectivity, low-cost, outstanding biocompatibility, durability, thermal stability, and abundant natural resources [33, 34]. CA showed high tendency for hydrophilic materials which can be attributed to the existence of hydroxyl groups in its chemical structure, giving better film-forming and oleophobic properties [35, 36]. Although CA is hydrophilic, membrane fouling regarding CA is still considered one of the biggest issues because its hydrophilicity is not enough to avoid dye droplet deposition tendency toward CA surface.

Therefore, membrane modification would be a suitable choice to enhance membrane performance [11, 12]. Regarding the improvement of membrane performance, organic nanoparticles are promising alternative because they interact with polymers perfectly which could be attribute to

huge amount of hydrophilic functional groups. These hydrophilic groups enhance hydrophilicity, and fouling-resistant of the prepared membranes. The nanoparticles are metal-organic framework [16], chitosan [17], polystyrene [18], and polydopamine [19].

2.5. Methods

2.5.1. Membrane performance test

The oil rejection rate is defined and evaluated as follows:

$$\eta = 1 - \frac{C_i}{C_0} \tag{1}$$

where η stands for oil rejection rate, and C_0 and C_i are the concentration of oil in feed and permeate, respectively. The permeation flux was calculated using the following equation:

$$J = \frac{V}{A \times t} \tag{2}$$

where J is permeation flux (L m^{-2} s^{-1}), V (L) is the volume of the permeate, A (m^2) is the effective membrane surface area, and t (s) is the permeation time. The anti-fouling property of the membranes is measured by obtaining flux recovery rate (FRR). Initially, the filtration process using membranes is run for 1 h to calculate pure water flux ($J_{w,1}$), then BSA is treated for 1 h, and the obtained flux is defined as (J_p). During BSA treatment, the cake layers, responsible for fouling, are formed on the surface of the membrane. Next, the fouling is removed from the surface of the membranes by DI water washing for 10 minutes. Then, the cleaned membranes are placed in the setup to calculate the second water flux defined as ($J_{w,2}$). The flux recovery ratio (*FRR*) is obtained using equation 3, which shows the ability of the membranes against fouling phenomena. *FRR* is defined as follows:

$$FRR = \left(\frac{J_{w,2}}{J_{w,1}} \right) \times 100 \tag{3}$$

2.5.2. Atomic Layer deposition (ALD)

ZnO ALD was performed in an ALD reactor unit (OkYay Tech, Ankara, Turkey). The deposition was operated at 120 ºC and 120 millitorr. Before the deposition process, the α-alumina supports (1-inch diameter, 1 mm thickness, and ~25% porosity from Coorstek) were placed and stabilized inside the chamber for 30 min. To deposit a thin and uniform layer of ZnO (with a thickness of ~2 Å per cycle), nitrogen was used as a carrier gas and the subsequent amount of DI water and diethylzinc, $Zn(C_2H_5)_2$, (Strem Chemicals Inc., >95%, Newburyport, MA, USA) were run at the various cycles (20, 40, 60, 80, 100 and 120, respectively). The ZnO ALD process was conducted through the following mechanism, which was illustrated in Fig. 1.2 [37].

$$Zn(C_2H_5)_2 + H_2O\,(g) \longrightarrow ZnO + 2C_2H_6\,(g) \quad (4)$$

2.5.3. Dead-end and cross-flow filtration systems

Generally, pressure-driven membrane processes can be operated in two different modes: dead-end and cross-flow operations. In the dead-end mode, there are only two streams, one inlet and one output. One stream of the feed enters the membrane module and flows vertically toward the membrane surface, and the other stream leaves the membrane module. However, in the cross-flow mode, there are three streams, one stream of the feed flows tangentially to the membrane surface, and the other two streams leaving the membrane module with one as a retentate flow and the other one as the permeate flow [38]. The dead-end mode is employed mostly in microfiltration (MF) and ultrafiltration (UF) for clarification and sterilization, where the feed is relatively clean. In most applications, the accumulation of the rejected particles or molecules is so severe that dead-end operation becomes impractical and cross-flow operation has to be adopted. The tangential flow in the cross-flow mode can help to shear away the accumulated rejected species at the membranes,

limit the heights of cake layers, and hence maintain the permeate flux [39]. Fig. 2.3 Shows the schematic diagrams of the dead-end mode and the cross-flow mode, and their effects on the permeate flux and the height and resistance of the cake layer [39].

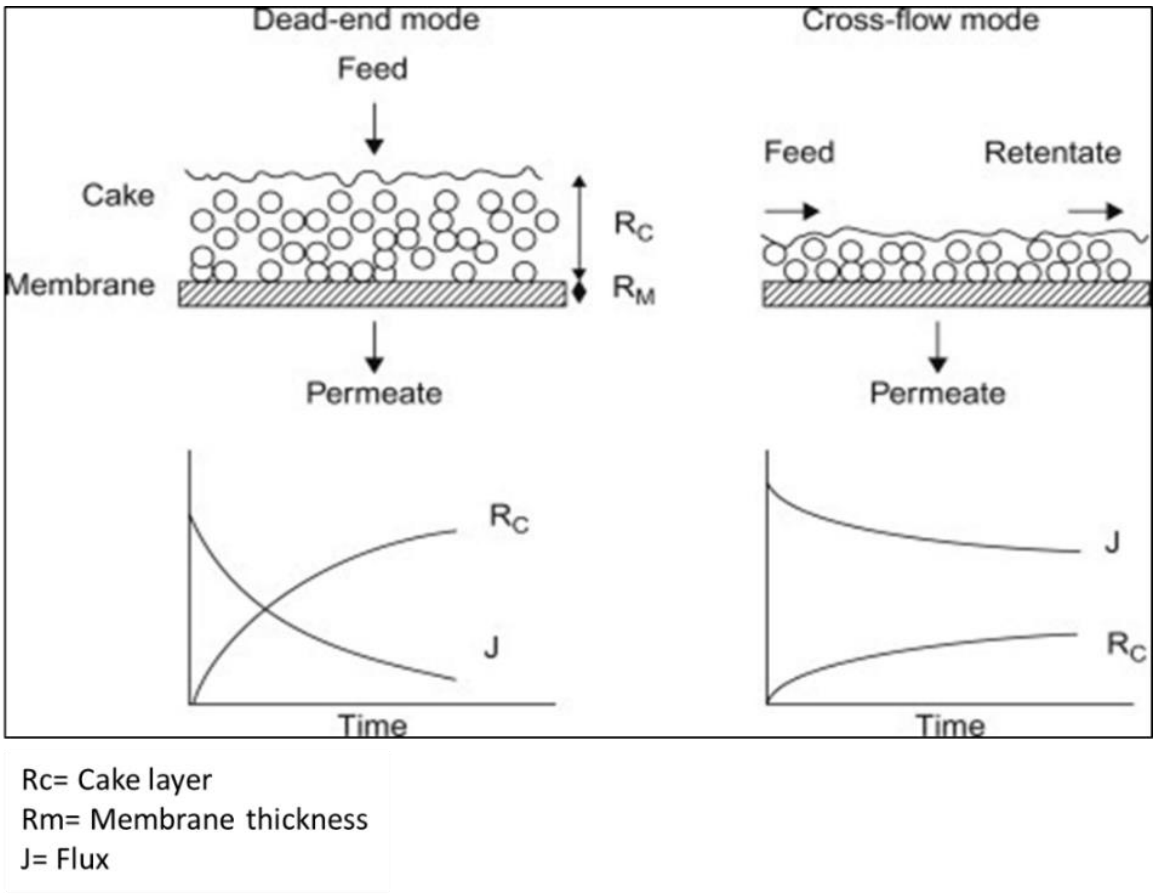

Fig. 2.3 The schematic diagrams of the dead-end mode and the cross-flow mode, and their effects on the permeate flux and the height of the cake layer [39].

CHAPTER III

FABRICATE ZEOLITE MEMBRANES WITH TUNABLE HYDROPHILICTY FOR OIL-WATER MIXTURE SEPARATION

3.1. Introduction

The availability of clean water has been an important issue around the globe, where the safety and maintenance of clean water sources is critical to environmental, societal and human health. Oil spills attract the attention of the public because of their negative impact on human health, the environment and regional economics [40-42]. Consequently, the development of oil/water separation technology is a worldwide goal and challenge. Various methods for oil/water separation have been proposed to refine the water, such as coagulation, adsorption, air flotation, and sorption process [43-49]. However, these methods have drawbacks, such as high cost, large machinery and low efficacy [50, 51]. Membrane filters have been widely used in oil-water mixture treatment due to their high separation capability and facile operation conditions [52, 53] Micro/nano and ultra-filtration membranes have also been utilized for oil-water separation [54, 55].

Typically, porous membranes, regardless of their construction, suffer from fouling, which reduces the permeation efficiency [50, 51, 54, 55]. For instance, polymeric membranes are attractive due to their effective selectivity, affordable cost, easy handling and low energy consumption [54], but are prone to fouling by natural organics, proteins and biofilms and corresponding decreases in flux over time. To remove foulants on the membrane surface, chemical rinsing is a proposed remedy, but strong oxidants can damage the membrane structure and decrease its lifetime [56]. Thus, regardless of its own costs and benefits, efforts on the use of organic membranes have remained an open challenge to be resolved.

Inorganic membranes have great potential for oil-water separation due to their chemical and physical properties, high durability and reusability [52]. For treating oily wastewater, inorganic membranes, such as carbon nanotubes, graphene, and zeolite-based membranes have been proposed [57, 58]. Zeolite membranes have attracted significant attention due to their high surface area, unique molecular sieving properties, and various pore sizes [59, 60]. Zeolites consist of aluminum, oxygen, and silicone with tetrahedral crystalline framework, which produces discrete pore sizes [61]. In particular, NaA zeolites have been used in membrane applications because of their unique properties, such as high thermal stability and tunable pore diameters from 0.3-0.5 nm using ion exchange of aquatic calcium or potassium salt [62, 63]. Kiadehi et al. synthesized a NaY zeolite using the secondary growth method on stainless-steel mesh for hydrogen separation. They reported that the NaY zeolite mesh improved the hydrogen permeation flux by approximately 12 times relative to a palladium composite membrane [64]. Jiang et al. synthesized hollow fiber CHA zeolite membranes with varied Si/Al ratios. CHA zeolite membranes with Si/Al ratios > 2.9 showed the highest separation factor (>10,000), as compared to 5,000 for a Si/Al ratio of 2.7. They reported it is probably because the low Si/Al ratio resulted in low crystallinity of membranes and the incomplete crystallization or dissolution of CHA zeolite crystals. The optimized Si/Al ratio enhanced the membrane's stability in harsh environmental conditions, such as acidic environments,

because the high crystalline zeolites were not blocked, unlike the lower Si/Al ratio membranes [65]. For alcohol/water separation, Li et al. improved stability of NaA zeolite membranes by adding a polyelectrolyte on the membrane surface, which produced a permeability of 875 g m^{-2} h^{-1} and ethanol separation of 99.8% [66]. Liu et al. investigated the effect of seeding methods, such as dip-coating, rubbing, and combinations of both rubbing and dip-coating, on the NaA zeolite membrane's performance. The combination of rubbing and dip-coating showed a more uniform seed layer and improved its performance for ethanol/water separation, as compared to separating dip-coating and rubbing seeding methods [67]. Significant efforts have been made to reduce membrane fouling [68-71]. For instance, Ju et al. [68] synthesized the fouling-resistant poly (ethylene glycol) diacrylate (PEGDA) membrane for oil/water separation. This membrane showed higher permeation and lower oil fouling than uncoated polysulfone (PSF) ultrafiltration membranes. Water permeability increased from 10 to 150 L μm/ (m^2 h bar) when the amount of water in the prepolymerization water mixture increased from 60 to 80 wt%. The membranes not only demonstrated a high tolerance for a wide range of pH (1-14) but also improved anti-fouling for oil/water separation [69].

In order to reduce fouling, an attractive approach is to develop hydrophilic membranes. Hydrophobic membranes are intrinsically vulnerable to oil fouling since hydrophobic materials are prone to adsorbing to the membrane surface due to their oleophilic properties [72, 73]. Using hydrophilic-material-coated meshes for oil/water separation is promising because they repel oil droplets and facilitate the removal of oil foulants. Materials such as hydrogel [74], ZnO [75-77], and TiO_2 [53, 78] have been coated on meshes to enhance hydrophilicity for oil/water separation. In spite of the aforementioned membranes' high oil rejection efficiencies, their structures are not compatible in hot, acidic, and basic solutions [79, 80]. Zeolite membranes are favorable because of their chemical, mechanical, thermally stable, and corrosion resistant properties.

Herein, a NaA zeolite-coated mesh with tunable hydrophilicity is developed by a secondary growth method and placed in practice for high-level oil/water separation. The zeolite meshes are calcined and retested to investigate the oil/water separation efficiency, reusability, regenerability, and stability. The ratio of Al/Si (ASR) in the NaA zeolite mesh is considered as a key factor. Moreover, the NaA zeolite-coated mesh is tested for various oils including olive oil, mineral oil, and diesel to assess the effect of the type of oil on oil/water separation efficacy. The degree of hydrophilicity is evaluated along with for mesh stability analysis in in acidic, basic, and hot solutions.

3.2. Experimental

3.2.1. NaA seed synthesis

The procedure for preparing NaA seeds has been previously reported by Zhang et al. [81] and only an abbreviated description is provided here. Sodium aluminate (Al (Al_2O_3):50-56%, Na (Na_2O):40-45%), sodium metasilicate nonahydrate (≥98% purity) and sodium hydroxide (99.99%) were purchased from Sigma-Aldrich (USA). Sodium aluminate (7.16 g) was added to 35 g of deionized (DI) water, and the resulting aluminate solution was stirred for 5 min. Silicate solution was produced by adding 20.72 g of sodium metasilicate nonahydrate to 42 g of DI water, and the resulting solution was stirred at 50 ^oC for 10 min. Subsequently the silicate solution was gradually added to the aluminate solution under vigorous stirring for 15 min. The resulting solution was transferred into a hydrothermal vessel and processed at 100 ^oC for 4 h. The synthesized NaA zeolite powder was washed in deionized water in a centrifuge and dried. Then, NaA seeding solution (3 wt%) was obtained by adding 1.5 g of NaA zeolite powder into 50 ml of DI water. The pristine stainless steel mesh (0.9 in × 0.9 in) was washed and cleaned by ethanol, acetone, and deionized water, in that order. The cleaned mesh was dried overnight at 50 °C in an oven. Before hydrothermal synthesis, the cleaned mesh was seeded by dip-coating method (immersed in in NaA seeding solution) for 5 min (Fig. 1.1).

3.2.2. Zeolite-coated mesh synthesis

The synthesis solution for secondary growth was prepared using the following procedure [81]: Sodium hydroxide was dissolved in DI water under vigorous stirring for 5 min. Then, sodium aluminate was added and the resulting solution was stirred for 3 h. Subsequently, a uniform solution was obtained by adding sodium metasilicate nonohydrate and the solution was stirred vigorously for 30 min. The molar ratio of the solution was maintained at $H_{18}Na_2O_{12}Si$: NaOH: H_2O: $NaAlO_2$ = 1: 1.89: 172: X, respectively. The value of X was varied from 0 to 1.82. The dried seeded mesh was kept vertically inside a 20 ml autoclave reactor which contained 18 ml of synthesis solution and hydrothermal synthesis was carried out at 100 °C for 4 h (Fig. 1b and c). After hydrothermal growth, the fabricated membrane was taken out from the reactor and washed with DI water. Then, the NaA zeolite coated mesh was calcined at 450 °C for 4 h with a heating and cooling rate of 30 °C/h.

3.2.3. Characterization

A FEI Quanta 600F field emission scanning electron microscope (SEM) equipped with an Energy Dispersive Spectrometry (EDS) X-ray microanalysis unit was used to examine the surface morphology and chemical composition of the NaA zeolite mesh, respectively. The phase and crystal structure of the NaA zeolite mesh was characterized by X-ray powder diffraction (XRD) (Bruker D8-A25-ADVANCE) scanning from 2Θ of 5–40°. UV–vis spectrophotometer (Beckman Coulter DU 730) and the analytical weighing scale (Cole-Parmer Instrument Company-USA) was used to measure the oil concentration in the permeate. A contact angle goniometer (Rame-Hart Goniometer model 250) was used to measure the contact angles of the mesh at room temperature. While measuring contact angle, a section of the mesh was put on plastic coverslips to hold the mesh and to avoid its submersion into water. To obtain a reliable oil contact angle (OCA), the results reported herein are on the average of three measurements on the three different areas of the NaA

zeolite mesh. Moreover, n-hexane (2 µL) was descended on the membrane surface for each contact angle measurement.

3.3. Results and Discussion

3.3.1. Characterization of NaA zeolite mesh

The surface morphologies of the pristine and NaA zeolite coated mesh were examined by SEM. For an ASR = 0 (Fig. 3.1a0-a2), the coating is highly nonuniform when compared with those processed with a higher ASR (0.3-1.82), which indicates the crystallization was incomplete. However, with increasing ASR (Fig. 3.1b-e), it was found that the mesh surface was entirely coated by NaA zeolite crystals. The pore size of the meshes decreased from 150 µm (pristine mesh) to about 10 µm (ASR = 1.21, Fig. 3.1e0). As shown in Fig. 3.1c2, 3.1d2, and 3.1e2, the NaA zeolite meshes were aggregated on the stainless steel mesh surface and showed higher surface roughness, a very crucial factor for the underwater super-hydrophobicity of the mesh [79, 82]. To evaluate the stoichiometry of the NaA zeolite mesh, EDS was performed on the pristine and the zeolite coated mesh (ASR = 1.21). Based on Fig. 3.2a, iron, chromium, and nickel are the main components of the pristine mesh, as expected per the manufacturers specifications. The carbon peak is attributed to the carbon adhesive used to hold the mesh onto the SEM specimen holder. For the zeolite coated mesh with ASR = 1.21 (Fig. 3.2b), the elemental stoichiometry is 49% O, 15% Na,15% Al, and 12% Si, which confirms that NaA zeolite film has been deposited on the stainless steel mesh. The XRD pattern of NaA zeolite powder, pristine stainless steel mesh, and NaA zeolite mesh are shown in Fig. 3.3. The XRD pattern of the NaA zeolite powder (Fig. 3.3c) ranges from 5 to 35°, which corresponds to the characteristic peaks of NaA zeolite crystals [83, 84]. The XRD pattern of NaA zeolite coated mesh (Fig. 3.3a) presents characteristic peaks of NaA zeolite crystals, as well as some peaks coming from the stainless steel mesh [64, 83, 84], which is to be expected.

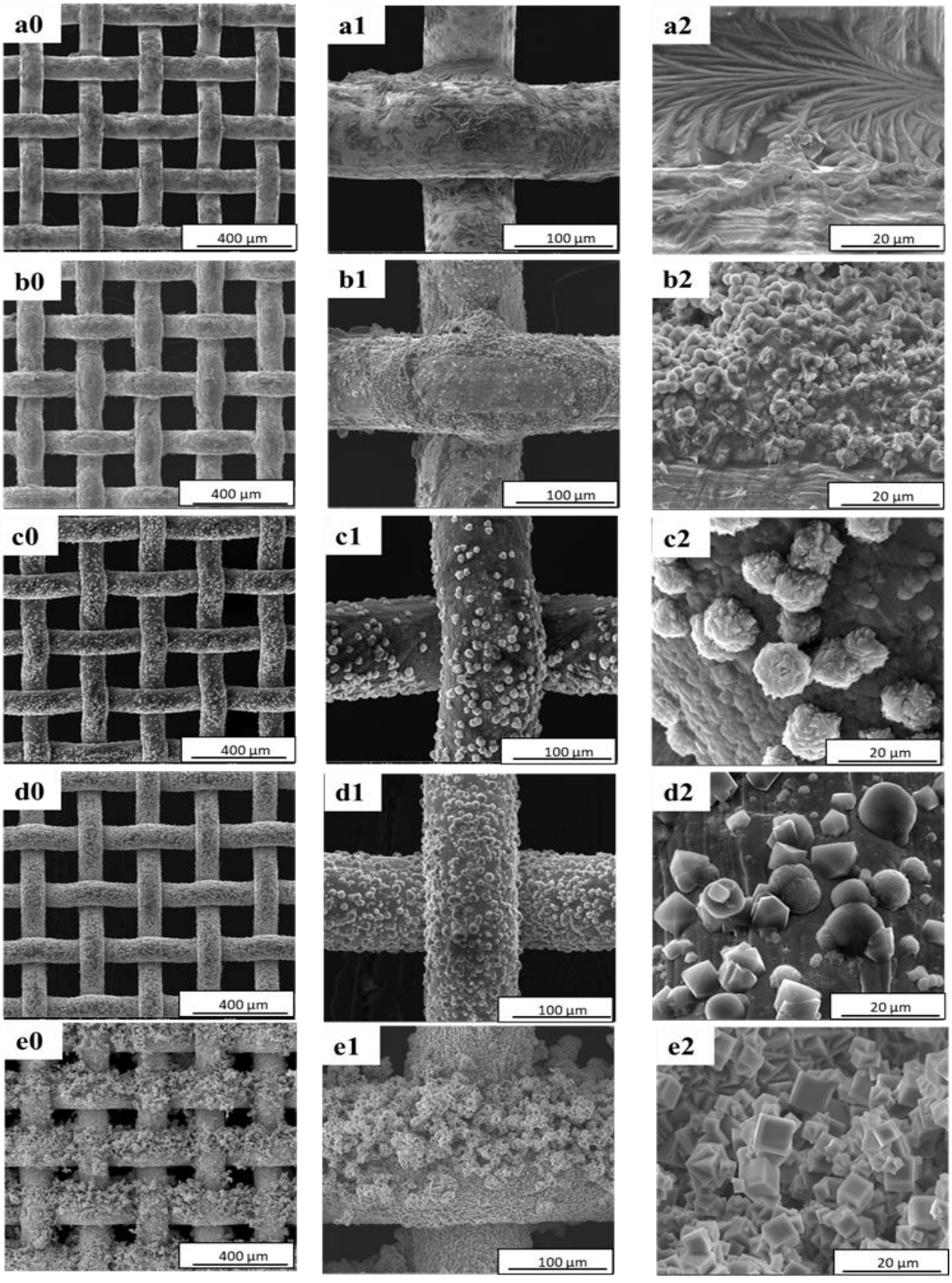

Fig. 3.1 SEM photos of NaA zeolite coated mesh with (a) ASR = 0, (b) ASR = 0.31, (c) ASR = 0.61, (d) ASR = 0.91, and (e) ASR = 1.21.

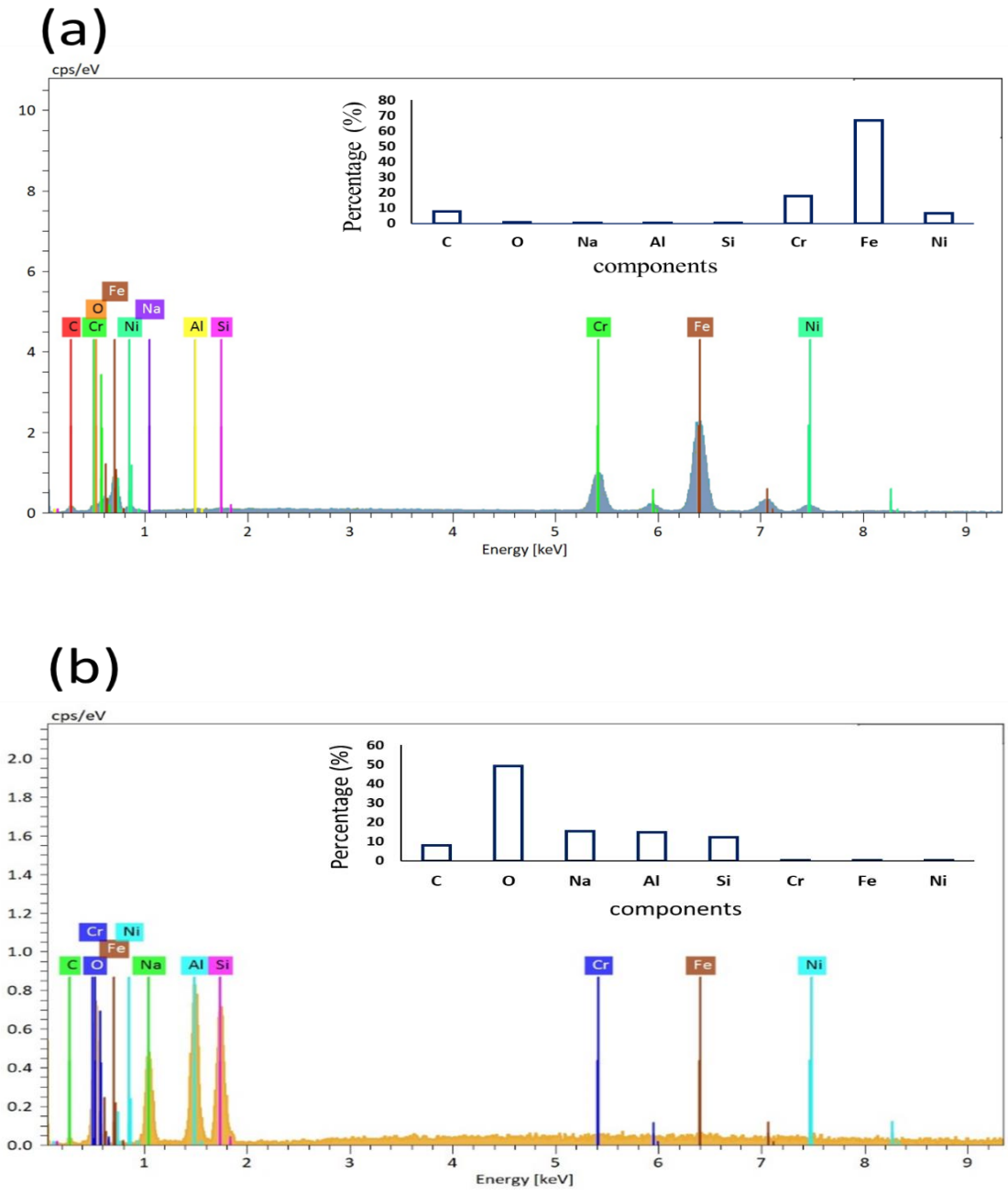

Fig. 3.2. (a) The energy dispersive spectrometer (EDS) element distribution of pristine mesh and (b) NaA zeolite (ASR = 1.21) coated on the mesh support.

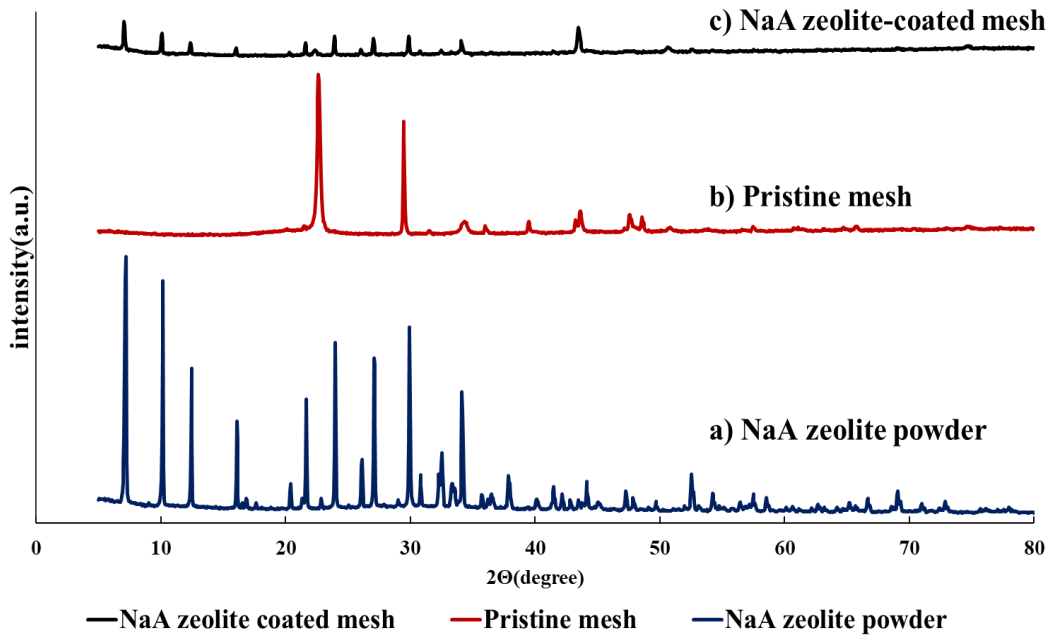

Fig. 3.3. XRD pattern of a) the NaA zeolite coated mesh, b) pristine mesh, and c) NaA zeolite powder.

The wettability of pristine mesh and NaA zeolite coated mesh were assessed by water contact angle (WCA) and oil contact angle (OCA) measurements. As shown in Fig. 3.4a, for a 2 µL DI water dropped on the surface of the pristine mesh, the WCA is 115.3°, indicative of the intrinsic hydrophobicity of the pristine mesh. For the zeolite coated mesh (ASR = 1.21), the WCA is 0° (Fig. 3.4b), indicating that the NaA zeolite significantly increases the hydrophilicity of the mesh. To study the effect of ASR on the wettability of the membrane, underwater OCA was measured using n-hexane (2 µL). The underwater OCA of the zeolite mesh (ASR = 1.21) is 163.7° (Fig. 3.4c), indicating that the underwater super-oleophobicity of the membrane increases with the introduction of aluminum. In other words, the oil-fouling of the zeolite meshes decreases with increasing ASR from 0 to 1.21.

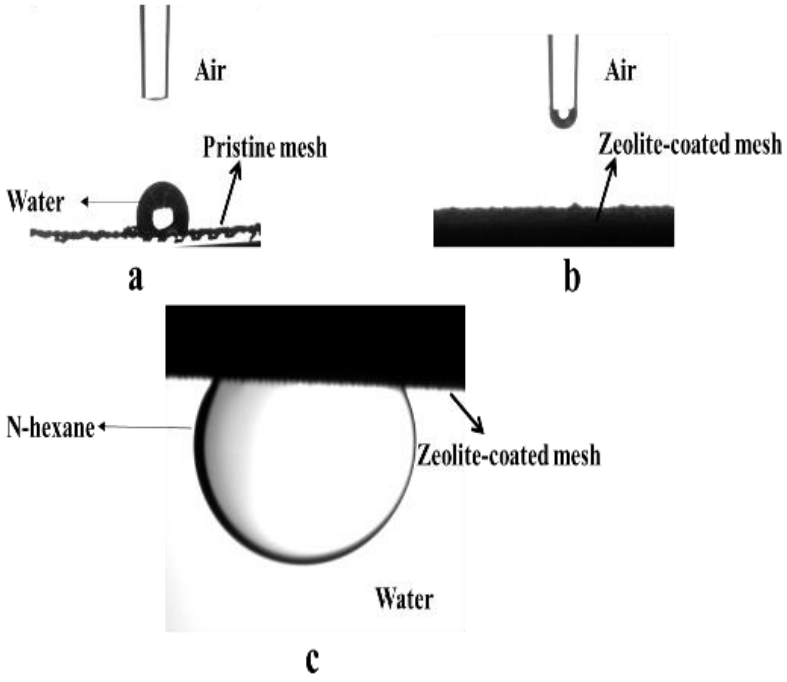

Fig. 3.4 Water contact angle in air for (a) pristine mesh, (b) NaA zeolite mesh (ASR=1.21), and (c) underwater oil contact angle for NaA zeolite coated mesh (ASR = 1.21).

Fig. 3.5 shows the underwater super-oleophobic property of zeolite meshes for various ASRs. With increasing ASR from 0 to 1.21, OCA value increase from 132.0° to 163.7° (Fig. 3.5) and then slightly decreases to 160.7° for an ASR = 1.82. Given the high levels of OCA (e.g., 163.7° at ASR = 1.21), it is possible that a water layer forms between the NaA zeolite coated mesh and the n-hexane droplet [85-87]. If NaA zeolite crystals are engaged and anchor the water layer, it could repel the oil from adhering to the surface[85, 88]. The empty 2p orbitals of Al^{3+} ions have an enormous tendency to link with water, resulting in an increase in the density of hydroxyl groups on the surface of the NaA zeolite crystals. Therefore, the enhanced hydrophilicity of the hydroxylated surface remarkably helps to reject oil molecules [85, 88]. Assuming that the capacity of empty 2p orbitals of Al^{3+} ions is limited, after incrementing the ASR there was not a considerable increase in OCA values. However, the OCA decreased slightly for ASR> 1.21.

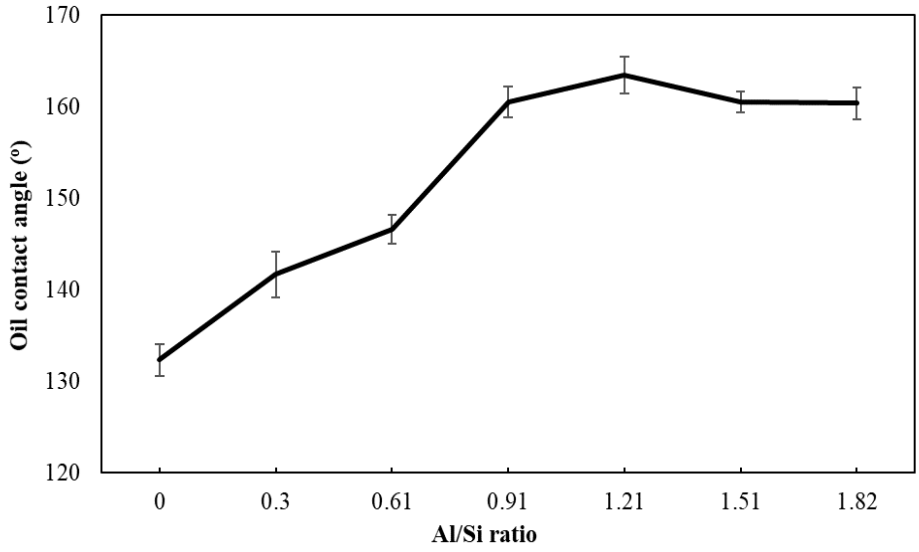

Fig. 3.5 Underwater oil contact angles of n-hexane on the zeolite-coated mesh as a function of Al/Si ratio.

3.3.2. Zeolite-coated mesh performance for oil/water separation

As shown in Fig. 3.6, the oil rejection rate for ASR = 0 decreased from 96.2% to 93.7% after 4 separation cycles, probably because there are no Al^{3+} ions that can enhance membrane surface hydrophilicity. However, the oil rejection rates of the mesh with ASRs of 0.3-1.82 were higher than that of ASR = 0, and the mesh with ASR of 1.21 showed the highest oil rejection rate of 99.4% during 4 separation cycles. Since Al^{3+} ions were incorporated in the zeolite structure by replacing Si^{4+} ions, the empty 3p orbital on the Al^{3+} ion accept unaccompanied pair electrons from electron donors. Therefore, it is expected that a larger concentration of Al^{3+} ions will increase the oil rejection [61, 89]. In other words, the higher the concentration of Al^{3+} ions incorporated into the membrane structure, the higher the oil separation rate. Once an oil/water mixture liquid is applied to the membrane surface, hydroxyl groups attach to Al^{3+} ions through synchronized bonds [65, 89], which converts the surface of the mesh from hydrophobic to hydrophilic through hydrogen bonding of hydroxyl groups. Consequently, a larger ASR in the mesh increases the connection between water and the mesh surface and leads to a higher oil rejection rate [81, 89].

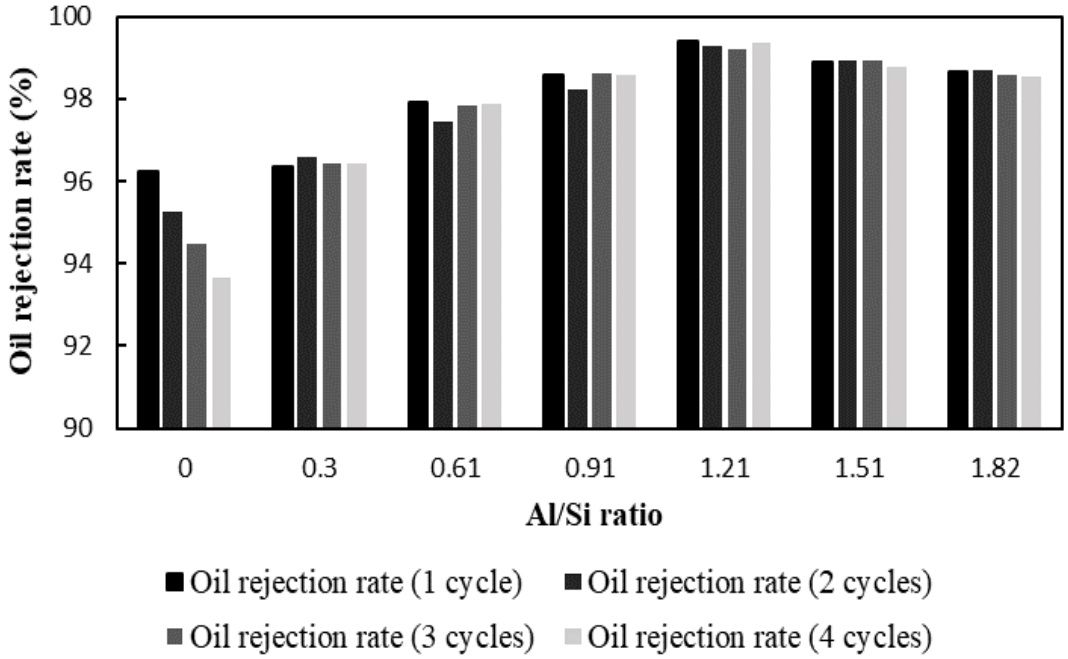

Fig. 3.6 The oil rejection rate of NaA zeolite-coated mesh as a function of Al/Si ratio.

Fig. 3.7 is a plot of the permeation performance of NaA zeolite-coated mesh as a function of ASR. According to Fig. 3.7, the water flux increases with increasing ASR, where the maximum water flux of 13,356 L m^{-2} h^{-1} is achieved for an ASR = 0.91 and subsequently decreases with increasing ASR. This decreasing trend of the flux for ASR>0.91 is attributed to the combination of underwater OCA and the decreasing pore size of the zeolite coated mesh (Fig. 3.5)[53]. Since the underwater OCA value is proportional to water penetration across the mesh [53, 90], the smaller OCA could decrease water penetration across the zeolite mesh, indicative of a weakening of the water capillary films. To test the NaA zeolite coated mesh in corrosive aqueous solutions, the best zeolite mesh (ASR = 1.21) was selected and tested in various oils, such as n-hexane, mineral oil, olive oil, and diesel fuel. Fig. 3.8 shows that the oil rejection rates for various oils were above 98.1%.

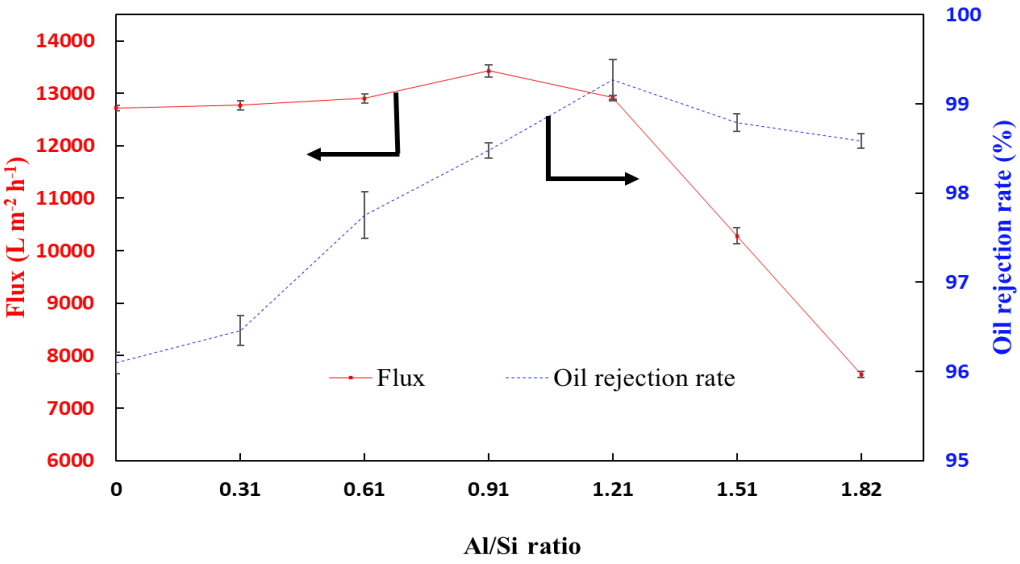

Fig. 3.7. Effects of varied Al/Si ratios on water flux and oil rejection rate of the zeolite-coated meshes.

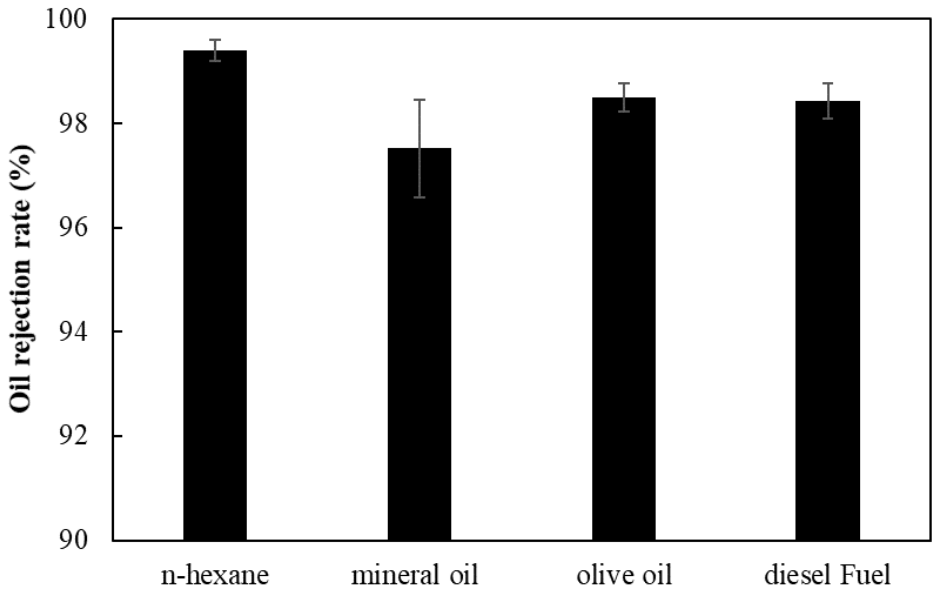

Fig. 3.8. Oil rejection rate of NaA zeolite-coated mesh with ASR = 1.21 for various oils.

3.3.3. Reusability and stability of the NaA zeolite coated mesh membrane for oil water separation

One of the primary challenges in membrane technology is fabricating anti-fouling membrane for long-term usage. Generally, membranes are highly prone to fouling, which reduces their separation efficiency and increases energy consumption [91]. To test the long-term reusability of the zeolite mesh for oil/water separation, we selected the mesh with ASR = 1.21 and evaluated for multiple separation cycles. After washing the used membrane with DI water and waiting for 10 min., the next oil/water separation was performed. As shown in Fig. 3.9, the oil rejection rate for the zeolite mesh with ASR = 1.21 after operating for 15 separation cycles remains greater than 99%. The results indicated impressive stability and reusability of the zeolite mesh. To assess the stability, the zeolite mesh was tested in acidic, basic, and hot oil/water mixtures, respectively. Before the test, the mesh was pre-wetted by 1M HCL(acidic), 1M NaCl, and hot water, respectively.

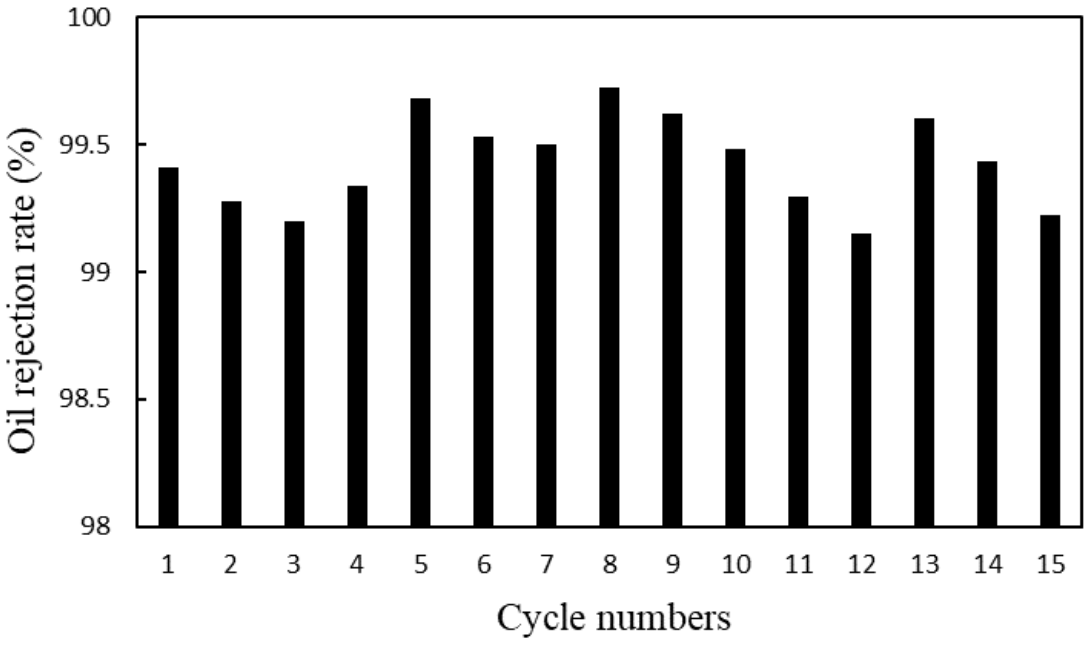

Fig. 3.9 Oil rejection rate of the NaA zeolite-coated (ASR = 1.21) mesh during 15 separation cycles of oil/water mixture.

Fig. 3.10 shows that the zeolite mesh is quite stable in corrosive or hot aqueous solutions. The average oil rejection rate in normal, hot water, acidic, and basic solutions is 99.4%, 99.7%, 99.4%, and 99.4%, respectively. SEM images of the mesh before and after testing in corrosive or hot aqueous solutions are presented in Fig. 3.11. Although some cracks are observed on the mesh surface, the NaA zeolite structure remains unchanged, indicative of the high stability of the NaA zeolite structure in harsh conditions, which is supported by permeation results.

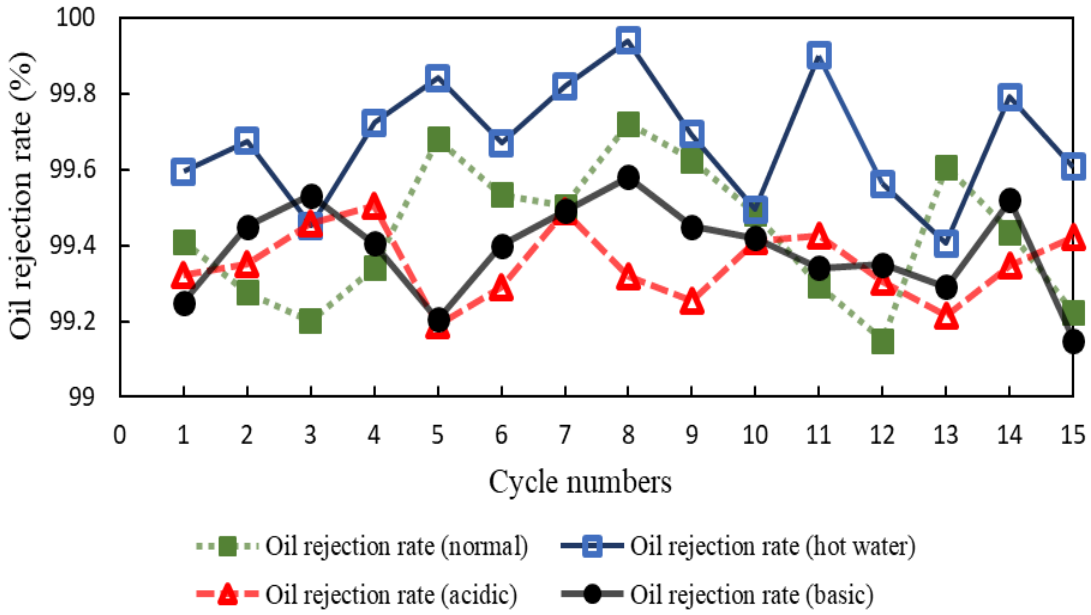

Fig. 3.10. Oil water separation rate of NaA zeolite-coated mesh with ASR = 1.21 in ordinary, acidic, basic, and hot solutions.

Moreover, reusability is one of the most significant features of the zeolite mesh. We examined the reusability by the re-calcination process. The used zeolite coated-mesh were re-calcined in the oven at 550 °C for 6 h with heating and cooling ramping rates of 30 °C/h. Upon subsequent use, the oil rejection rate is nearly unchanged and the average oil rejection rate after 3 re-calcination cycles is >99.4% (Fig. 3.12), as compared to that before calcination (99.7%). After 4 cycles of calcination, the zeolite-coated mesh exhibit reproducibility in terms of oil/water separation performance, which demonstrates that the recalcination is a simple and fast method to refresh the used mesh without

sacrificing performance. The re-calcination can not only save the membrane regeneration time, but also decreases the operational cost [89].

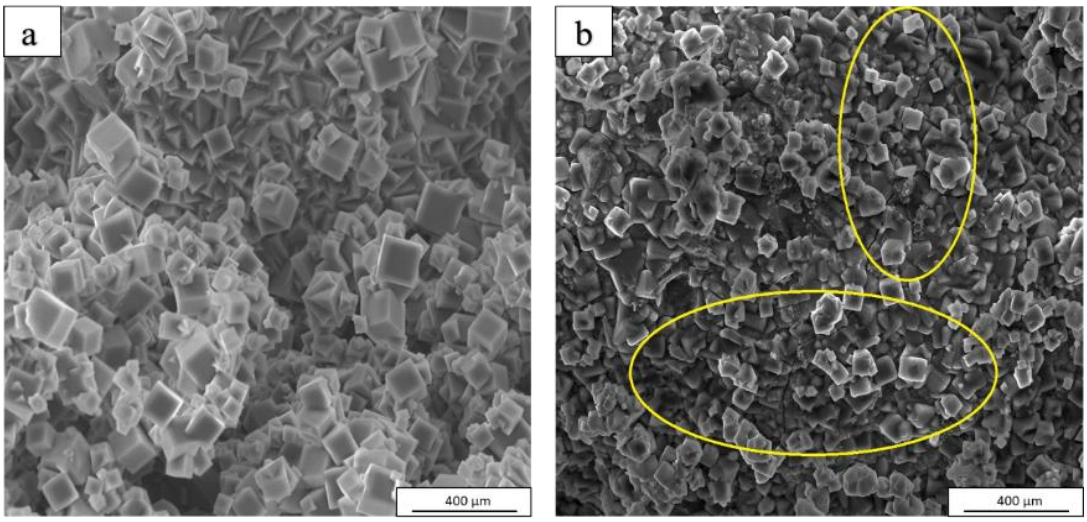

Fig. 3.11 SEM photos of NaA zeolite-coated mesh a) before and b) after oil / water separation test in harsh environmental conditions.

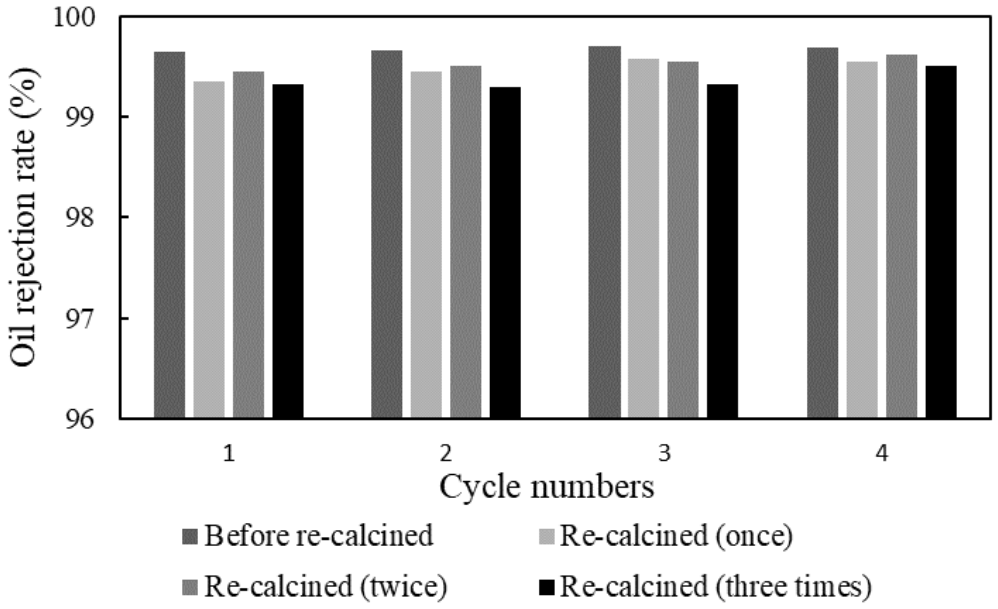

Fig. 3.12 Oil rejection rate of the NaA zeolite-coated meshes with ASR = 1.21 before and after calcination for oil/water separation.

To further investigate, the stability of the zeolite mesh, EDS has been performed before and after cyclic re-calcinations to observe changes in the zeolite stoichiometry and is summarized in Table 3.1. The ASR decreases slightly from 1.21 to 1.11 after three re-calcination cycles, which is attributed to the loss of Al. During the re-calcination process, organic components, epoxy, and residual oil on the mesh surface can be burned and converted to form water [92, 93]. The re-calcination process in the presence of water under 550 ^{o}C cause dealumination in the zeolite structure.

Table 3.1: Elemental surface composition of NaA zeolite coated mesh (ASR = 1.21) before and after 3 times re-calcination.

Samples	**EDS atomic %**		**Al/Si**
	Al	Si	
Before re-calcination	21.59	17.86	1.21[a]
After 1st re-calcination	21.10	17.52	1.20[b]
After 2nd re-calcination	20.55	17.24	1.19 [b]
After 3rd re-calcination	16.61	14.98	1.11 [b]

[a] before separation test
[b] after separation test

3.4. Conclusion

We synthesized NaA-type zeolite-coated mesh and controlled hydrophilicity by varying the Al/Si ratio (ASR). The zeolite mesh with ASR = 1.21 showed the highest separation efficiency of 99.5%. By increasing ASR from 0 to 1.21, the oil contact angle increased from 132° to 163.7°, an indication of increasing hydrophilicity of the mesh. However, with further increasing of the ASR from 1.21 to 1.82, the oil contact angle slightly decreased to 160°. NaA zeolite layer formation on the mesh was confirmed by EDS, with a composition of 49% O, 15% Na,15% Al, and 12% Si, respectively. The zeolite-coated mesh (ASR = 0.91) had a water flux of > 13,513 L m^{-2} h^{-1} and the zeolite-coated

mesh (ASR = 1.21) had an oil rejection rate of > 99.4%. The zeolite mesh exhibited good stability, reproducibility, and refreshability in corrosive or hot aqueous solutions. The mesh performance in various oils, such as n-hexane, mineral oil, olive oil, and diesel, the oil rejection rate was above 98%. The results show that the NaA zeolite-coated membrane is suitable for oil/water mixtures separation.

CHAPTER IV

IMPROVING ANTIFOULING PROPERTY OF ALUMINA MICROFILTRATION MEMBRANES BY USING ATOMIC LAYER DEPOSITION TECHNIQUE FOR PRODUCED WATER TREATMENT

4.1 Introduction

Produced water (PW) is the water that comes out of a well with crude oil during production. PW is a combination of dissolved and dispersed oil components, dissolved minerals, production chemicals, and produced solids that contains a complex mixture of water, salts, and heavy metals [94]. Regulations restrict the discharge of PW into the environment. For instance, per the Paris Convention, the maximum Total Dissolved Solids (TDS) level for discharge can be 40 mg/L for offshore and 5 mg/L for onshore [95]. However, in the United States, the Environmental Protection Agency (EPA) has set an upper limit of overboard discharge of 72 mg/L per day and 48 mg/L per month [96]. These stringent regulations demonstrate the urgent need for evolving efficient treatment technologies. The conventional technologies for treating PW are dissolved air flotation (DAF) [97], coagulation [98], solvent extraction [99, 100], froth flotation [101, 102], biodegradation [103], and adsorption [104, 105]. These methods have disadvantages, such as low efficiency, high cost, corrosion, and re-pollution [94].

Filtration of PW utilizing membrane technology has been studied since 1976. Compared to conventional technologies, membrane separation provides advantages, such as high selectivity, easier scale-up, energy-efficient operation, and smaller space requirements [106]. These benefits make membrane treatment a potential method for treatment of PW [94, 106], where polymeric [107, 108] and ceramic membranes [109-111] have been used. Ceramic membranes showed advantages over polymeric membranes, such as high thermal stability and easier regeneration. Ceramic membranes can be operated in harsh environmental conditions like acidic, basic, and hot solutions [96, 109]. Although polymeric supports have been extensively used in industry, due to lack of functional groups in the majority of polymeric supports, polymeric supports might not be modified with atomic layer deposition (ALD). Thus this likely restricts the use of non-polar polymeric membranes for many applications [112]. Multiple membrane interface engineering methods like plasma coating, layer by layer (LBL) assembly, and sol-gel treatment have been used to sterilize non-polar polymeric support in order to make them amenable for ALD but most of these techniques are not only expensive, but also time-consuming under operating condition [113]. Therefore, ceramic supports were selected in this study. A significant obstacle that restricts the broader application of membrane-based separation is fouling [114], where fouling is the deposition of PW components like organic and inorganic materials on the membrane surface or inside of the pores, which results in decreased permeation flux and filtration performance [115]. PW contains high amounts of organic contaminants and TDS that are derived from the decomposition of minerals and organic components [116]. For instance, TDS of PW from the Marcellus shale reaches 390,000 ppm (39%). Such high salinity causes the filtration to be more complicated, and fouling phenomena would be inevitable during PW treatment [117].

Hydrophilicity plays an essential role in the fouling phenomenon, which can be controlled to inhibit membrane fouling. The applicable methods to endow hydrophilicity are hydrophilic nanoparticle coatings, such as TiO_2 [118], Al_2O_3 [67], SiO_2 [119], graphene oxide [120], zeolite [121], and Fe_3O_4 [122] on the surface and inside the pores of the membrane. However, it is worth mentioning that such coatings can suffer from agglomeration that drastically decreases the performance of the membranes [123]. Alternatively surface modification methods have been utilized, such as plasma treatment [124], dip coating [125], surface

grafting [126], interfacial assembly [127], and surface deposition [128]. However, these traditional modification methods suffer from low stability, fragile membrane structure, restricted suitable substrates, and non-uniform surface [129].

To overcome such issues, atomic layer deposition (ALD) has emerged as a promising tool to fabricate membranes with controllable pore size and uniform structures. ALD has three advantages over conventional methods. First, the ALD process is compatible with a wide range of substrates. Second, ALD generates a uniform coating over uneven supports, which not only keeps the original pore structure of the support but also reaches complete coverage. Third, ALD allows for unprecedented control of the thickness of the coating, and can be tuned from nanometers to micrometers [129, 130]. Li et al. [131] utilized an ALD technique in order to coat Al_2O_3 on zirconia support with a pore size of ~50 nm, where they reported that the pore size of the substrate decreased with increasing ALD cycles. The deposition of 600 cycles of Al_2O_3 by ALD caused a reduction of flux from 1,698 L m^{-2} h^{-1} bar^{-1} for the pristine zirconia support to 118 L m^{-2} h^{-1} bar^{-1}, while its bovine serum albumin (BSA) rejection increased immensely from 3% to 97% [131]. By increasing the number of ALD cycles, the membrane pore size and water permeability decreases, but the rejection rate increases due to hydrophilicity enhancement [131-134]. ALD has also been used for coating polymer-based membranes [135-140].

In this work, ALD was successfully utilized as a new approach to develop ZnO coated alumina membranes with tunable hydrophilicity. Membranes were prepared with a different number of ALD cycles, i.e. thicknesses, and their pure water fluxes, TOC rejections, and anti-fouling properties were investigated. ZnO ALD was able to efficiently enhance the permeability, selectivity, and anti-fouling property of the membranes.

4.2. Experimental section

4.2.1. ZnO ALD thickness on the α-alumina support

The various cycles and ZnO coated thickness of the prepared membranes are shown in Fig. 4.1 The thicknesses of the prepared membranes were determined by ellipsometry. In this method, blank Si wafers

were run simultaneously with the membrane samples and their thicknesses subsequently measured [141]. The thickness of the ZnO thin film was measured by using Ellipsometry (VB-400 VASE ellipsometer system, J.A. Woollam Co.). Experimental Ellipsometry and reflectivity data were acquired using wavelength from 330 to 800 nm at an interval of 1 nm with incident angle of 70º. A model with a 3 layered stack consisting of ZnO film, native SiO_2 layer, and Si substrate with estimated thickness was constructed. Then, the model was fitted with an ellipsometry spectrum to obtain the thicknesses of SiO_2 and ZnO layers. Further, we validated this model by demonstrating that it correctly generates the reflectivity spectrum. Once, a monolayer of the interfacial layer is formed, the ZnO layer should be growing on top of the ZnO layer. Hence, it was concluded that the film thickness grown on Si substrate should be comparable to the film thickness grown on α-alumina substrate.

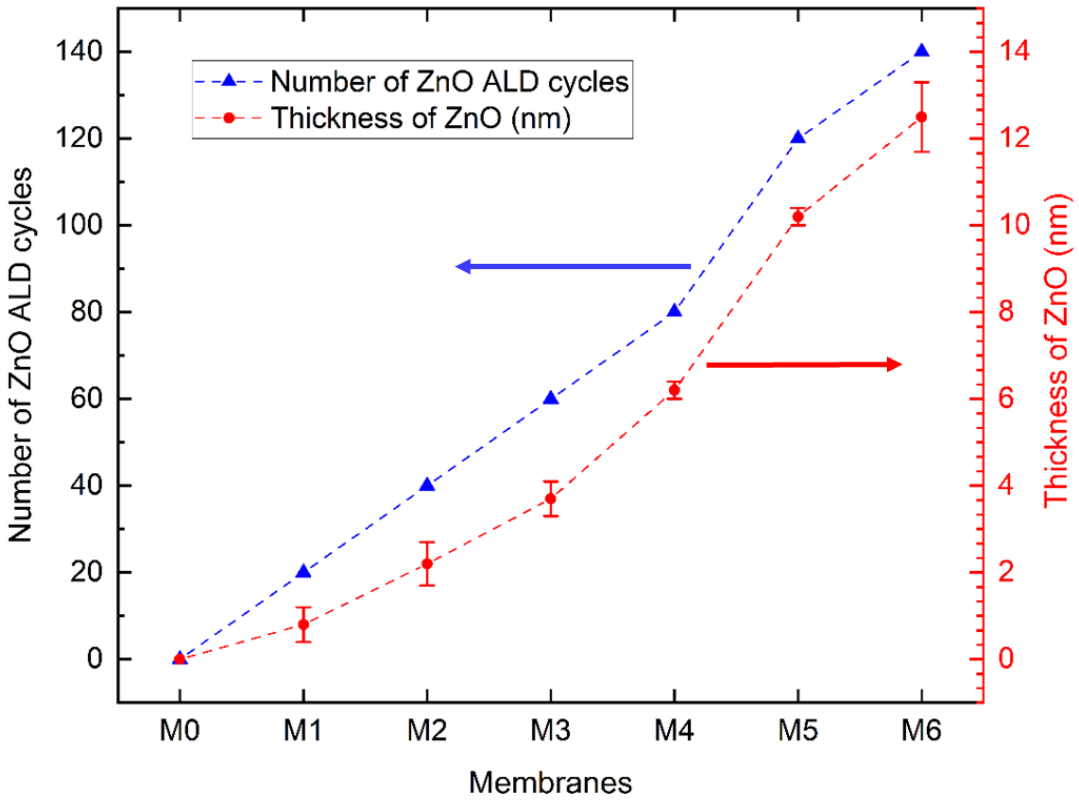

Fig .4.1 The number of ZnO ALD cycles and thickness of ZnO for the prepared membranes.

4.2.2. Membrane set-up

The setup for flow-through PW treatment is shown in Fig. 4.2 The ZnO ALD membrane was fixed to a bell-shaped glass tube using an adhesive epoxy, and then the attached membrane was immersed in PW so that the ALD treated surface was facing down. In this setup, the driving force was created due to the pressure differential across the membrane using a vacuum pump, which caused the transport of PW across the membrane. A vacuum pump (1400B-01, WELCH-ILMVAC, Denver Gardner, Laguna Hills, CA, USA) was utilized in order to maintain a vacuum in the permeate side and the pressure differential of ~1 atm across the membrane. The feed side and permeate side pressures were 1.05 and 1.3×10-6 atm, respectively. The pressure differential through the membrane was continuously monitored by a pressure gauge. The glass tube, cold trap, and vacuum pump were connected with plastic tubes. All experiments were run until the pores of the membrane were blocked completely and there was no PW flow available across the membrane. During the filtration process, the water passed through the membrane in liquid form, while the hydrophilic membrane prevented the oily components from passing through. At the same time, because of vacuum conditions in the permeate side, evaporation occurred in the permeate side at room temperature. The water that passed through the membrane was very salty; however, evaporation in the permeation side of the membrane caused the salt reduction [166]. The salty water stayed on the top of the permeate side of the membrane, and clean water evaporated and flowed to the cold trap. The evaporated water was condensed in the cold trap, and then the collected water was measured to calculate water flux.

4.2.3. Characterization

A FEI Quanta 600F field emission scanning electron microscope (SEM) equipped with an energy dispersive spectrometry (EDS) and X-ray microanalysis unit were applied to investigate the surface morphology and elemental dispersion of both the ZnO ALD membranes and cross-sections, respectively. The surface of the sample was scanned by accelerating a fine focused electron beam under maximum potential difference of 20 kV.

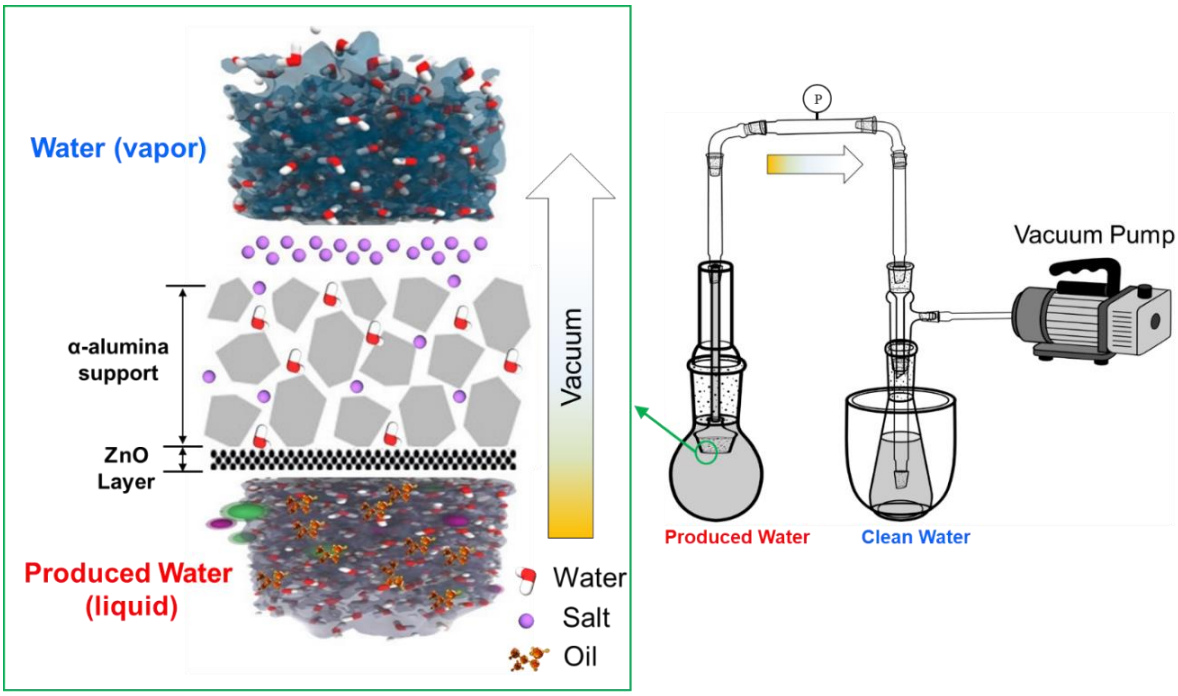

Fig. 4.2 The Schematic of flow-through produced water treatment setup.

For both SEM pictures and EDX analysis, samples were first coated by the gold layer (thickness of 200–300 Å) to avoid any charges and then analyzed. The pore size distribution of the fabricated membranes was measured using Image J software. A contact angle goniometer (Core Laboratories IFT-10) was used to calculate the hexane contact angles (HCA) and water contact angle (WCA) of the ZnO ALD membranes at room temperature. The left contact angle (θ1) and right contact angle (θ2) of the hexane drop (mostly the amount of θ1 and θ2 were so close) were calculated and the average of five contact angles measurements (each for left and right side) was taken to be the final contact angle. The same measurement was done at three different positions on the surface of the α-alumina support and the modified membranes. DR 5000™ UV-Vis spectrophotometer (HACH company, USA) was used to compute TOC parameter. The method 10173 (15 to 150 mg/L C) was applied to measure TOC of the treated PW; however, method 10128 (100 to 700 mg/L C) was used to calculate TOC of PW. A ZetaPALS ζ-potential (Brookhaven Instrument Corporation, USA) analyzer was used. DLS measurements were taken at 90° angle. A 200 µL fractional of PW

complexes were put inside the instrument. Triplicate measurements, including at least ten runs per measurement, with each run taking 1 min was applied to calculate oil droplet diameter. Finally, the vials were put inside UV-Vis spectrophotometer to read TOC. For each sample, we measured three different samples to obtain trustable data. The atomic force microscopy (AFM), MFP-3D Infinity Asylum Research, Santa Barbara, CA, USA) was used to study surface topography and membrane roughness (20 µm×20 µm). Inductively coupled plasma (ICP) model SPECTRO ARCOS (Germany) emission spectroscopy (Method 3120 B) was used to detect and measure elements such as salt components. The TDS was calculated using the following methods:

$Na + Ca + Mg + K + SO_4 + Cl + NO_3\text{-}N + HCO_3 + CO_3$ (in ppm) = TDS (ppm)

4.2.4. The produced water analysis

PW was collected from Oklahoma wells. Based on the lab analysis, TOC and TDS of PW were measured as 160 ppm and 311388 ppm, respectively. The samples were taken from the middle of the PW container and then oil droplet size was measured using DLS equipment. For consistency, the same PW was used for filtration purposes in all experiments. Fig. 4.3 shows that the overall range of particle size for the PW ranged between 98 and 446 nm.

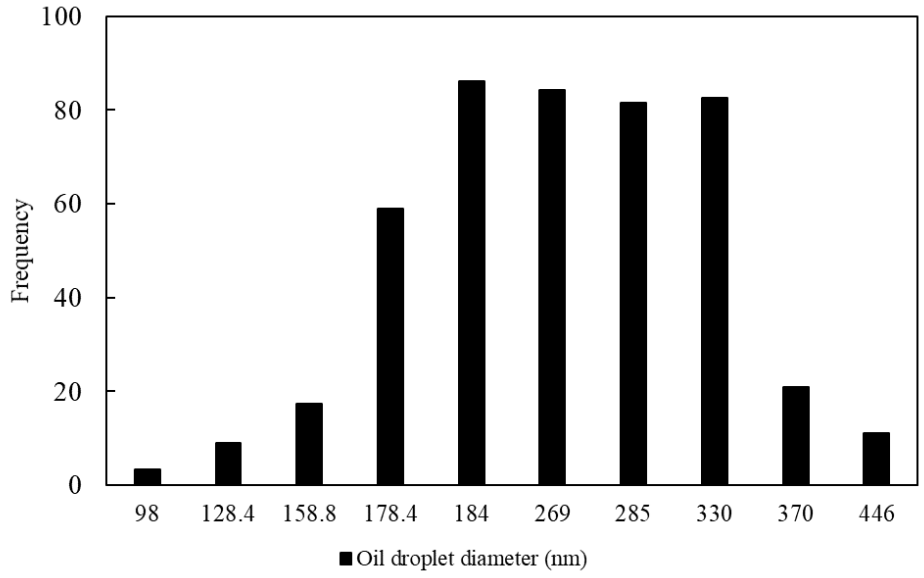

Fig. 4.3 The oil droplet diameter of PW.

4.3. Results and Discussion

4.3.1. Membrane characterization

The characterization of the α-alumina support and the ZnO ALD membranes were carried out by SEM, EDX, HCA, and AFM. To alter the thickness of the deposition layer, the deposition cycles in the ALD process were varied. SEM images were taken to investigate the effect of ZnO ALD coating on the morphology of the α-alumina supports. As shown in Fig. 4.4, the α-alumina support had a coarse and non-uniform surface, but after ZnO ALD, the membrane surface became smooth [142]. There are no notable changes in morphology between the α-alumina support and ZnO ALD membranes (Fig. 4.4a1-e1). The identical surface morphology of the α-alumina support and ZnO ALD membranes could refer to the homogeneous and conformal layer coated on the surface of the α-alumina support [137]. However, the pore size of the ZnO ALD membranes changed slightly with varying ALD cycles due to the deposition of ZnO. Measuring the pore diameter of the membranes exhibited that with increasing number of ALD, the membrane pore diameter reduced slightly, but continuously (Fig. 4.4a3-e3). The mean pore diameter reduced from 200 nm for the α-alumina support to 197.2, 193.8, 189.2, and 184.7 nm for the membranes after 40, 80, 100, and 120 ALD cycles, respectively. Moreover, the thickness of ZnO coat increased with the number of ALD cycles, which is another explanation for the reduction of the membrane pore size (Fig. 4.1). Add 10 mL of sample to a 50-mL Erlenmeyer flask. To adjust the pH, 0.4 mL of buffer solution was added to the samples to reach pH 2. The flask was put on a stirrer plate and the solution was stirred at a moderate rate for 10 min. Then, TOC persulfate powder pillow was added to acid digestion vial, the following 1 mL of the samples were added to these vials. To prepare the blank vial, 1.0 mL of organic-free water was added to acid digestion vial. All the samples were placed inside the DRB200 reactor (HACH Company) for 2 hours at 103 to 105 °C. The vials were removed from the reactor and put in a test tube rack to cool for one hour. The physicochemical properties of PW complexes were determined by utilizing dynamic light scattering (DLS) to calculate the size of oil droplets.

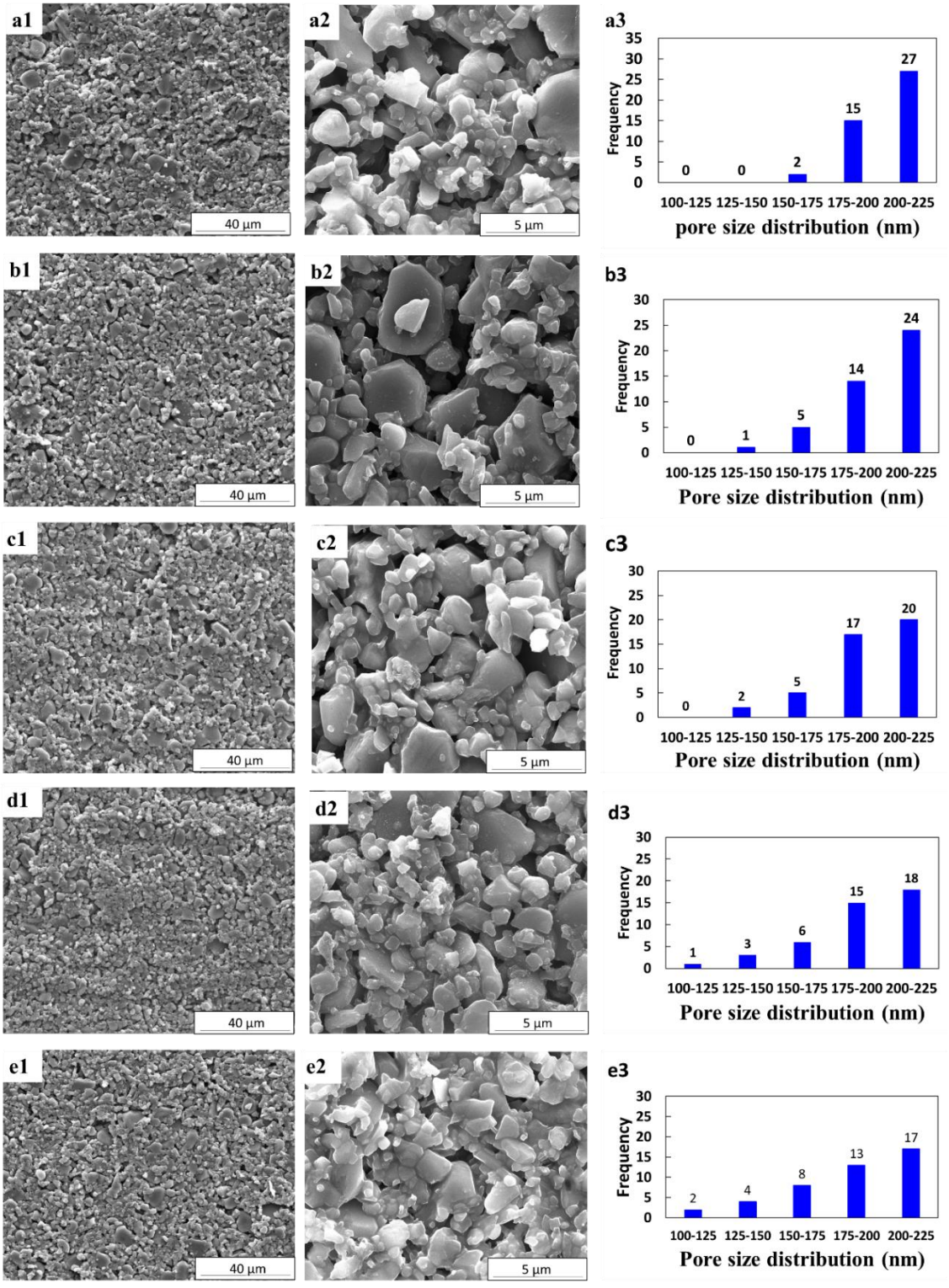
a1
40 µm
a2
5 µm
a3
Frequency
0
0
2
15
27
100-125 125-150 150-175 175-200 200-225
pore size distribution (nm)
b1
40 µm
b2
5 µm
b3
Frequency
0
1
5
14
24
100-125 125-150 150-175 175-200 200-225
Pore size distribution (nm)
c1
40 µm
c2
5 µm
c3
Frequency
0
2
5
17
20
100-125 125-150 150-175 175-200 200-225
Pore size distribution (nm)
d1
40 µm
d2
5 µm
d3
Frequency
1
3
6
15
18
100-125 125-150 150-175 175-200 200-225
Pore size distribution (nm)
e1
40 µm
e2
5 µm
e3
Frequency
2
4
8
13
17
100-125 125-150 150-175 175-200 200-225
Pore size distribution (nm)

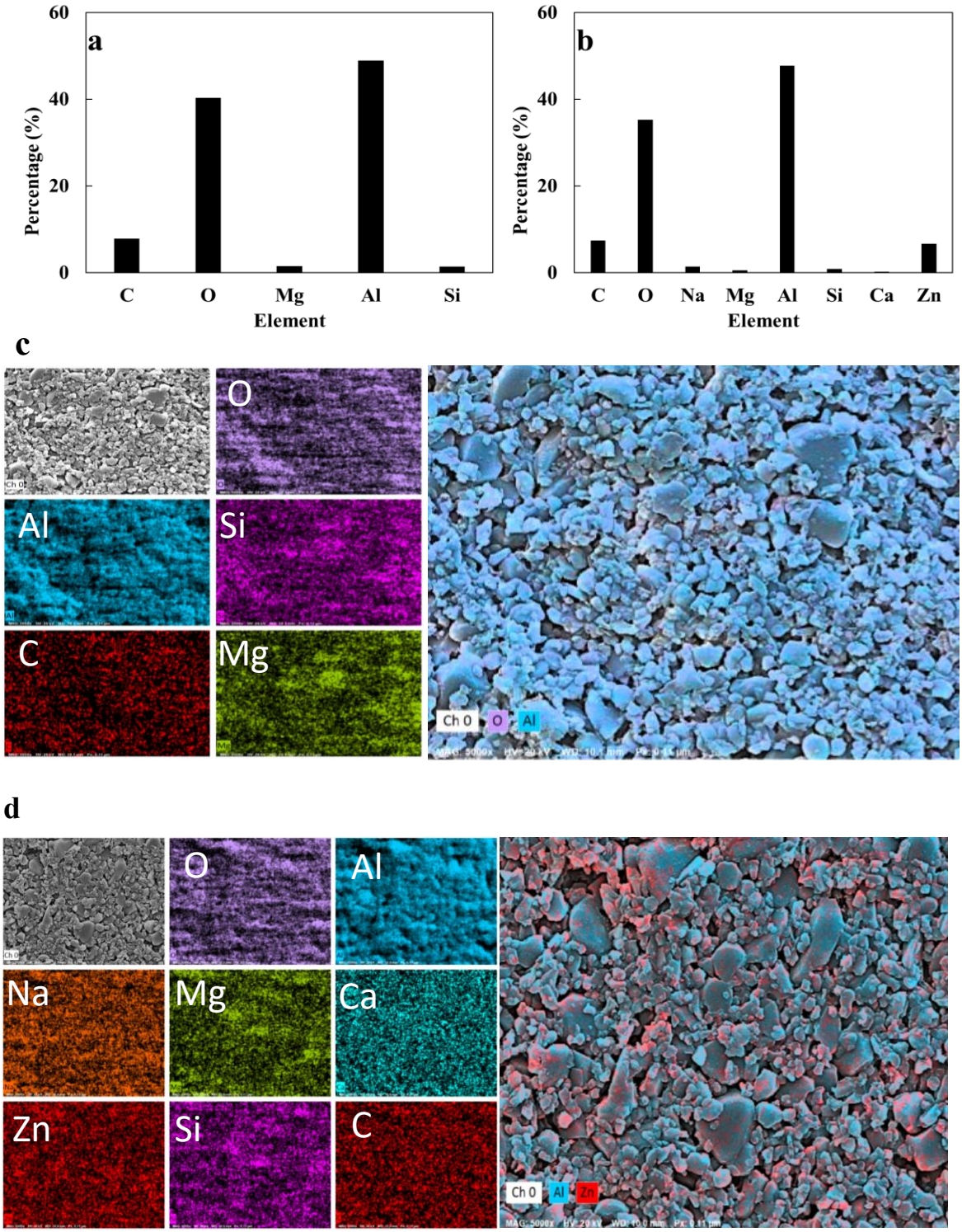

Fig. 4.5 EDS element distribution of (a) M0 and (b) M6. SEM images corresponding to element distribution of (c) M0, and (d) M6.

To investigate chemical composition of the membrane surfaces, EDS was performed on the pristine M0 and M6 membranes. In Fig. 4.5, aluminum and oxygen are the main elements in M0 [143]. The carbon peak in both M0 and M6 is attributed to carbon, which is used for sputtering before SEM. For M6, the elemental stoichiometry showed 47.76% Al, 35.22% O, 6.63% Zn, and 1.35% Na, and negligible values of Mg, Si, Ca, which verifies that ZnO has been coated on the α-alumina support. The Zn/Al ratio increased from 0% for M0 to 13.9% for M6. To further investigate the presence of ZnO, EDS cross-section elemental map distribution has been performed for both M0 and M6. In Fig. 4.6, alumina and oxygen are the only elements in the cross-section for M0. However, in Fig. 4.6b, the presence of Zn elements in M6 verified that ZnO has been coated on the surface of α-alumina support. Zn concentration near the top surface of the membrane M6 is higher than the lower part, which indicates that ZnO was coated on the top surface of α-alumina support. In addition, the cross-section elemental distribution of the prepared membranes is shown in Fig. 4.7 to observe changes in ZnO stoichiometry. The amount of Zn slightly increases from 0 to 1.98% after 20 cycles (M1) and it reached 9.77% after 120 cycles (M6).

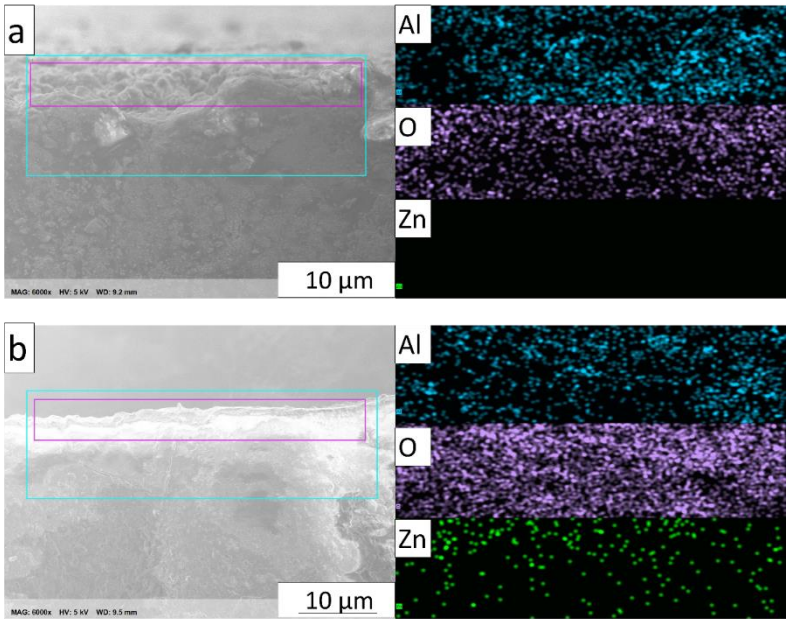

Fig. 4.6 EDS cross section elemental map distribution of (a) M0 and (b) M6

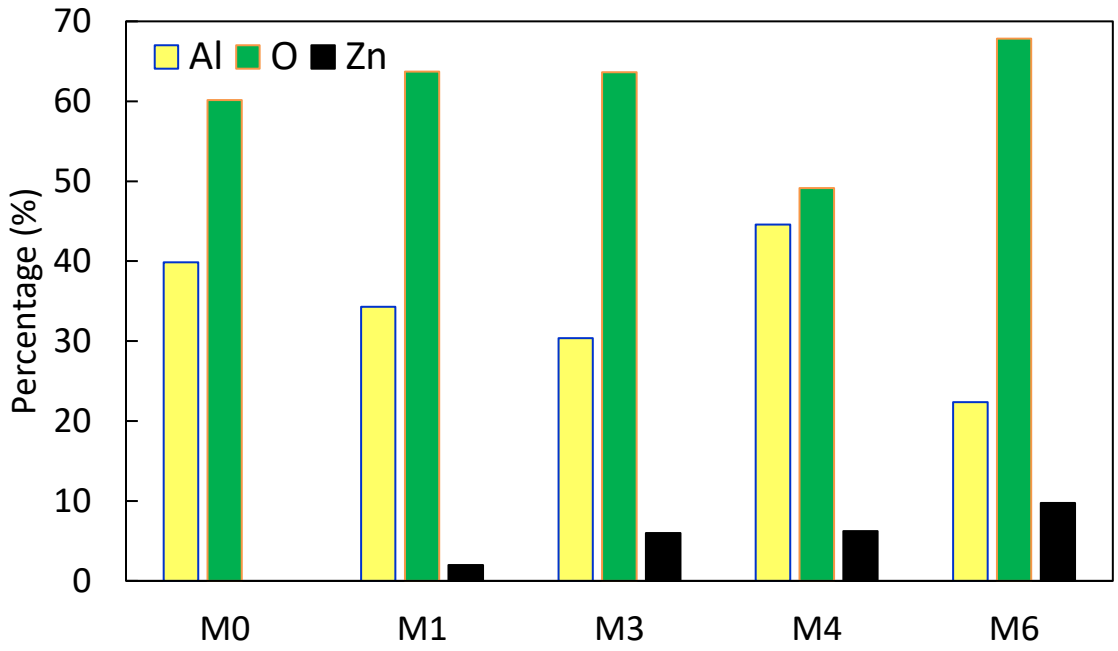

Fig. 4.7 EDS cross-section elemental distribution of α-alumina support (M0) and the modified membranes (M1-M6).

For investigating the roughness, AFM images of the α-alumina support and ZnO ALD membranes (scan size of 20 μm × 20 μm) were taken and are shown in Fig.4.8 As exhibited in Fig 4.8a, M0 has a rough surface with "hill-and-valley" morphology distributed throughout the membrane surface. After coating ZnO by the ALD technique, most of the hill-and-valleys became weak, and the surface became smooth [132]. Clearly, ZnO ALD reduced the roughness of ZnO ALD membranes in comparison with the α-alumina support (Fig. 4.8a-g). The surface roughness parameters of the membranes such as average roughness (S_a), root means square height (S_q), and the height difference between the highest peak and the lowest valley (S_t) are summarized in Table 1. The roughness decreases with increasing ZnO ALD cycles. For instance, S_a, S_q, and S_t are 509 nm, 629 nm, and 4490 nm for M0, respectively, while the corresponding roughness values decreased to 332 nm, 427 nm, and 2893 nm for M6. With reducing the surface roughness of the membranes, the trapping and sticking of contaminants into the "hill-and-valley" decreases dramatically, which likely improves the anti-fouling property of the prepared membranes [129].

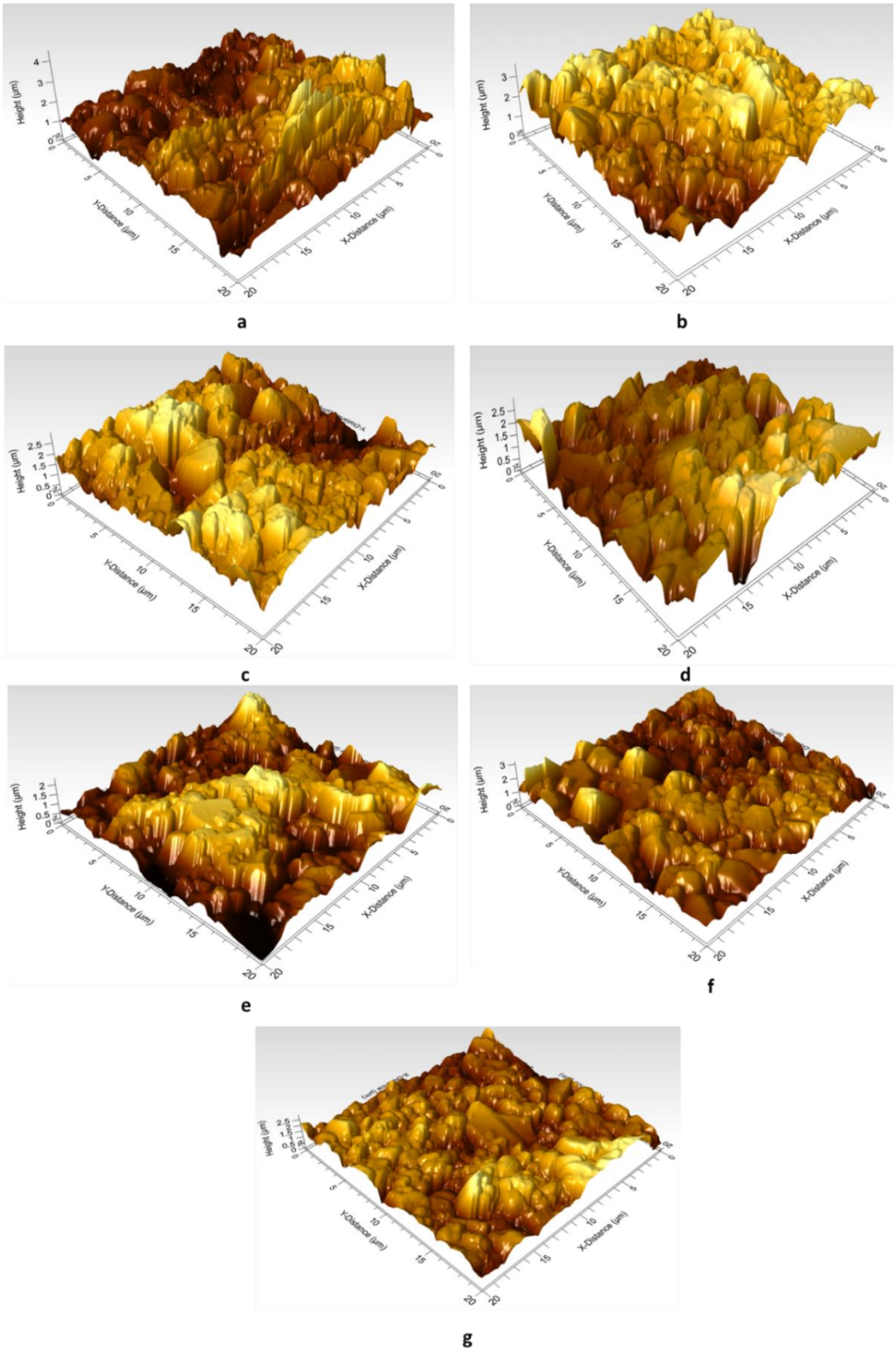

Fig. 4.8 AFM images of M0 (a), M1 (b), M2 (c), M3 (d), M4 (e), M5 (f), and M6 (g).

Table 4.1: The surface roughness of the α-alumina support and ZnO ALD membranes.

Membrane name	Roughness Parameters		
	S_a (nm)	Sq (nm)	S_t (nm)
M0	509	629	4490
M1	459	571	3621
M2	434	540	2982
M3	420	523	2992
M4	407	488	2322
M5	356	446	3174
M6	332	427	2893

The wettability of the M0 was studied by measuring HCA values. α-alumina support (M0) is hydrophilic inherently and some research confirmed this. Like for instance, Ahmad et al. measured water contact angle for the pristine α-alumina. They reported water contact angle zero for pristine alpha alumina confirming its inherent hydrophilic property [144]. In addition, because of hydrophilic nature of ZnO, Shen et al. reported that water contact angle of polyethersulfone (PES) support improved by incorporating ZnO nanoparticles into the membrane matrix structure from 80º for PES to 55º for PES/ZnO membranes with 0.4 gr of incorporated ZnO [145].

To investigate the impact of ZnO ALD coating on the wettability of membranes, instead of WCA, underwater HCA was measured using n-hexane (2 µL). Note that the hydrophilicity increases by increasing HCA values. Fig. 4.9 exhibits the underwater super-oleophobic property of both the α-alumina support and the ZnO ALD membranes. HCA increased from 165.1° (M0) to 170.5° (M6). The membranes showed the oil-fouling resistant property due to their hydrophilic property; oil did not show any tendency to stick on the surface of the prepared membranes [109, 146].

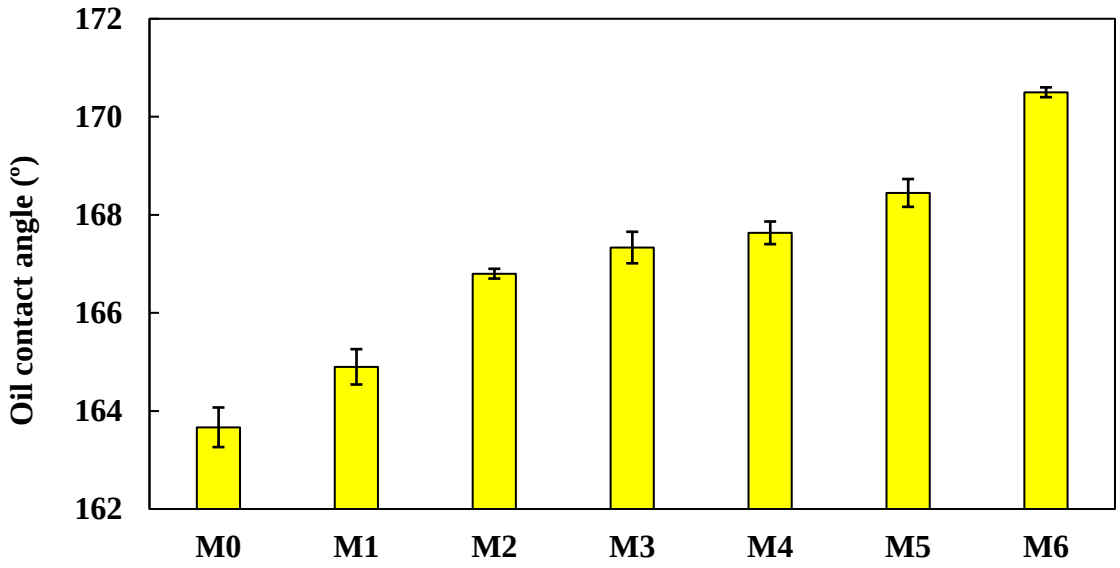

Fig. 4.9 Underwater oil contact angles of n-hexane on the pristine and ZnO ALD membranes as a function of the ZnO ALD cycles.

4.3.2. TOC rejection rate in PW

Fig. 4.10 represents both permeation flux and TOC rejection rate of ZnO ALD membranes as a function of ALD cycle. TOC rejection rate was 96.4% for M0, which could be attributed to the intrinsic hydrophilicity property of M0 (Fig. 4.9). With increasing ZnO ALD cycles, TOC rejection rate continuously increased up to 99.0% for M6. One factor that can explain the increasing trend of the TOC rejection rate is the thickness of the membranes. Increasing the number of ALD cycles leads to thicker deposition of ZnO on the membrane pore entrance and, consequently, causes a reduction of membrane pore sizes [133, 147].

In addition, hydrophilicity showed a considerable impact on TOC rejection rate and permeability [133, 142]. With an increase in the number of ALD cycles, TOC rejection rate and permeability increased. This occurs because the contact between the solution and the pore walls impacts the filtration resistance [133, 148]. As shown in Fig. 4.10, all the ZnO ALD membranes exhibited better performance in comparison with the α-alumina support. The flux increased from 147.8 ± 1.6 L m^{-2} h^{-1} for M0 to 170.2 ± 4.9 L m^{-2} h^{-1} for M2. With more ZnO ALD cycles, the flux of the

prepared membranes continued to increase until it reached a maximum value of 192.2 ± 5.3 L m^{-2} h^{-1} for M5. However, the flux slightly decreased for M6 and reached 185.7 ± 3.4 L m^{-2} h^{-1} probably because permeability of the membrane was affected by both the reduced membrane pore size and the hydrophilicity [129, 133, 138, 148]. At smaller number of ALD cycles, M1 and M2, the pore size of the membranes decreased slightly as depicted in Fig. 4.4a2-e2. Therefore, the hydrophilicity dominated water permeability for M1 to M5, which further increased the flux. For M6, the layer of ZnO kept growing thicker, the membrane pore size decreased, and the impact of the membranes pore size became more dominant in permeation values which resulted in flux reduction from 192.2 ± 5.3 to 185.7 ± 3.4 L m^{-2} h^{-1} [133, 149, 150].

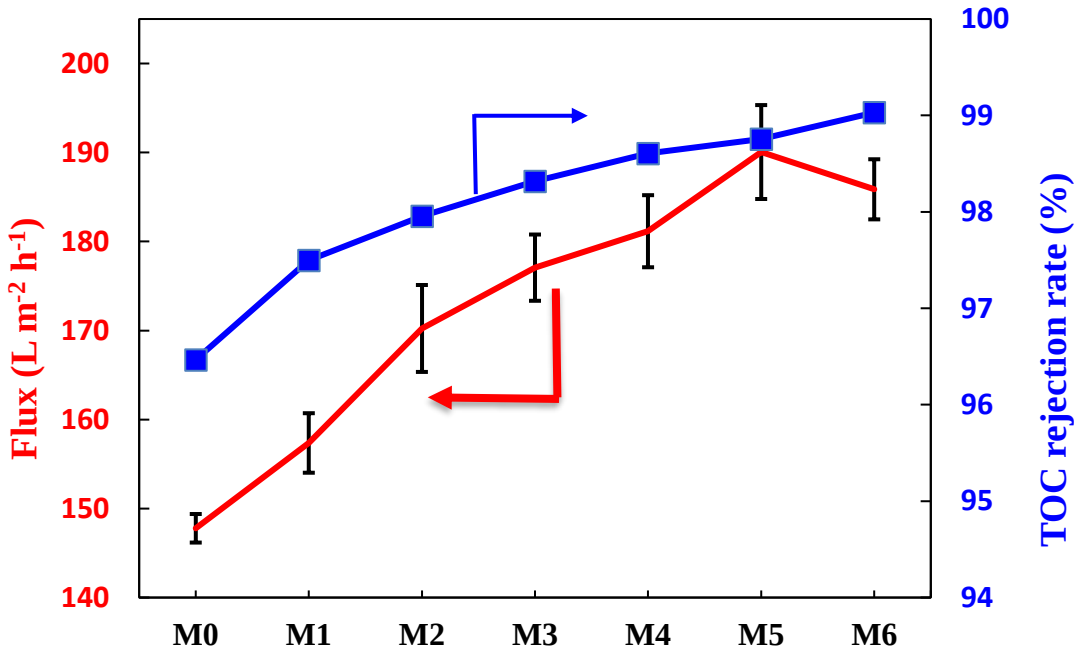

Fig. 4.10 Effects of ALD ZnO cycles on water flux and TOC rejection rate.

4.3.3. TDS rejection rate in PW

The results of the α-alumina support and the ZnO ALD membranes on desalination are shown in Fig. 4.11 TDS in PW is high, 311388 ppm, which is not suitable for drinking water and agricultural purposes based on EPA regulations [151]. Because of its high total dissolved salts, high sodium level, and high boron content, PW is not recommended for livestock watering and crop irrigation,

respectively (Table 4.2). The PW water has greater Na concentration (89453 ppm) than EPA Livestock Water Limits guideline, and it is recommended to keep Na concentration less than 1000 ppm. In addition, the PW water exceeds the guideline of 5mg/L for boron, which is likely harmful able for some livestocks. Excess boron in the diets of livestock may decrease feed consumption and cause weight loss [151]. In the flow-through PW treatment process, multiple factors such as hydrophilicity, membrane thickness, and pore sizes of the membrane play essential roles in membrane salt reduction and water permeability [152, 153]. Although TDS decreased to 53205 ppm in M0 by the flow-through process, the PW quality (permeate) is not suitable for livestock and irrigation watering (Table 4.2) [151, 154]. As shown in Fig. 4.11, with increasing the number of ZnO ALD cycles, TDS values gradually decreased, and the permeate reached the standard value for agriculture-based EPA regulations. After doing 40 cycles of ZnO ALD, the permeant contained low enough total dissolved salt and sodium content which is suitable for livestock and irrigation watering (Table 4.2) [151].

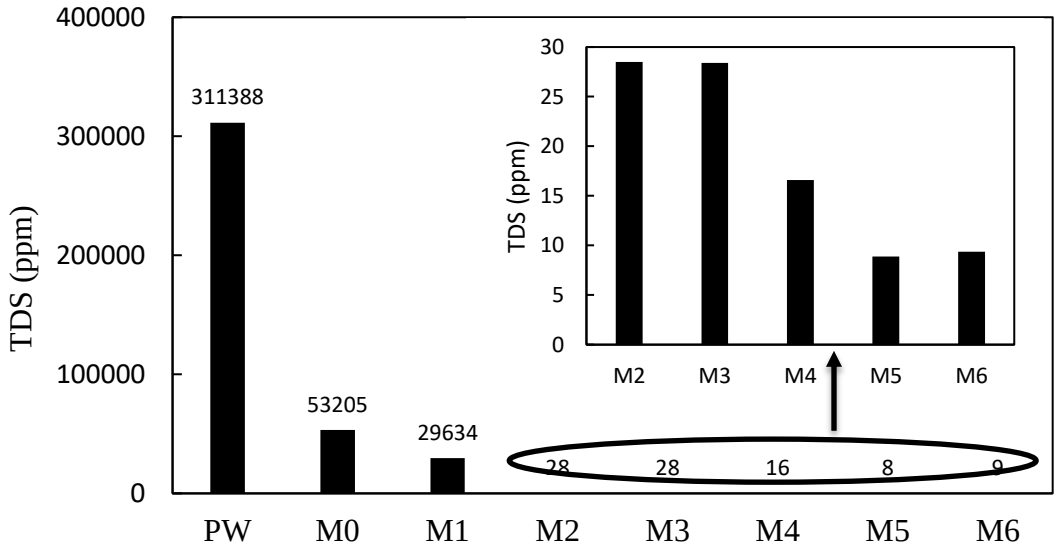

Fig. 4.11 Analysis of membrane performance efficiencies for the desalination of the produced water.

Table 4.2: Analysis of produced water and treated produced water using ZnO ALD membrane (40 cycles).

Analysis	Produced water	Treated after ZnO ALD membrane (40 cycles)	EPA Livestock Water Limits
B	47.5 ppm	0.2 ppm	< 2.4
Ca	22790 ppm	7 ppm	No Guidelines
Cl	194971 ppm	6.5 ppm	<250 ppm
Cu	0.06 ppm	< DL	<0.5 ppm
Fe	0.03 ppm	< DL	No Guidelines
Mg	2649 ppm	0.04 ppm	No Guidelines
Mn	1.8 ppm	< DL	No Guidelines
NO3-N	0.3 ppm	< DL	<100 ppm
K	1309 ppm	< DL	No Guidelines
Na	89453.3 ppm	3.3 ppm	<1000 ppm
SO_4^{2-}	189.4 ppm	0.2 ppm	<1000 ppm
Zn	0.03 ppm	< DL	<25 ppm
EC	235000 µmhos/cm	35.6 µmhos/cm	No Guidelines
Hardness Class	Very Hard	Soft	No Guidelines
pH	5.9	6.7	5.5 - 9
TDS	311388 ppm	28.5 ppm	3000 ppm
DL: Detection Limit			

4.3.4. Anti-fouling properties of the membranes

Membrane fouling is a significant problem that limits the durability and efficiency of the membranes. Membrane fouling is caused by the precipitation of contaminants (particulates or molecules) on the surface and within the pores of the membrane [155]. As shown in Fig. 4.12, after 1 h of separation of PW, a huge amount of contaminants were precipitated on the surface of the membrane, and completely blocked the pores of the membrane.

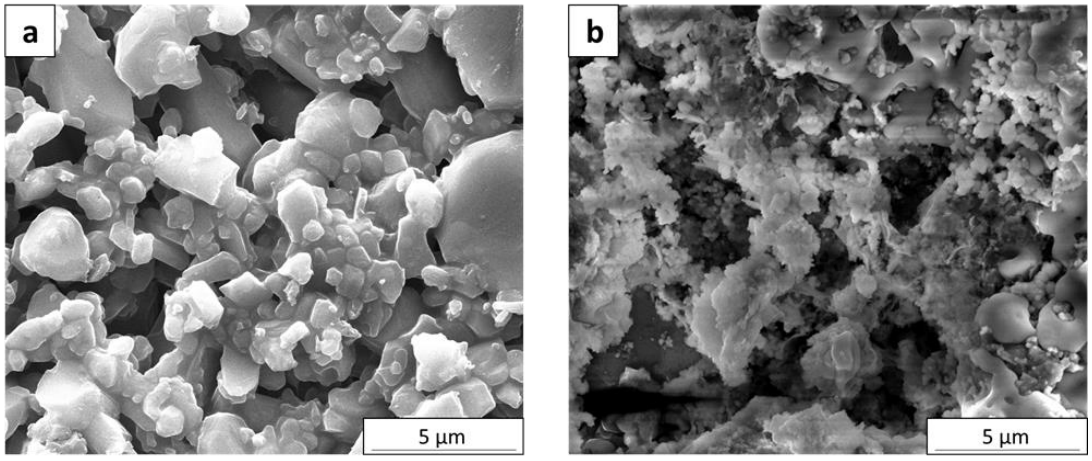

Fig. 4.12 The morphology of M0 (a) before and (b) after 1 h operation of PW membrane filtration.

This phenomenon can cause a reduction in membrane performance and increase the flow resistance across the membrane. Fouling on the membranes was investigated using characterization and performance tests. Fig. 4.13a and b show EDS data for M0 and M6, respectively. There are contaminants such as boron, oxygen, silicon, chlorine, calcium, iron, and sulfur stuck on the surface on M0. Similarly, these foulants were present on the surface of M6. However, the atomic percentage of contaminants on M6 is lower than M0, which indicates that ZnO ALD improved the fouling-resistant property. As mentioned, with increasing ALD cycles, the hill-and-valleys of the membranes decreases (Table 4.1), which likely helps in improving the anti-fouling factor because there are fewer vacant spaces for the contaminants to be precipitated [133, 138]. Another explanation regarding the anti-fouling property can be contributed to the alumina peak. Based on Fig. 4.13c, alumina peak intensity in M0 is weaker than M6, which contributed to the higher amount of foulants on the surface of M0 in comparison with M6. In this case, contaminants blocked the surface of M0, and the EDS beam could not detect the surface of M0 as efficiently as M6 [132]. The atomic percentage of contaminants such as B, Ca, Na, and Fe on the surface of M0 are more than M6, which shows M6 has a better anti-fouling property than M0.

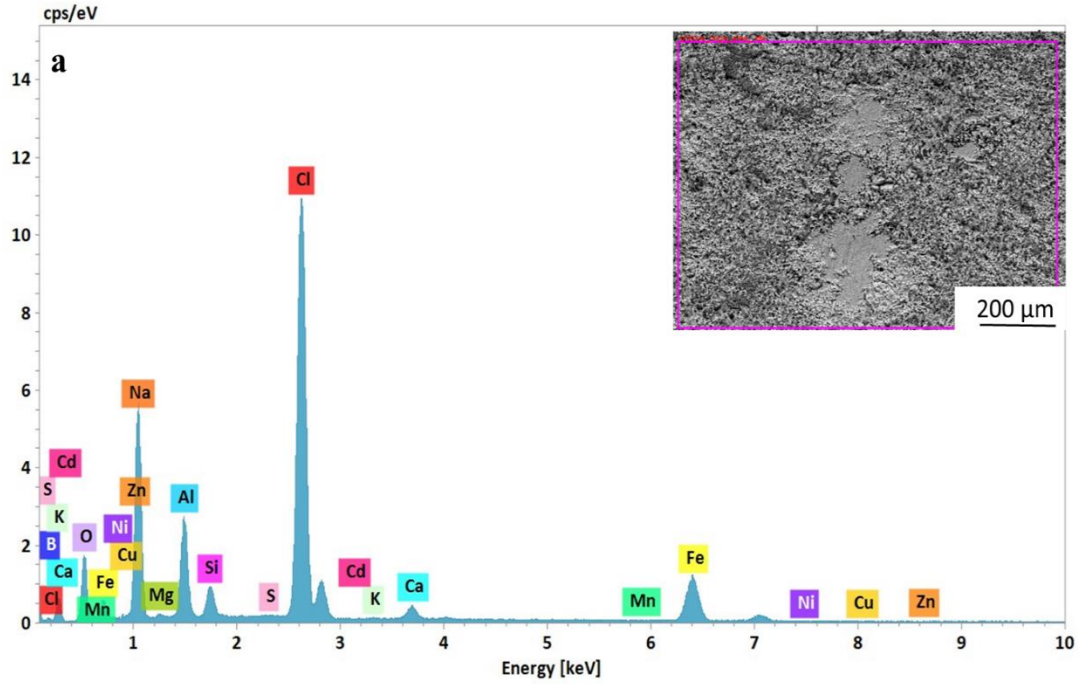
cps/eV
a
200 µm
Cl
Na
Cd
S
Zn
Al
K
Ni
O
B
Cu
Si
Ca
Fe
Cd
Ca
Fe
Cl
Mn
Mg
S
K
Mn
Ni
Cu
Zn
Energy [keV]

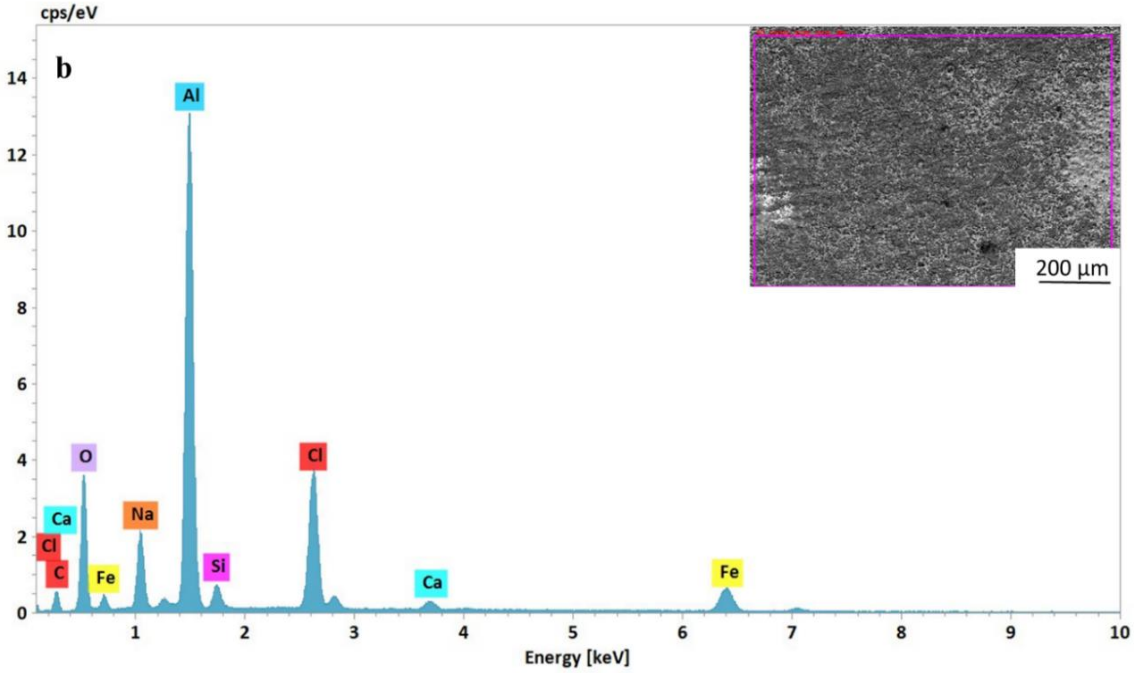
cps/eV
b
200 µm
Al
O
Cl
Ca
Na
Cl
C
Fe
Si
Ca
Fe
Energy [keV]

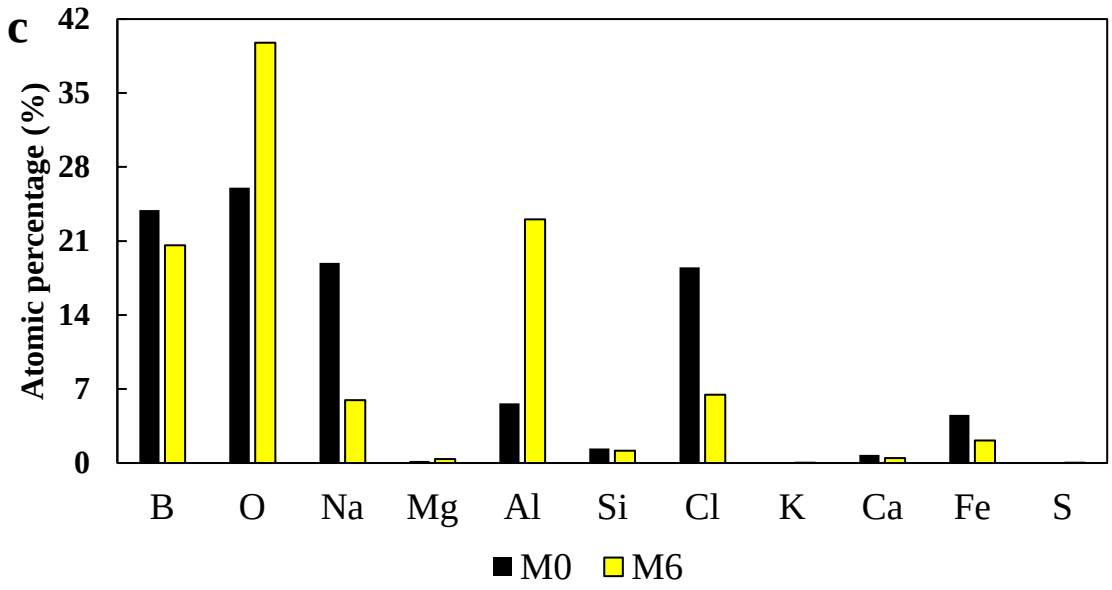

Fig. 4.13 EDS elemental distribution of top surface of (a) M0, (b) M6, and (c) EDS atomic percentage of M0 and M6 after 1 h operation of PW membrane filtration.

An FRR parameter was used to study the fouling behavior of the ZnO ALD membranes. To calculate *FRR*, we applied three steps: after 1 h pure water filtration, PW was filtered for 1 h, and finally, the pure water was filtered for another 1 h [156]. Fig. 4.14 exhibits FRR values for pristine and ZnO ALD membranes. All ZnO ALD membranes showed better FRR than the pristine membrane, which can be ascribed to higher hydrophilicity [157]. The higher hydrophilicity of ZnO ALD membranes is less oleophilic, which caused the reduction of oily foulants on the surface of the ZnO ALD membranes [109, 133]. M0 exhibited the lowest *FRR* value of 93.2 ± 0.54%, while *FRR* values of all ZnO ALD membranes were higher than 96.5%, and it reached the maximum amount of 99.5 ± 0.26 % for M5. The FRR results are consistent with the analyses and characterization results, such as HCA and roughness values. Increasing ZnO ALD cycles caused an increase in HCA values, which means that the ZnO ALD membranes have a lower inclination toward oils, and oil foulants were precipitated less on the membrane surface [158]. Roughness is another parameter affecting *FRR* values. Based on Table 1, the ZnO ALD converted the rough and

uneven surface of the pristine membrane to a uniform and smooth surface [136, 138]. Hence, pollutants in the PW, such as heavy metals and salts, did not have enough space in hill-and-valleys to be precipitated. In this case, *FRR* of ZnO ALD membranes increased because their anti-fouling property increased.

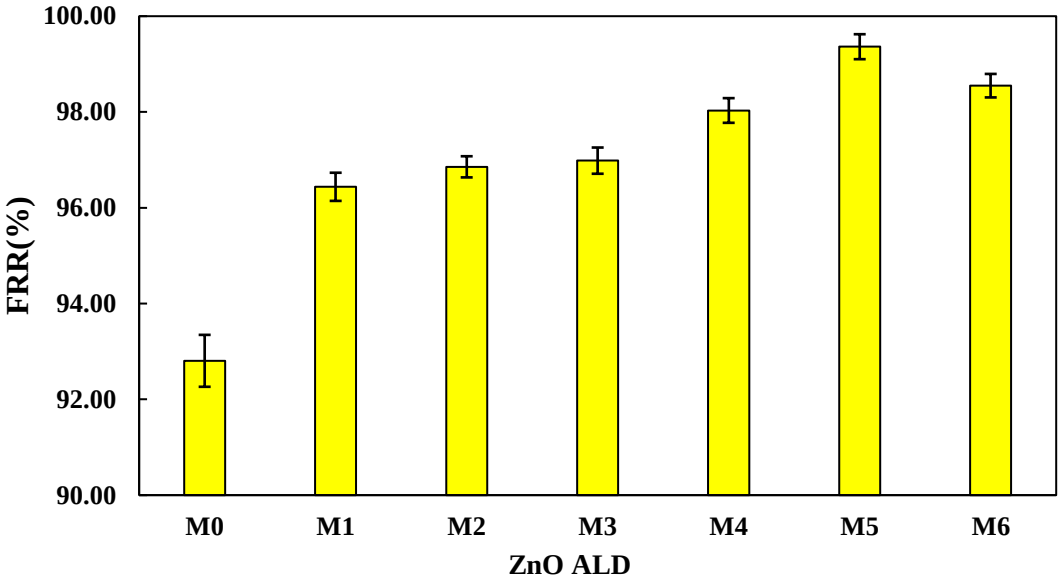

Fig. 4.14. Flux recovery ratios (*FRR*) of the membranes as a function of ZnO ALD membranes.

In order to better assess the fouling-resistant property of the ZnO ALD membranes, the membranes were tested to treat PW to the point that their pores were entirely blocked and the flux drastically reduced. As shown in Fig. 4.15, M0 filtered PW only for 2 h, and the water flux reached from 147.7 ± 1.7 L m^{-2} h^{-1} during 1 h of operation to 26.3 ± 6.1 L m^{-2} h^{-1} by the end of 2 h operation. Because of the high roughness of the membrane surface, the foulants can be confined inside the valleys, which caused reduction of the performance (Table 4.1) [136, 137]. However, separation time increased from 2 h to 4 h for ZnO ALD membranes M3 and M5, respectively. With more ZnO ALD cycles, the surface of ZnO ALD membranes became smoother [142]. Therefore, the permeation operating time of ZnO ALD membranes (M1-6) increased, which prolonged the lifetime of the membranes.

M5 worked for 4 h with the flux reaching 190 ± 5.3 L m^{-2} h^{-1} during 1 h of operation to 65 ± 6.97 L m^{-2} h^{-1} at the end of 4 h of operation, which showed tremendous improvement in comparison with the alumina support. Clearly, the membrane lifetime is dependent on the anti-fouling property of the membrane, which can be easily improved through ZnO ALD.

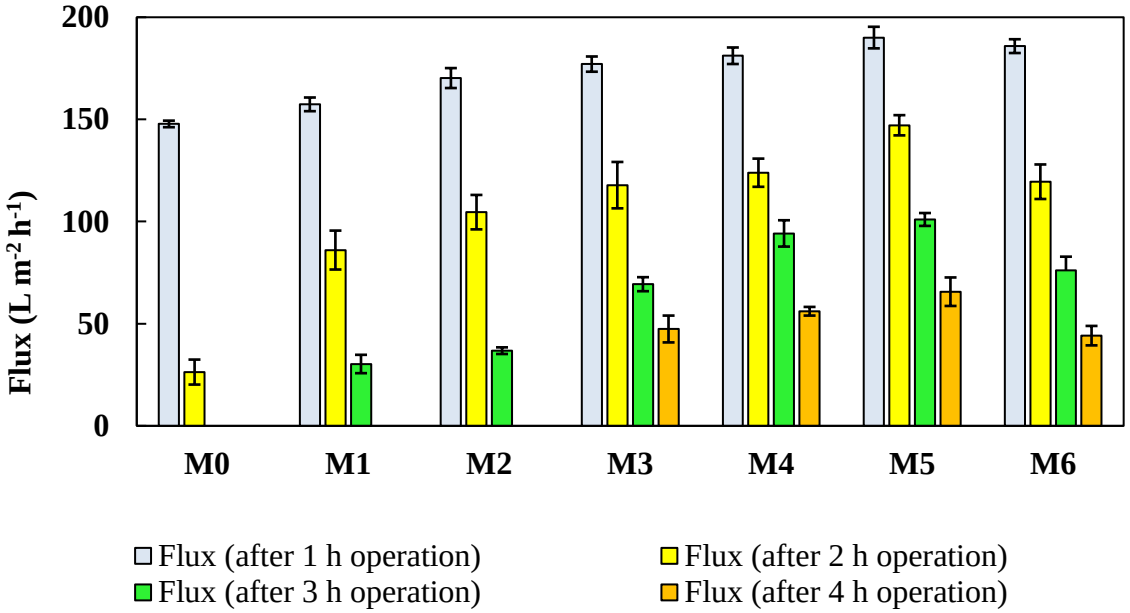

Fig. 4.15. Flux vs. time for the pristine and ZnO ALD membranes.

4.4. Conclusion

ZnO was coated on the α-alumina support using ALD, which helped improve membrane hydrophilicity and reduced the roughness and pore size of the membranes. Contact angle measurements showed that the oil contact angle increased from 165.1° for the α-alumina support to 170.5° for ZnO ALD membrane (120 cycles), which enhanced pure water flux. Membrane pore size is another main factor that significantly affects flux. The flux increased from 147.8 ± 1.6 L m^{-2} h^{-1} for M0 to 192.2 ± 5.3 L m^{-2} h^{-1} for M5. We assumed that for M0-M5, the hydrophilicity dominated water permeability, which caused an enhancement in flux value. With higher hydrophilicity, water passes through the membrane faster which resulted in flux enhancement. However, the flux slightly decreased for M6 and reached 192.2 ± 5.3 L m^{-2} h^{-1} for M5 to 185.7 ±

3.4 L m^{-2} h^{-1} for M6 because the layer of ZnO kept growing thicker, the membrane pore size decreased. Consequently, the impact of the membranes pore size became more dominant in permeation values.

ZnO ALD also helped reducing the roughness of the membrane, which improved the anti-fouling property. Although ZnO atomic layer deposition (ALD) has shown considerable improvement against membrane fouling in our current work, it is not the ultimate solution to overcome the membrane fouling problem. Recent work by Zheng et. al [159] describes the emerging role of methods and materials from photocatalytic pollutant degradation to alleviate membrane fouling problems. In addition, Zhang et. al [160] used photocatalysis with membrane separation to significantly reduce membrane fouling. A visible light-activated photocatalytic film was prepared by N_2 doping on TiO_2 deposited (via ALD) ceramic support and a stable membrane operation was observed. By reducing the surface roughness of the membranes, the trapping and percipitation of contaminants into the "hills-and-valleys" decreased dramatically. TOC rejection and TDS were 96% and 311388 ppm for M0 and 99% and 10 ppm for M5, respectively. The drastic reduction in TOC and TDS values was a result of improved membrane hydrophilicity and decreased membrane roughness by ZnO ALD. Purified water met the irrigation standards of the Environmental Protection Agency (EPA), and thus ZnO ALD modified membranes provides a potentially sustainable and robust solution for the purification of PW. The reusability and longevity of the ZnO ALD membranes was enhanced in comparison to the α-alumina support.

CHAPTER V

IMROVING CELLULOSE ACETAT (CA) MIX MATRIX MEMBRANES BY INCORPORATING HYDROPHILIC MIL-101-NH2 NANOPARTICLES FOR TREATING DYE/SALT SOLUTION

Industrial wastewater, especially in biomedical and textile industries, generates a huge amount of extremely polluted wastes that contain harmful dyes, toxic macromolecules, inorganic salts such as NaCl, suspended solid particles, acids, and other hazardous chemicals. The complex structure and chemical stability of such pollutants make the treatment process challenging [161]. Generally, several methods have been used to treat textile wastewater, including physical, chemical (Fenton oxidation, chemical coagulation, and electro-coagulation), and biological treatment (aerobic and anaerobic degradation) [162, 163]. Drawbacks of these methods involve long process time in case of biological treatment, sludge generation in oxidation process, and high energy demand for adsorbent recovery. However, membrane technology, being a pressure-driven physical separation process can benefit from low energy requirement while providing selectivity, lower maintenance, and operation simplicity, and its modular design allows handling of varying feed quality and volume [164, 165].Polymers have been widely utilized in fabricating membrane materials because of their immense variety, low cost, and ease of fabrication process [166]. Among reverse osmosis (RO), nanofiltration (NF), and ultrafiltration (UF), NF membranes serves best for wastewater treatment, because of higher permeance compared to RO.

However, RO membranes are significantly high separation capabilities for salt and other solute compared to UF membranes [32]. Among various polymers, cellulose acetate (CA) is one of the most commonly utilized polymers due to its unique specification such as high selectivity, low cost, outstanding biocompatibility, durability, thermal stability, and abundance in nature [33, 34]. CA is somewhat hydrophilic due to hydroxyl groups in its structure, providing better film-forming and oleophobic properties [35, 36]. Although CA shows some hydrophilic property, membrane fouling regarding CA is still considered one of the biggest issues because of inadequate hydrophilicity allowing solute molecules to stick to the surface. Therefore, membrane modification is necessary to enhance membrane performance [11, 12].

Fouling in NF membrane is the major challenge limiting their application in large scale. Making membrane more hydrophilic is found to be an effective way to mitigate fouling, hence not drastically reducing flux. Techniques like surface coating; surface chemical treatment, surface grafting, and polymer blending have been studied to enhance membrane hydrophilicity [12, 167]. Surface coating runs the risk of peeling of the hydrophilic coating under harsh crossflow conditions and this technique is only appropriate for high molecular weight polymers [168-170]. Although chemical modification involving addition of polar groups, for example –OH, –COOH, and $–NH_2$ or grafting hydrophilic monomers, is effective, but it requires, often sophisticated, post-processing step after membrane fabrication, that limits membrane scaleup [171-174]. Polymer blending, where hydrophilic nanoparticles are directly mixed into the polymer matrix is a facile technique applied for membranes preparation that is easily implemented in the current commercial fabrication techniques [13].

To improve hydrophilicity, nanoparticles are embedded into the polymer blend, called mixed-matrix membranes, which help improve membrane performance such as permeability, and fouling-

resistant property, increasing membrane longevity [14, 15]. However, mixed-matrix membranes using inorganic nanoparticle faces two main challenges. First, particles, if large, tends to aggregate, leading to an uneven membrane surface, hence increasing risk of fouling. Secondly, the low affinity between the inorganic nanoparticles surface and the polymer chains leads to uneven dispersion, causing nanoparticle clusters in the polymer matrix, failing to impart uniform desirable property throughout the membrane [175, 176]. On the contrary, organic nanoparticles are a promising alternative because of their higher interaction with polymers, which could be attributed to ample hydrophilic functional groups in them. These hydrophilic groups enhance hydrophilicity and fouling-resistant of the as-prepared membranes. These nanoparticles include metal-organic framework [16], chitosan [17], polystyrene [18], and polydopamine [19].

Vatanpour *et al.* [177] improved the CA membrane by incorporating ZnO@graphitic carbon nitride nanocomposite to obtain pure water flux (PWF) of 51.3 LMH, which was 2.1 times greater than pristine CA at same given driving force, while demonstrating highest rejection rate for bovine serum albumin (BSA) and Blue 3R dye (Reactive Blue 50) rejections. Polyethersulfone (PES) nanofiltration membrane was modified in terms of antifouling behavior by incorporating nanocrystalline Ce(III) MOF (Metal Organic Framework) [178], and pure water flux and dye rejection rate were reported 21.2 LMH and 99%, respectively. Vetrivel et al. [179] studied CA modification using embedding hydrous manganese dioxide (HMO) nanoparticles, and the modified membranes showed PWF (143.6 LMH), BSA rejection (95.9%), and FRR (93.3%). CA/nanohydroxyapatite membranes were synthesized for NaCl rejection, and the modified membrane exhibited NaCl rejection rate of 99.1% and water permeability of 34.96 LMH bar. In this research, MIL-101(Cr)-NH_2 nanoparticles were selected to be embedded into the CA matrix to develop nanocomposite membranes due to their low cost, mesoporous zeotype architecture with mesoporous and microporous cages windows, a giant cell volume, huge surface area, hydrophilicity, and numerous unsaturated chromium [180]. Only a few works have been published on applying MIL-101(Cr) nanoparticles in the water treatment area [181].

The major goals of this study are as follows: (1) To achieve enhanced efficiency and antifouling properties of synthesized membranes; (2) To synthesize new CA/MIL-101(Cr)-NH_2 membranes utilizing phase inversion; (3) To determine the optimal concentration of synthesized nanoparticles (MIL-101(Cr)-NH_2), which were incorporated in the CA matrix. Synthesized nanoparticles were characterized by Fourier transform infrared (FTIR) spectroscopy, Transmission electron microscopy (TEM), and scanning electron microscopy (SEM). The structure and chemical stoichiometry, hydrophilicity, surface morphology and separation performance of the synthesized membranes, and the pure water, dye, and BSA flux were measured comprehensively.

5.2. Experimental

5.2.1. Materials

Cellulose acetate (Mn = 50,000 Da), polyethylene glycol (PEG, MW = 4000 Da), N, N-Dimethylformamide (DMF, 99.8%), chromium (III) chloride hexahydrate (>96%), terephthalic acid, ammonium fluoride (>98%), epichlorohydrin (>99%), and sodium hydroxide and bovine serum albumin (BSA) were purchased from Sigma Aldrich® Chemical Co (Germany). Ammonia solution 25% was purchased from Merck (Germany). Methyl blue ($C_{37}H_{27}N_3Na_2O_9S_3$, MW = 799.8 g/mol) was provided from Alfa Aesar (England).

5.2.2. Synthesizing MIL-101(Cr)-NH_2 nanoparticles

MOF was fabricated via hydrothermal reaction of chromium (III) chloride hexahydrate, terephthalic acid (TPA), and deionized (DI) water (the reactants molar ratios were chromium(III) chloride hexahydrate:TPA:H_2O = 1:1:300), as described elsewhere [180]. The precursor solution was placed inside a hydrothermal autoclave reactor and heated in an oven at 210 °C for 8 h. After hydrothermal synthesis, the synthesized MOF was purified and collected in three steps. First, 1 g of the synthesized MIL-101(Cr) was dispersed in 300 mL of deionized water and stirred for 5 h at 70 °C. Subsequently, the MIL-101(Cr) nanoparticles were separated by centrifuge (4000 rpm, 10 min) and dried in the oven for 6 h. Secondly, the MIL-101(Cr) nanoparticles were added to 250

mL of ethanol, and stirred for another 3 h at 60 °C and collected by centrifuge (4000 rpm, 10 min). In the last step, the MOF collected from the second step was loaded to 150 mL of 30 mM NH_4F solution and stirred for 10 h at 60 °C [182]. The final solid purified MOF was filtered with a centrifuge (4000 rpm, 20 min), washed sufficiently with hot water, and placed in an oven overnight. The synthesized MOF was functionalized by adding 1.1 g of MIL-101(Cr) to 100 g of water and sonicated for 2 minutes. Then, 5 molar NaOH was added to the solution and then stirred vigorously for 15 minutes. Afterwards, 70 ml of epichlorohydrin was added to the solution and stirred for 24 hours. Finally, 60 ml of ammonia was poured in the solution and then stirred for 1 hour. The desired product was separated by centrifuge (4000 rpm, 30 min) and washed with DI water, and then MIL-101(Cr)-NH_2 as final product was dried at 60 °C in an oven [181].

5.2.3. Membrane preparation

The CA/MIL-101(Cr)-NH_2 membranes were prepared using the phase inversion technique (Fig. 1.3). First, a certain amount of the fillers (0.01, 0.05, 0.1, 0.2, 0.5, and 1 wt.%) relative to the CA were added to DMF and the solution sonicated for 30 min. The concentration of the casting solution is summarized in Table 5.1. Next, PEG (3 wt.%) and the CA (18 wt.%) were loaded into the solution by stirring at 30 °C for 24 h. After that, the casting solutions were put in an oven at 60 °C for degassing. Finally, the casting solutions were cast on glass with a casting knife of 150 μm thickness. The resulting membrane sheets were immediately immersed in a distilled water bath as nonsolvent at room temperature. After coagulation, the resulted membranes were rinsed and placed in fresh distilled water until tested. To determine the optimal concentration of synthesized nanoparticles (MIL-101(Cr)-NH_2), which were incorporated in the CA matrix. Synthesized nanoparticles were characterized by Fourier transform infrared (FTIR) spectroscopy, Transmission electron microscopy (TEM), and scanning electron microscopy (SEM). The structure and chemical stoichiometry, hydrophilicity, surface morphology and separation performance of the synthesized membranes, and the pure water, dye, and BSA flux were measured comprehensively.

Table 5.1. Different concentrations of casting solution for the preparation of the membranes.

Membrane	**MIL-101-Cr (%wt.)**	**CA (%wt.)**	**PEG (%wt.)**	**DMF (%wt)**
M0	0	18	3	`79
M0.01	0.01	18	3	72.97
M0.05	0.05	18	3	72.94
M0.1	0.1	18	3	72.91
M0.2	0.2	18	3	72.88
M0.5	0.5	18	3	72.85
M1	1	18	3	72.82

5.2.4. Membrane characterization

The bonding behaviors of the synthesized nanoparticles were studied by Fourier-transform infrared (FT-IR) spectroscopy (Nicolet iS50 FTIR spectrometer, Thermo Scientific, Waltham, MA, USA) in the range of 4000-500 cm^{-1}. A FEI Quanta 600F field emission scanning electron microscope (SEM) connected with an energy dispersive spectrometry (EDS) and X-ray microanalysis unit were used to study the surface morphology and elemental stoichiometry of both the CA/MIL-101(Cr)-NH_2 membranes top surfaces and cross-sections. Before capturing SEM and EDX pictures, samples were initially coated with the gold layer (thickness of 200–300 Å) to avoid charging. Water contact angle (WCA) was measured using a goniometer consisting of a digital microscope positioned horizontally (make: Dino Lite; model: AM7815MZTL), a cold background light source with

diffusor, and a height adjustable stage. A 5 µL water droplet was gently put on the surface of the membrane, and then the image of the droplet was captured. A minimum of five contact angle measurements on each membrane was obtained, and the average values with standard deviations are reported. The atomic force microscopy (AFM), MFP-3D Infinity Asylum Research, Santa Barbara, CA, USA) was used to study surface topography and membrane roughness (20 µm×20 µm).

5.2.5. Performance of nanofiltration membranes and pore size

The performance of the fabricated membranes was investigated by using a lab-scale dead-end filtration set-up. The prepared membranes (1.7 cm^2) were put between two Teflon sheets and was sealed completely by plastic O-ring and epoxy resin. Before running the experiment, the fabricated membranes were first compressed at a pressure of 5 bar, and then the separation experiments were run at a pressure of 4 bar using pure water. The steady permeation flux, J, was calculated as follows:

$$J = \frac{V}{A \times t} \quad (1)$$

where V is the total volume of permeate (L), A is the effective surface area of the membrane (m^2), and t is the duration of the filtration process (h). The rejection rate (R) was defined by the following equation:

$$\eta = 1 - \frac{C_i}{C_0} \quad (2)$$

where η stands for the rejection rate, and C_0 and C_i are the feed and permeate solution concentrations, respectively. The concentrations of salt solutions were calculated by a portable conductivity meter (Mi 306, Milwaukee, Romania). Na_2SO_4, $MgSO_4$, and NaCl were the salts used

in this study. Physical properties including the ionic radius and hydrated radius of various salts and the property of the dyes used in this study, are summarized in Table 5.2.

Table. 5.2: Specification of salts and dyes used in this study [183, 184].

Dyes	Molecular Structure	M_w (Da)*	λ(nm)**	Charge
MB	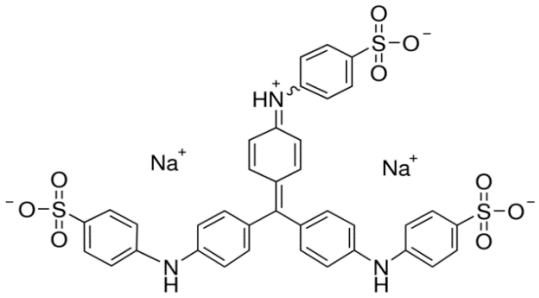	799.8	594	Anionic
MeB	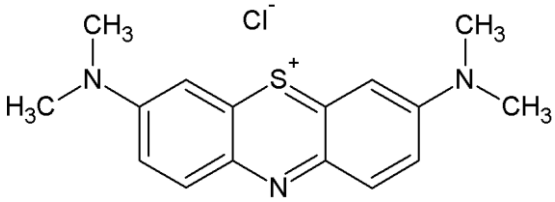	319.8	664	Cationic
RhB	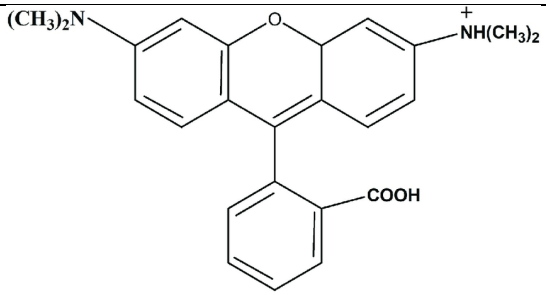	479.02	560	Cationic

* Molecular Weight
**Maximum absorption wavelength

Salts

Ion	Crystal ionic radius (Å)	Hydrated radius (Å)
Na^+	0.95	3.6
Mg^{2+}	0.65	4.3
Cl^-	1.8	3.3
SO_4^{2-}	2.9	3.8

The molecular weight cut-off (MWCO) of the prepared membranes was measured by the rejection of PEGs with various molecular weights (200, 400, 600, 800, 1000, and 1500 Da). Whenever rejection surpasses 90% for a given PEG, the molecular weight of that PEG is defined as the MWCO of the membrane. PEGs solution with concentration of 200 mg L^{-1} was used to probe the MWCO of the prepared membranes. The PEG concentration in the feed and permeate was calculated using DR 5000™ UV-Vis spectrophotometer (HACH Company, USA). The methods 10173 (15 to 150 mg/L C) and 10129 (0.3 to 20.0 mg/L C) were applied to measure the TOC of the feed and permeate. The MWCO values of every single membrane were calculated using the MWCO curve, which is a plot of the rejection of PEGs versus their molecular weight. In addition, the mean pore diameter of the prepared membranes was obtained utilizing the following equations [185, 186]:

$$dp = 33.46 \times 10^{-12} \times M^{0.557} \quad (3)$$

where M is the molecular weight of PEG (Da) and dp is the mean pore diameter (nm) of the prepared membranes. Dye concentrations in this study was obtained by a UV–vis spectrophotometer (Beckman Coulter DU 730). Methyl Blue (MB), Methylene Blue (MeB), and Rhodamine B (RhB) are used to study the dye rejection performance of the prepared membranes. At least three membrane samples were utilized for all separation performance measurements.

5.3. Results and Discussion

5.3.1. Characterization of nanomaterials

Fig. 5.2 shows the FT-IR spectra of MIL-101(Cr) and MIL-101(Cr) $–NH_2$ nanoparticles. The spectra of MIL-101(Cr) nanoparticles exhibited several strong IR absorption bands consistent with the reported spectrum [187]. The absence of vibration peak of carboxylic groups in FTIR spectrum at 1740 cm^{-1} showed the chelation between Cr^{3+} and –COOH that resulted in the formation of Cr–O bond [187, 188]. The rest of bonds between 590 and 1548 cm^{-1} are attributed to benzene rings,

consisting of the C=C stretching vibration at 1505 cm^{-1} and the C–H deformation vibration at 729, 972, and 1000 cm^{-1}[189]. The vibrational bands at 1420 cm^{-1} proved the existence of –O–(C=O)– (dicarboxylate groups) in the MIL-101(Cr) structure[187]. Besides, the sharp peaks at 1392 and 1548 cm^{-1} confirmed the presence of the stretching vibration of the carboxylates bond asymmetric vibrations on the terephthalic acid [187, 189]. The FT-IR image of MIL-101(Cr)-NH_2 exhibited that two peaks appeared at 3380 and 3600 cm^{-1} which, are attributed to N-H stretching of amide [190].

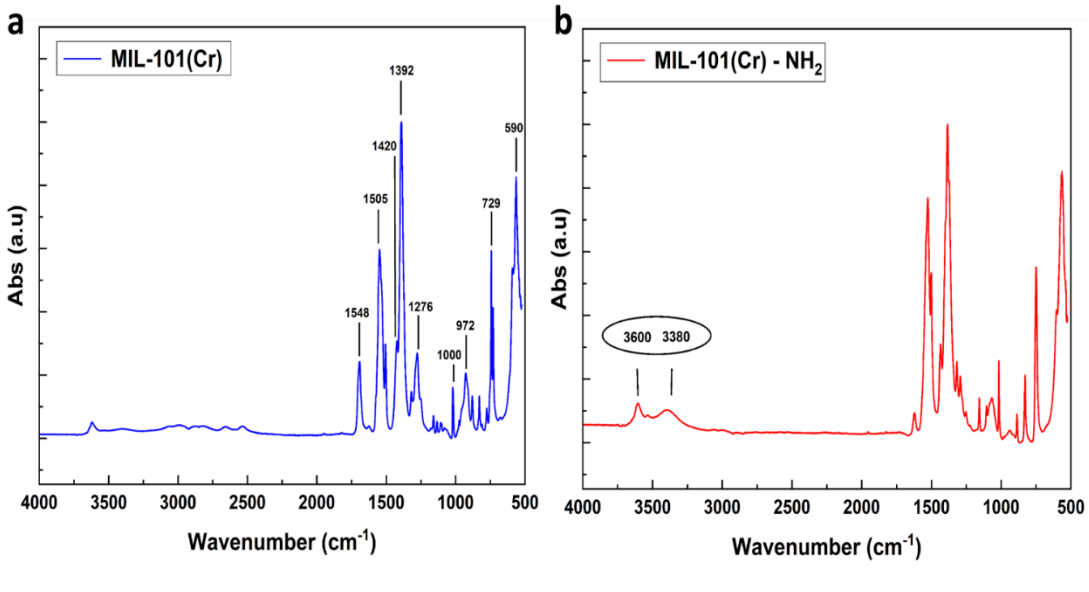

Fig. 5.2. FTIR spectra of (a) MIL-101(Cr) and (b) MIL-101(Cr)-NH_2 nanoparticles.

Fig. 5.3 (a-d) exhibited the morphology and structure of the fabricated MIL-101(Cr)-NH_2 nanoparticles. The SEM images Fig. 3 (a-b) of MIL-101(Cr)-NH_2 nanoparticles mainly consisted of prismatic crystals and hexagonal aggregated particles [191]. TEM images Fig.3 (c-d) also confirmed the hexagonal structure of MIL-101(Cr)-NH_2, and determined black small accumulated particles in TEM image (Fig. d) which can be attributed to NH_2, showing the deposition of NH_2 group on the surface of MIL-101(Cr) [189].

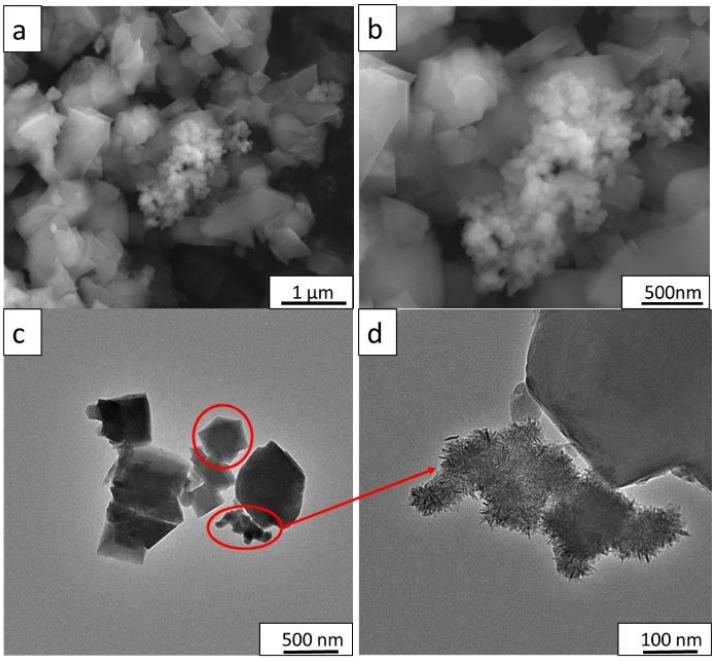

Fig. 5.3. SEM (a-b) and TEM (c-d) images of MIL-101(Cr)-NH_2.

5.3.2. Rheological properties of polymeric (casting) solutions

The rheological behavior of the polymeric solution studied utilizing steady-state rheological measurement that immensely influenced the phase inversion process, the morphology of the membranes, and their performance. The effect of MIL-101(Cr)-NH_2 nanoparticles on the viscosity of CA solution is exhibited in Fig. 5.4a, showing the viscosity of pure CA and CA/MIL-101(Cr)-NH_2 casting solutions vs. shear rate. All the membrane casting solutions (M0-M6) exhibited the Newtonian property in the investigated range of shear rate [32]. As shown in Fig. 5.4b, an enhancement in the viscosity of the casting solution was observed by adding MIL-101(Cr)-NH_2 nanoparticles. The highest value of the casting solution viscosity was reached at 149 Pa.s with the maximum incorporation of 1 wt% MIL-101(Cr)-NH_2 nanoparticles. The viscosity of the casting solution increased from 53 to 149 Pa·s by increasing of the MIL-101(Cr)-NH_2 nanoparticles from 0.0 to 1.0 wt%. The enhancement of the casting solution viscosity by adding MIL-101(Cr)-NH_2 (filler) shows the suitable interaction between MIL-101(Cr)-NH_2 and the polymer [32, 192]. This phenomenon can be attributed to polymer (CA)/solvent and polymer/filler interactions. By loading

fillers into casting solution, the dominant role of polymer decreased consequently since the fillers might behave as physical barriers to reduce the blend of polymer with solvent, resulting in the enhancement of casting solution viscosity [32, 193]. In other words, the enhancement in viscosity with loading MIL-101(Cr)-NH_2 can be related to more interaction of polymer (CA) and fillers (MIL-101(Cr)-NH_2) rather than polymers and solvents (DMF), therefore it causes the reduction of DMF molecules for polymer dissolution that make the polymer solution more viscous.

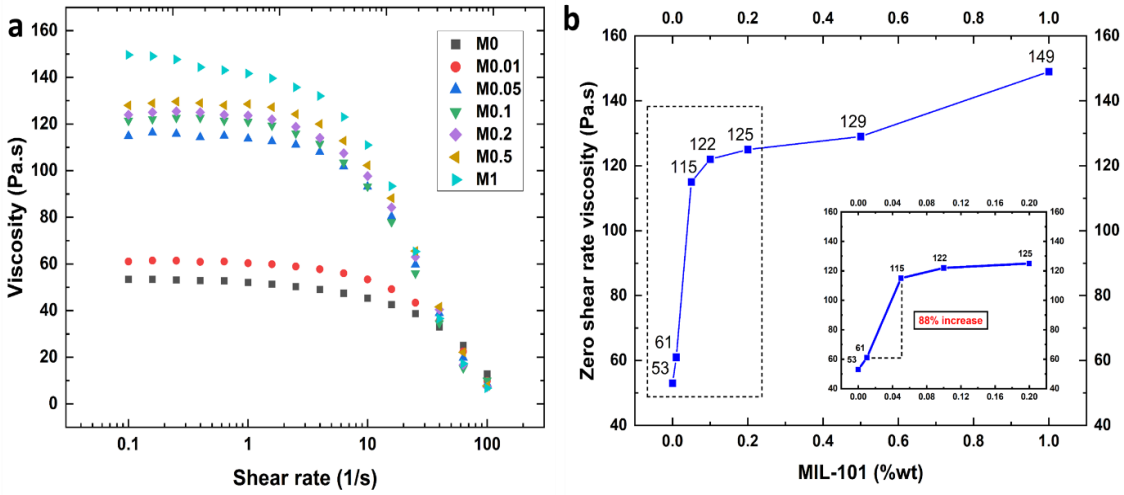

Fig. 5.4. The viscosity of casting solution vs. (a) shear rate and (b) various amount of MIL-101(Cr)-NH_2 loading.

5.3.3. Stability of CA/MIL- 101(Cr)-NH_2 in CA matrix

To study the stability of MIL-101(Cr)-NH_2 nanoparticles inside the CA matrix structure, M0 and M1 were immersed inside DI water at room temperature over 30 days. The precise value of the water contact angle (WCA) of the immersed samples was calculated to assess the tendency of MIL-101(Cr)-NH_2 nanoparticles to leach out from the CA membrane matrix. WCA values for M0 and M1 in terms of soaking time (days) are summarized in Table 3.

The values of WCA for M0 and M1 were remained almost constant, and WCA values were between 64.8 ± 0.4 and 66.4 ± 3.2 for M0. Similarly, the WCA values for M1 were constant, indicating negligible leaching out of MIL-101 (Cr)-NH_2 from the CA matrix into the liquid media.

Table 5.3: WCA values for M0 and M6 over 30 days.

Time (day)	M0 (WCAº)	M1 (WCAº)
Day 1	65.5 ± 1.4	50.5 ± 1.7
Day 4	63.9 ± 0.7	50.6 ± 0.4
Day 6	66.4 ± 3.2	50.9 ± 2.2
Day 10	64.8± 3.6	52.9 ± 1.2
Day 30	64.8 ± 0.4	52.3 ± 2.2

5.3.4. Characterizations of the prepared membranes

The top surface SEM images of the prepared membranes are exhibited in Fig. 5.5 As shown; recognition of the pores of the top surface is difficult even with 100,000X magnification, which indicates tiny pore sizes of the prepared membranes, which are difficult to see via any characterizations. The morphology of the membranes (M0-M1) was not substantially altered by loading various amount of CA/MIL-101(Cr)-NH_2 nanoparticles. As depicted in Fig. 5.5, the top surface of all the prepared membranes (M0-M1) are smooth and flat without any significant accumulative indication of CA/MIL-101(Cr)-NH_2 nanoparticles. Furthermore, the membrane surface was well developed without any sign of crack on the membranes surface.

Fig. 5.6 exhibits the cross-sectional SEM images of the pristine CA (M0) and modified membranes (M0.01-M1) membranes. The images showed that the membranes' unsymmetrical structure includes the top layer with a dense selective barrier and a bottom layer with macro void porous substructure.

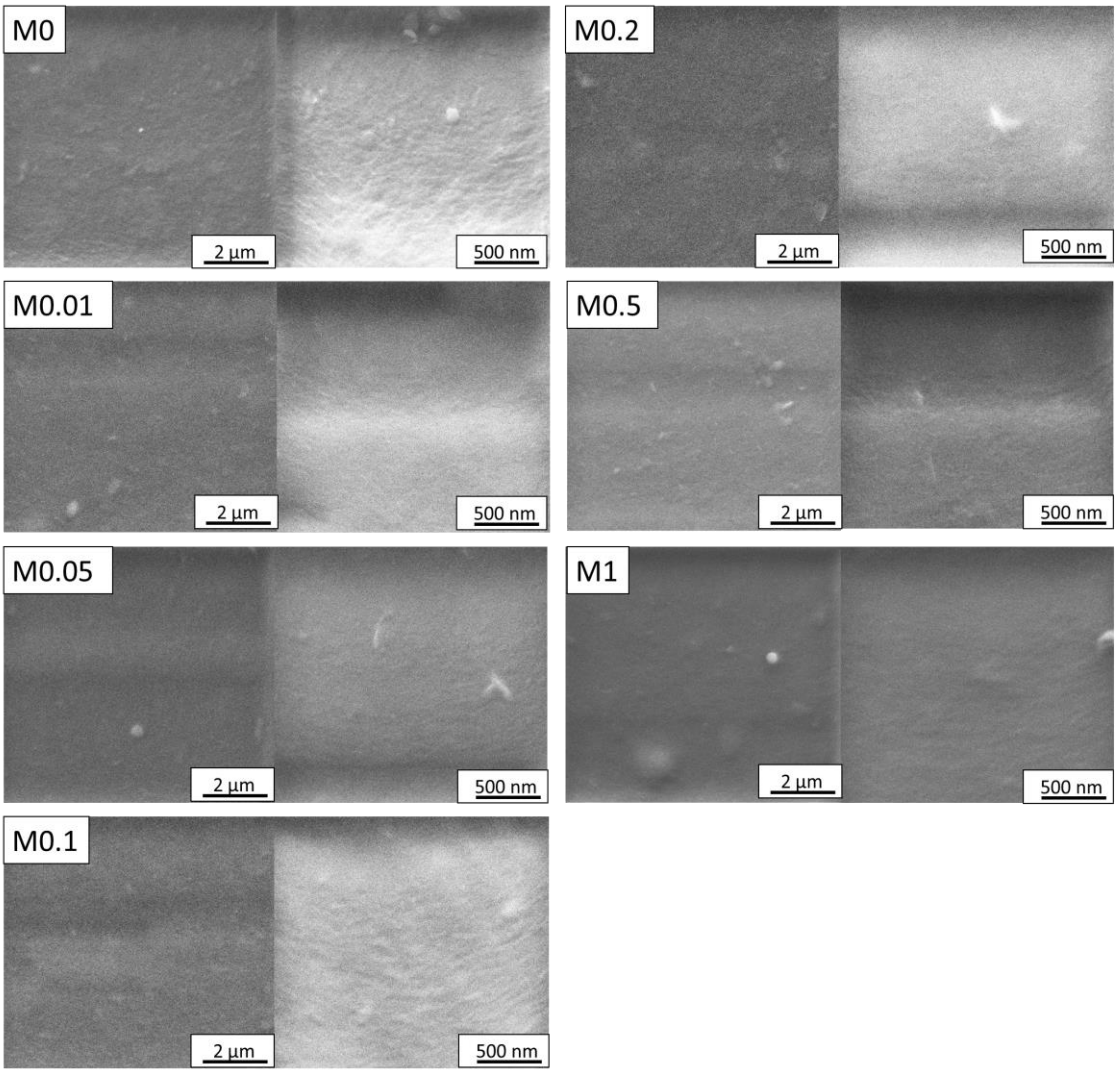

Fig. 5.5 SEM images of the top surface of the prepared membranes at various concentrations of MIL-101 (Cr)-NH_2.

Enhancing embedding MIL-101(Cr)-NH_2 nanoparticles up to 0.2 wt% (M0.01-M0.2) caused a reduction in the thickness of the upper layer and enhancement in the macro void porous structure of the bottom layer. The reason is by adding MIL-101(Cr)-NH_2 nanoparticles in the casting solutions immensely affects kinetic and thermodynamic of the phase inversion process by enhancing the mass transfer rate between DMF as the solvent and water as non-solvent phases. At the same time, the membranes coagulation affects the asymmetrical structure of the membranes by making larger pores [194]. Thus, MIL-101(Cr)-NH_2 nanoparticles act as a pore–making agent,

which possibly causes increased porosity of the membranes. In addition, because of the water affinity property of MIL-101(Cr)-NH_2 nanoparticles, water diffusion increased during the phase inversion which caused quicker phase separation and it reduced the thermodynamic stability of the solution [195]. This process increased pores of the prepared membranes by making progress in the diffusion rate of MIL-101(Cr)-NH_2 nanoparticles in the casting solution. However, enhancing MIL-101(Cr)-NH_2 incorporation in the casting solutions from 0.2 to 1 wt% enhanced the viscosity of the casting solution, which resulted in a lower exchange rate between the solvent and non-solvent phases. In this case, the rate of the membrane coagulation reduced, that caused denser structure and lower porosity of the prepared membranes (M0.2-M1) [196]. Thus, adding more nanoparticles into the casting solution created the accumulation of nanoparticles, which resulted in defective pore formation.

AFM images of the prepared pristine CA and CA/MIL-101(Cr)-NH_2 NF membranes are exhibited in Fig. 5.7 and the surface roughness parameters are summarized in Table 5.4. In given images, the red spots represent the highest points of the membrane surface, while the blue regions show valleys or pores of the membranes. AFM images indicate that the surface roughness of modified membranes is less than the pristine CA membrane (M0). By incorporating the filler up to 0.5%, the average roughness decreased from 41.3 nm for M0 to 5.5 nm for M0.5. However, by increasing the filler from 0.5% to 1%, the average roughness increased from 5.5 nm to 8.3, which can be attributed to MIL-101(Cr)-NH_2 agglomeration. Enhancing embedding MIL-101(Cr)-NH_2 nanoparticles up to 0.2 wt% (M0.01-M0.2) caused a reduction in the thickness of the upper layer and enhancement in the macro void porous structure of the bottom layer. The reason is by adding MIL-101(Cr)-NH_2 nanoparticles in the casting solutions immensely affects kinetic and thermodynamic of the phase inversion process by enhancing the mass transfer rate between DMF as the solvent and water as non-solvent phases. At the same time, the membranes coagulation affects the asymmetrical structure of the membranes by making larger pores.

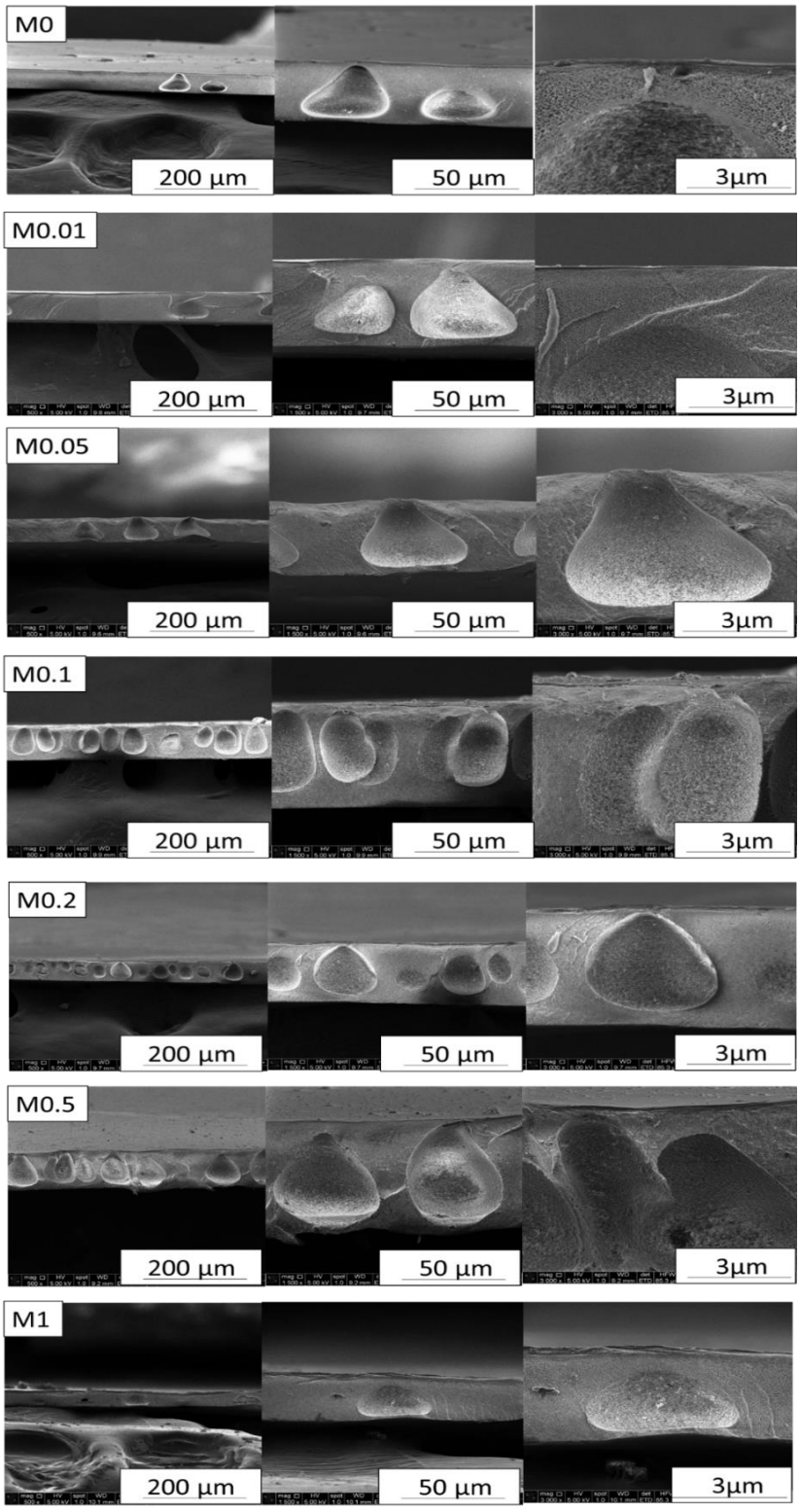

Fig. 5.6 Cross-sectional SEM images of the prepared membranes.

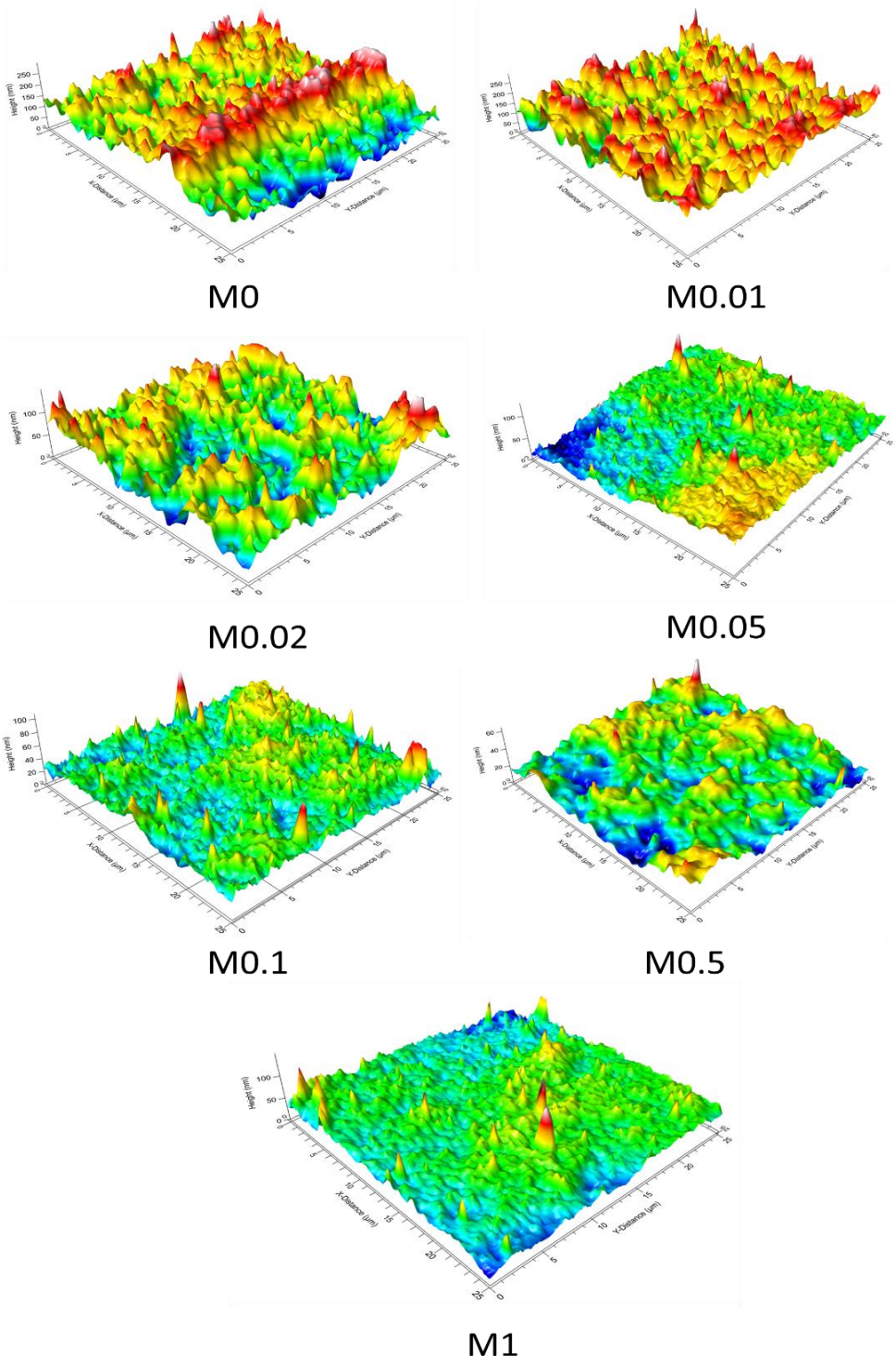

Fig.5.7 AFM images of the prepared membranes.

Table 5.4: Surface roughness parameters of the membranes.

Membrane name	Roughness Parameters		
	S_a (nm)	Sq (nm)	S_t (nm)
M0	41.3	51.2	154
M0.01	32	31.9	138.1
M0.05	16.9	21.1	92.04
M0.1	11	14.6	81.7
M0.2	7.4	9.5	72.3
M0.5	5.5	6.7	43.9
M1	8.3	11.01	101.3

Fig. 5.8 shows EDX mapping and Cr percentage of M0, M0.05, M0.2, and M1. The MIL-101(Cr)-NH_2 nanoparticles scattered in the CA matrix are exhibited with orange points, confirming the attendance of the chromium element. As shown in Fig. 5.8, at low MIL-101(Cr)-NH_2 nanoparticles concentrations, the EDX mapping of the Cr element exhibited the uniform scattering of MIL-101(Cr)-NH_2 nanoparticles in the CA membrane matrix. The nanoparticles were agglomerated by increasing the nanoparticles loading, particularly in M1. As shown in Fig. 5.8b, the amount of Cr as major element of MIL-101(Cr)-NH_2 nanoparticles increased from 0 form M0 to 0.26% for M1. This excessive deposition of MIL-101(Cr)-NH_2 nanoparticles and agglomeration at the top surface of the membrane might block the pores. The membrane pore blockage has an immense effect on the flux and separation performance of the prepared membranes.

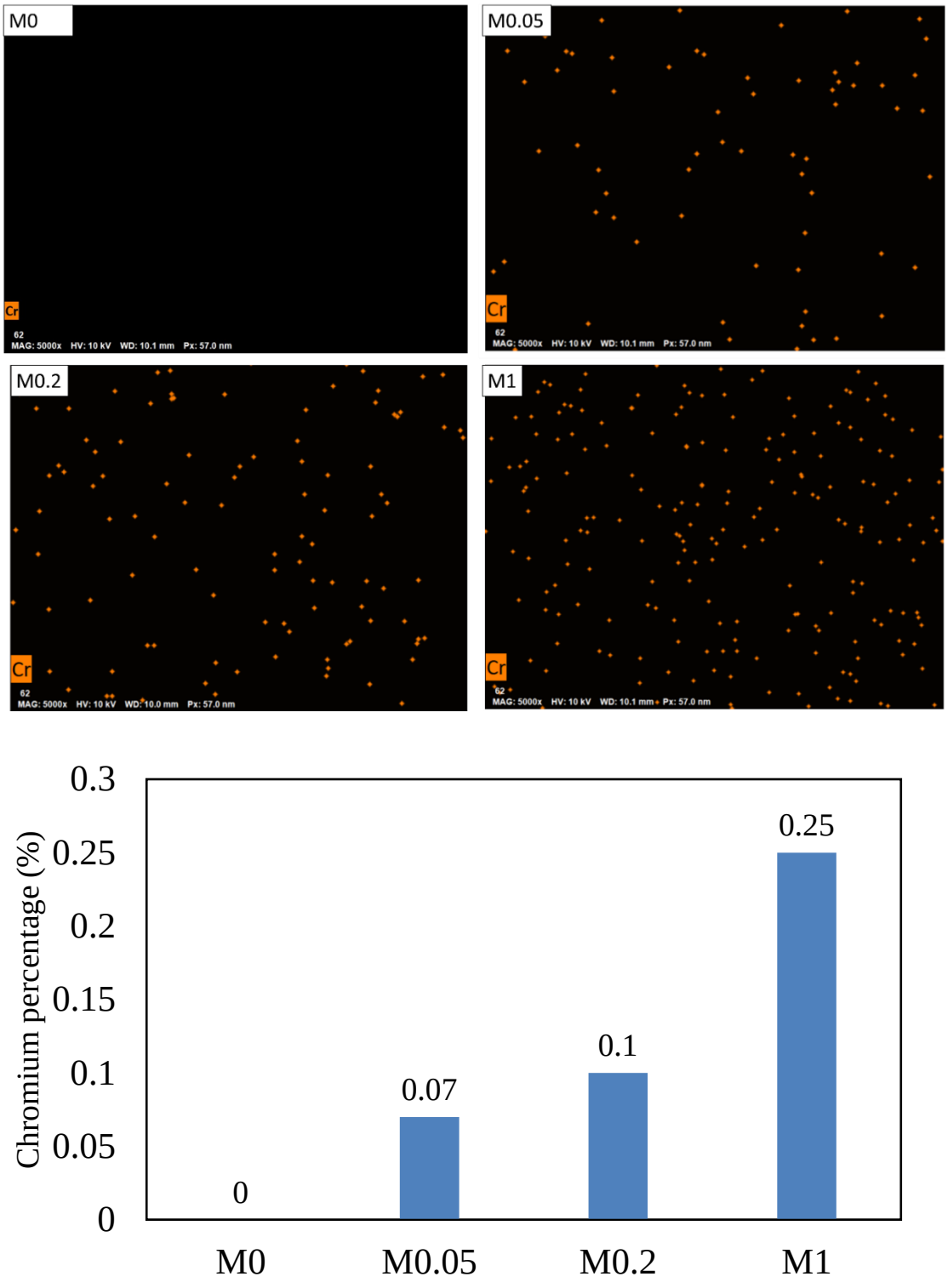

Fig. 5.8. EDX mapping and Cr percentage of M0, M0.05, M0.2, and M1.

One of the most significant indices for evaluating the performance of membranes in terms of permeability is surface hydrophilicity. In order to study the impact of MIL-101-(Cr)-NH_2 incorporation on the hydrophilicity of the prepared membranes, water contact angle (WCA) was calculated. A lower WCA indicates higher hydrophilicity and, consequently, higher water affinity to the surface of the membrane. In other words, lower WCA shows that membranes have higher water flux and fouling-resistant properties, particularly in UF/NF membranes [32]. As shown in Fig. 5.9a-b, drop of water on the surface of M1 spread out more than M0, indicating higher hydrophilicity of M1 membrane. The Plot of dynamic WCA exhibited that by adding MIL-101-(Cr)-NH_2 into the CA membrane matrix, WCA decreased from 65.1 ± 0.5 for M0 to 50.3 ± 1.9 for M1. It should be mentioned that hydrophilic functional groups such as NH_2 in MIL-101-(Cr) structure and its hydrophilic property of MIL-101-(Cr) are two main reasons for improving the hydrophilicity property of the modified membranes. Thus, by increasing the weight percentage of MIL-101-(Cr)-NH_2 nanoparticles in the membrane structure, the water affinity of the modified membranes increased consequently.

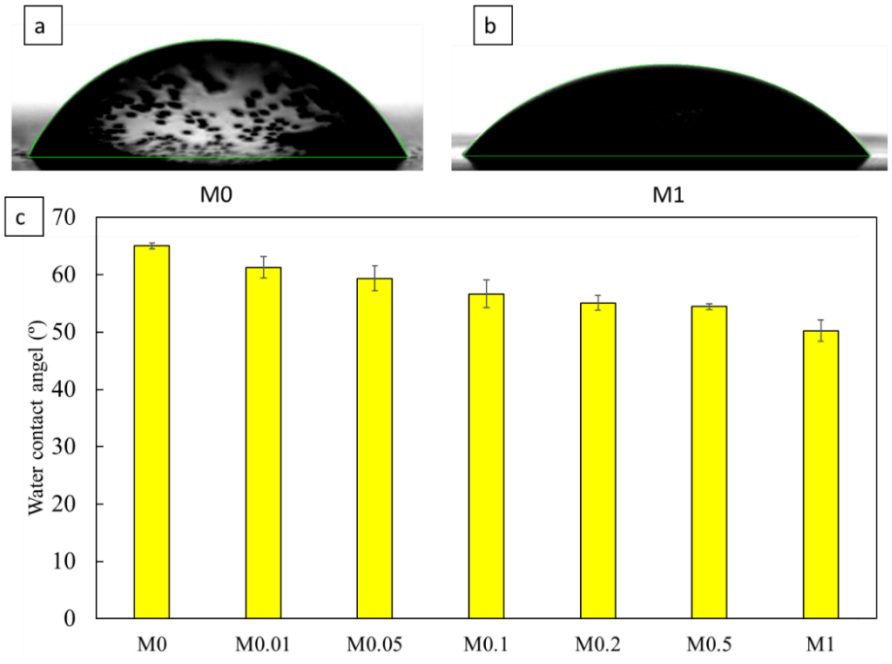

Fig. 5.9. Dynamic WCA of M0 (a), M1(b), and the WCA values of the prepared membranes (c).

Surface charge is one of the most significant parameter that immensely affects the separation efficiency, particularly for the salts rejection. As shown in Fig. 10, all the prepared membranes showed negative zeta potential from -27.6 ± 0.3 to -10.8 ± 0.11 mV for the pH of 6. It is obviously the negative surface charge of CA membrane (M0) is because of the CH_3^- and OH^- of CA polymer [197]. The incorporated membranes showed less negative surface charge compared with the pristine CA because of the positively surface charge of MIL-101(Cr)-NH_2 nanoparticles. In fact, trimeric Cr octahedral clusters and terephthalate ligands make the MIL-101(Cr)-NH_2 positively surface charged [198, 199]. By incorporating MIL-101(Cr)-NH_2 nanoparticles up to 0.5 wt%, the zeta potential increased from -27.6 ± 0.25 mV for M0 to -19 ± 0.35 mV for M0.5. However, by adding more MIL-101(Cr)-NH_2 nanoparticles from 0.5 to 1 wt%, the zeta potential increased from to -19 ± 0.35 mV for M0.5 to -10.4 ± 0.36 for M1 which can be attributed to the agglomeration of MIL-101(Cr)-NH_2 nanopartilces [194, 200]. Furthermore, by adding the nanoparticles the surface charge became more negatively because the nanoparticles moved toward the top layer of the membranes [200].

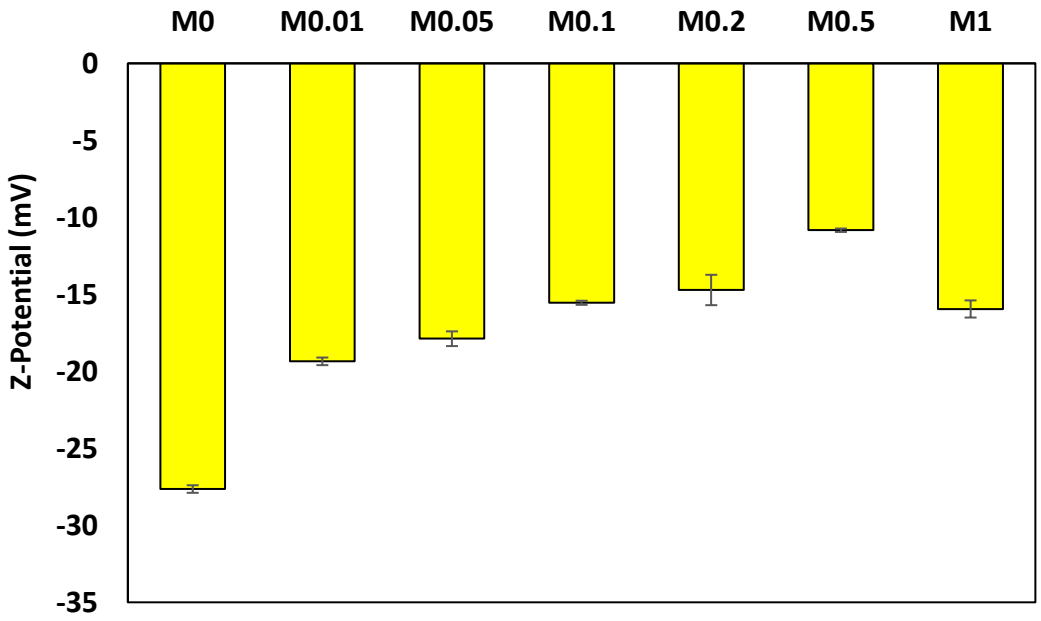

Fig. 5.10. Zeta potential results of the prepared membranes at pH value of 6.

To study the Impact of embedding of MIL-101-(Cr)-NH_2 nanoparticles on the structure and performance of the prepared membranes, MWCO (Da) and mean pore diameter (nm) were calculated by utilizing Eq. 3. The MWCO results for the prepared CA/MIL-101-(Cr)-NH_2 NF membranes and the mean pore diameter (nm) are shown in Fig. 5.11 and summarized in Table 5.5, respectively.

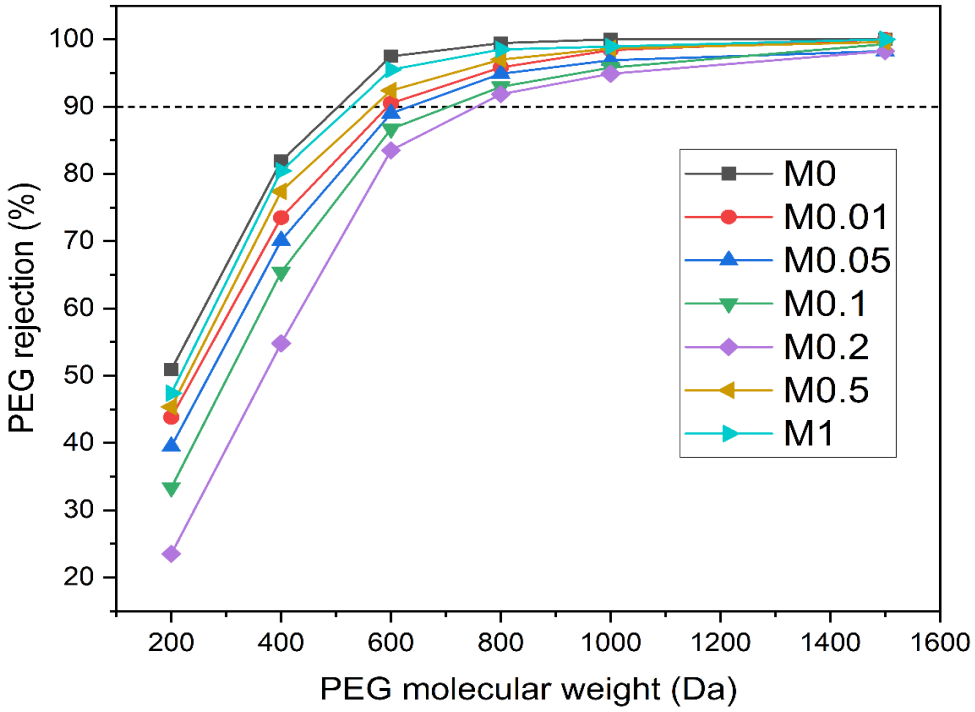

Fig. 5.11. PEG rejection of the prepared membranes (PEG concentration = 200ppm).

According to the obtained results, the mean pore diameter of the modified membranes (M0.01-M1) is larger than the pristine CA (M0). Enhancing MIL-101(Cr)-NH_2 nanoparticles into the CA matrix from 0 to 0.2 wt% caused an enhancement of the mean pore diameter and MWCO from 1.07 nm (504 Da) to 1.34 nm (756 Da), respectively. This phenomenon might be attributed to the movement of MIL-101(Cr)-NH_2 nanoparticles toward the top layer of the prepared membranes during the phase inversion process, which causes a prompt exchange between the solvent and non-solvent. The prompt exchange increased the porosity and the mean pore diameter of the prepared membranes [32, 186]. Nevertheless, by incorporating more MIL-101(Cr)-NH_2 nanoparticles in the

CA matrix membrane from 0.2 to 1 wt%, a reduction observed in the mean pore diameter that could be explained based on the accumulation of MIL-101-(Cr)-NH_2 nanoparticles and enhancing the viscosity of the casting solution. These two phenomena reduced the exchange rate between solvent and non-solvent phases, which caused a reduction in overall porosity and mean pore diameter of the prepared membranes.

Table 5.5: MWCO and mean pore diameter of the prepared membranes.

Membranes	Molecular cut off (Da)	Mean pore diameter (nm)
M0	504	1.07
M0.01	594	1.17
M0.05	634	1.22
M0.1	706	1.29
M0.2	756	1.34
M0.5	568	1.15
M1	527	1.10

5.3.5. Permeation performance of the prepared membranes

5.3.5.1. Effect of pressure on pure water flux

In addition to membrane properties, the membrane driving force, such as applied pressure has a significant impact on membrane performance, such as pure water flux and separation efficiency. Fig. 5.12 exhibits the impact of applied pressure (0.2, 0.4, and 0.6 MPa) on the prepared membranes' PWF. Obviously, PWF of all the prepared membranes was enhanced by increasing the

applied pressure from 0.2 to 0.6 MPa. However, the amount of this enhancement was different for the prepared membranes. Although M0.2 showed the highest PWF at pressure 0.2 and 0.4 MPa, M1 showed the highest amount of PWF at pressure 0.6 MPa. For instance, at the pressure of 0.4 MPa, the highest and the lowest PWF were related to M0.2 (53.97 ± 2.3 LMH) and M0 (23.2 ± 1.7 LMH) membranes, respectively. For applied pressure (0.2, 0.4, and 0.6MPa), M0 showed the lowest PWF that can be attributed to its water contact angle and smaller pore size compared with other prepared membranes. Generally, the membrane flux is significantly impacted by hydrophilicity and the pore structure of membranes [201]. On similar lines, it was observed that PWF was considerably enhanced by increasing the amount of MIL-101(Cr)-NH_2 from 0.0 to 1 wt%, which can be attributed to increasing hydrophilicity of the prepared membranes. In fact, the higher hydrophilicity of the prepared membranes can increase water permeability by improving the water affinity of the membranes. Furthermore, increasing the amount of MIL-101(Cr)-NH_2 in the membrane matrix remarkably enhanced the porosity of the membranes, which caused higher PWF [202]. However, with a further enhancement of MIL-101(Cr)-NH_2 content from 0.2 to 1 wt%, PWF was reduced at pressure of 0.2 and 0.4 MPa from 34.9 ± 0.87 to 27.36 ± LMH, and from 53.97 ± 2.2 to 48.1 ± 1.5 LMH, respectively. This reduction might be attributed to the agglomeration of the incorporated nanoparticles which resulted in non-uniform dispersion and pore blockage of the prepared membranes. Unlike 0.2 and 0.4 MPa, PWF of the prepared membranes at pressure of 0.6 increased continuously from 26.98 ± 1.8 LMH for M0 to 68.1 ± 0.87 LMH for M1 that can be attributed to hydrophilicity dominant compared with pore size at pressure of 0.6 MPa.

5.3.5.2. Study the performance of membranes for salts rejection

Na_2SO_4, $MgSO_4$, and NaCl were considered to study the performance of prepared membranes at the operational condition of 500 ppm salt concentration, pressure of 0.4 MPa, and temperature of 24 ± 0.5. For the prepared membranes, salt rejections reduced in the order of Na_2SO_4> $MgSO_4$ >

NaCl (Fig. 5.13) that can be explained based on the electrostatic interaction and size exclusion (pore size).

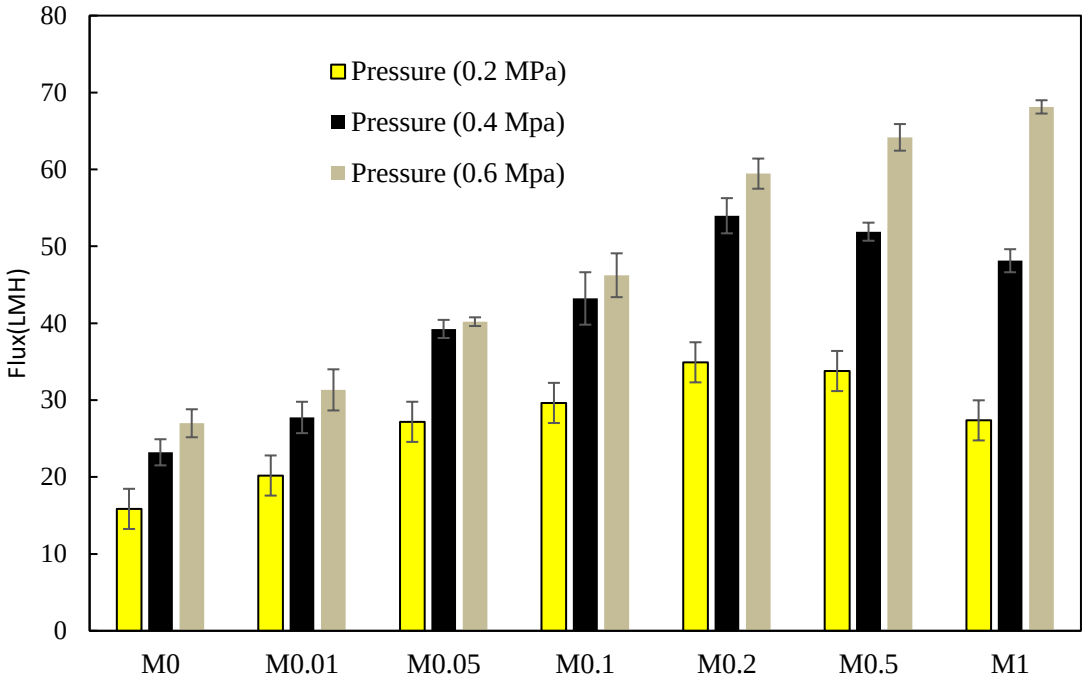

Fig. 5.12 Effect of pressure on Pure water flux of the prepared membranes.

As shown in Fig. 5.13, the highest and lowest NaCl rejection were 14.4 ± 1.4 and 8 ± 0.5 for M0 and M0.2, respectively. However, the highest and lowest rejection of Na_2SO_4 was 65.1 ± 2.5 and 51 ± 8 for M0 and M0.5, respectively; while the corresponding values for $MgSO_4$ were 59.3 ± 2.3 and 46.1 ± 0.8 for M0 and M0.5, respectively. According to the order, the size exclusion might explain the higher rejection rates of Na_2SO_4 and $MgSO_4$ compared to NaCl. For the salt summarized in Table 5.2, the order is $SO_4^{2-} > Cl^- > Na^+ > Mg^{2+}$, and it can be explained based on a universal rule for the size of ions with a negative and positive charge. The ions with negative charges are much bigger than ions with positive charges. In fact, the more positive and negative charge of ions, the smaller and bigger ions, respectively (Table 5.2) [183]. Like for instance, according to the sieving effect, the hydrated radius of SO_4^{2-} (3.8 Å), and Na^+ (0.95 Å) are bigger than Cl^- (3.3 Å) and Mg^{2+} (0.65 Å), respectively.

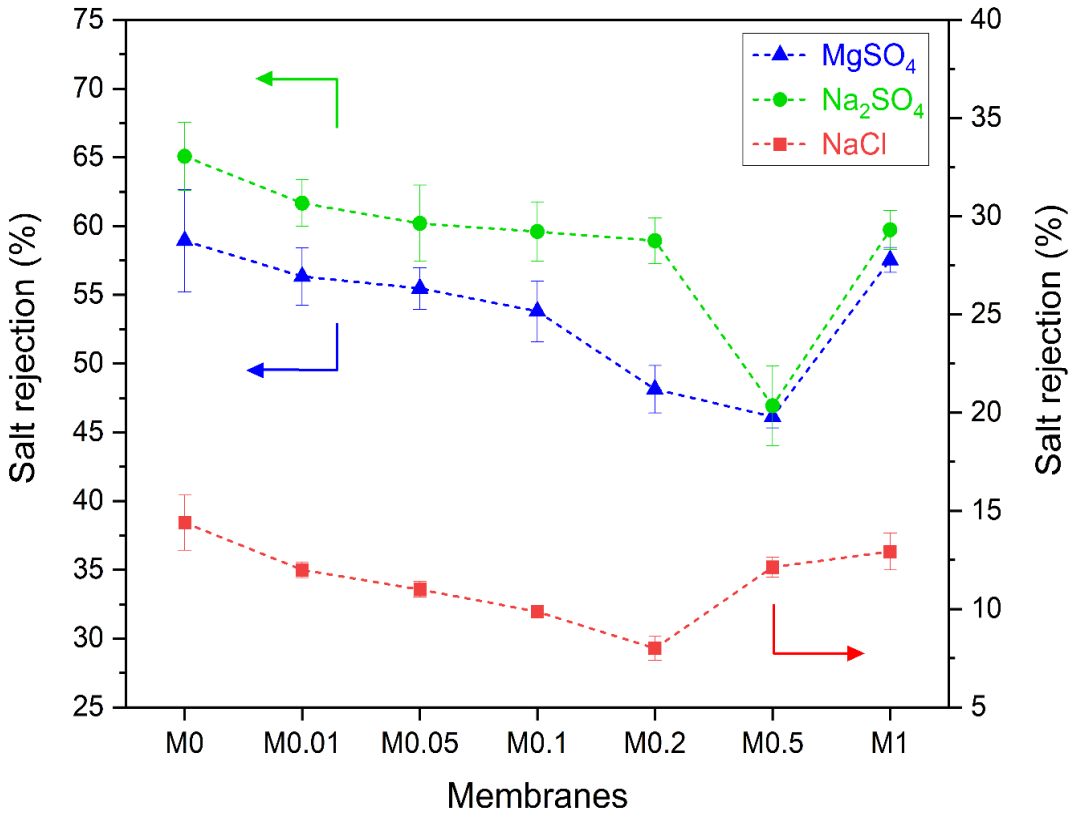

Fig. 5.13. Salt rejection of the prepared membranes for different kinds of salt solutions of NaCl, Na_2SO_4, and $MgSO_4$.

This could be a solid explanation for the higher rejection of sodium sulfate than magnesium sulfate. In addition, salt rejection for the prepared membranes depends not only on size exclusion (pore size) but also on electrostatic interaction between the surface of the membranes and the ions existing in the solution. Generally, this phenomenon can be clarified by the Donnan exclusion effect. The Donnan effect is the failure distribution of charged particles evenly across the two sides of the membrane close a semi-permeable membrane that sometimes fail to distribute evenly across the two sides of the membrane [203]. The usual cause is the presence of a different charged substance that is unable to pass through the membrane and thus creates an uneven electrical charge [204]. As shown in Fig. 5.10, the results of zeta potential confirmed that all the prepared membranes are negatively surface charged, while after incorporating MIL-101(Cr)-NH_2 as fillers, the surface

of the prepared membranes became less negatively surface charged. M0 showed higher Na_2SO_4 and $MgSO_4$ rejection because of the higher negative surface charge that led to the existence of stronger electrostatic repulsion. In fact, the anion SO_4^{2-} was rejected due to the stronger electrostatic repulsion with the M0 membrane having higher negative charge compared with other membranes. Furthermore, based on the Donnan Exclusion mechanism (the electrostatic repulsive interaction), the anion valence electrons dominantly control the amount of salt rejection in the negatively charged prepared membrane. For example, divalent anions (SO_4^{2-}) are heavily rejected by the prepared membrane, however, monovalent anions (Cl^-) are repulsed lower. Therefore, the salt containing sulfate can be removed more than salts containing chloride. Therefore, the order of the rejection rate of salts used in this study is perfectly attributed to the anion valence reduction order or weaker anion repulsion forces [205]. Finally, the order of desalination can be explained according to the cation charge density enhancement.

The amount of electric charge per volume is defined as the cation charge density (ρ) as follows:

$$\rho = \frac{q}{\frac{4}{3}\pi r^3} \quad (4)$$

where q is the cation charge, and r is the ionic radius (Å) [206]. Based on equation 4, the more charge density of a cation acquires, the stronger electronic affinity. Therefore, the electrostatic attraction of negatively charged membranes on the Mg^{2+} is more than Na+ (1.66 Vs. 0.26), which caused lower rejection of Mg^{2+} than Na^+.

5.3.5.3. Study the performance of membranes for dye rejection

Methyl Blue (MB), Methylene Blue (MeB), Rhodamine B (RhB) are applied to study the performance of the prepared membranes for dye rejection. The molecular weight of MeB (319.8 Da) is lower than the MWCO of the prepared membranes (504-756 Da), meaning that the MeB enters the pore and channels of the prepared membranes and then passes through the membrane easily. Therefore, the prepared membranes did not show any rejection for MeB. However, the

prepared membranes rejected MB and RhB. The molecular weight of MB (799 Da) is larger than the MWCO of all the prepared membranes (504-756 Da). Therefore, the rejection of MB is immensely caused by size exclusion, and confirms that the pore diameter of the prepared membranes are generally smaller than the effective hydrodynamic size of the dyes. As shown in Fig. 5.14, all the prepared membranes showed a rejection rate for MB higher than 97%. The prepared membranes showed less rejection for RhB because the MWCO of all the prepared membranes (504-756 Da) is higher than the molecular weights of RhB (479.02 Da). For negatively surface charged membrane, cationic RhB dye is adsorbed on the membrane surface. Therefore, the Donnan exclusion as a result of the strong negative charge of the M0 membrane could effectively improve the rejection rate of the positively charged RhB because M0 showed highest tendency to adsorb the positive charge RhB than M1 that is less negatively charged according to the membrane surface zeta potential results (Fig. 5.15).

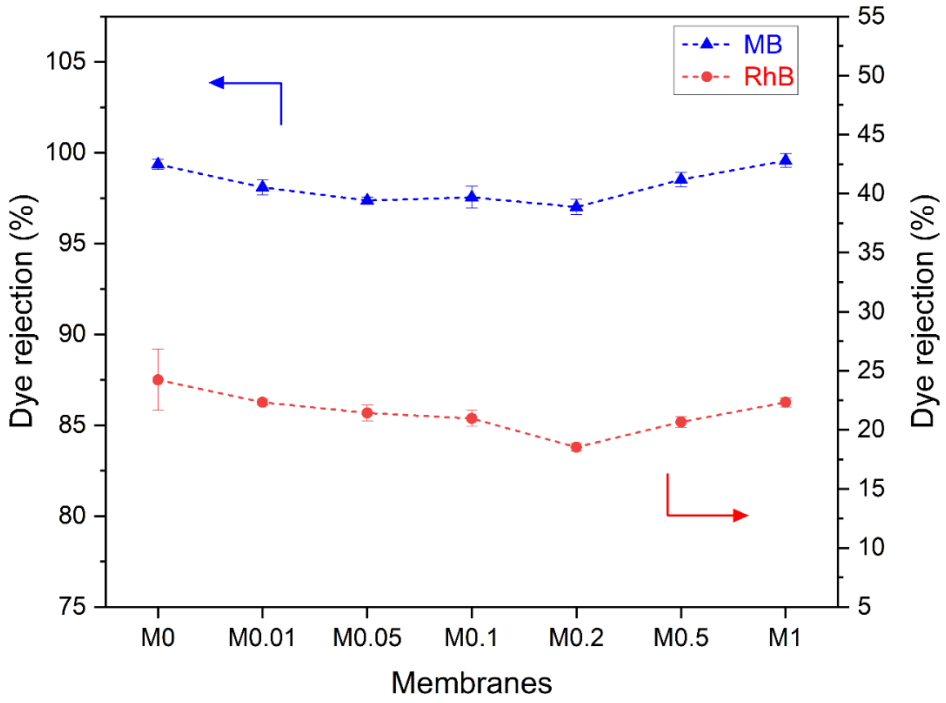

Fig. 5.14. Dyes rejection of the prepared membranes for Mb and RhB dye solutions (dyes concentration = 100 ppm, pressure=0.4 MPa, and at room temperature).

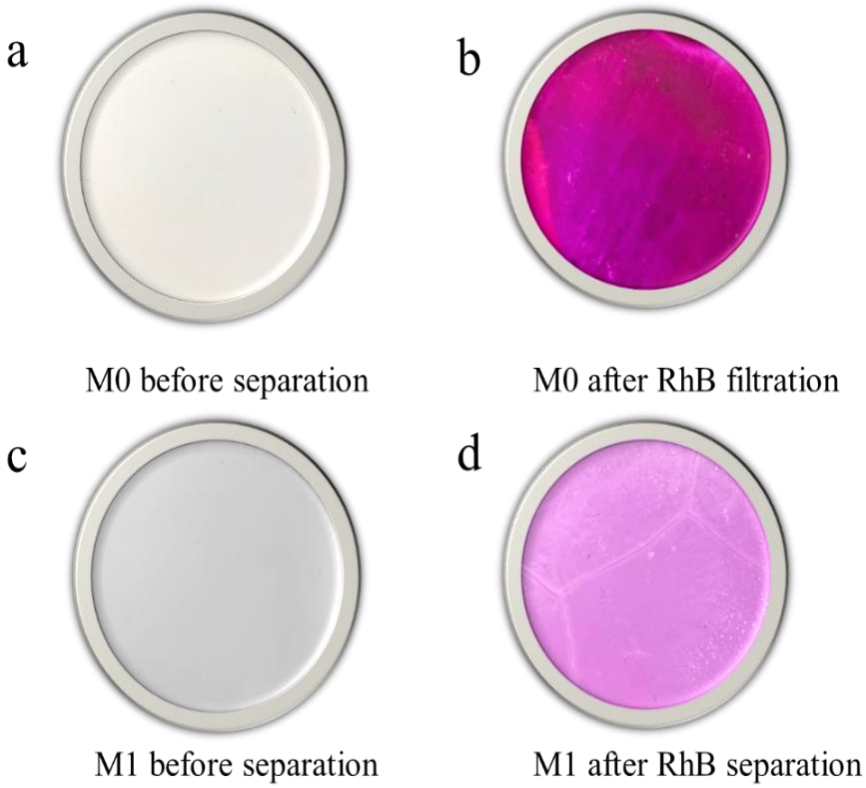

Fig. 5.15 Image of M0 and M1 membranes before and after dye/salt rejection.

5.3.5.4. Study the performance of membranes for dye/salt rejection

Existing salts in the dying process or byproduct from the synthesis of dye might affect dye rejection and permeate flux during the filtration of the dye/salt solution. To investigate the effect of salt on dye rejection and vice versa, M0 and M0.2 were applied for various concentrations of MB/Na_2SO_4 and RhB/Na_2SO_4. Fig. 5.16 exhibited the filtration of MB/Na_2SO_4 for M0 and M0.2, respectively. By increasing the salt concentration from 100 ppm to 2000 ppm, Na_2SO_4 rejection for M0 and M0.2 decreased from 83.2 ± 2.95 to 44.5 ± 3.3 and from 76.6 ± 3.5 to 39.3 ± 0.5, respectively (Fig.5.16a-b). This reduction might be due to the Debye length of the electrostatic interaction between the charged ions and the membrane is extended as the salt concentration increases. In fact, by increasing salt concentration from 100 ppm to 2000 ppm, the impact of the cation shield is

immensely stronger on the negatively surface charged prepared membranes. This phenomenon caused the reduction of the prepared membranes' repulsion on the anions, leading to the reduction of the salt rejection. In addition, as shown in Fig. 5.16a-b, by twentyfold enhancement of MB concentration from 50 ppm to 1000 ppm, the dye rejection remained almost same for M0 (99.7%) and M0.2 (97.9%). As explained earlier, MB is an anionic dye with bigger molecule size than MWCO than M0 and M0.2 meaning the rejection of MB is mostly caused by size exclusion (Fig. 5.16a-b). M0 and M0.2 showed higher Na_2SO_4 rejection in the RhB/Na_2SO_4 solution than MB/Na_2SO_4 solution. For the MB/Na_2SO_4 solution, Na_2SO_4 rejection at the concentration of 100 and 2000 were 83.2 ± 2.95 and 44.5 ± 3.3 for M0, respectively, while the corresponding values were 76.6 ± 3.5 and 39.3 ± 0.5 for M0.2 (Fig. 5.16c-d). However, in the RhB/Na_2SO_4 solution Na_2SO_4 rejection at the concentration of 100 and 2000 increased to 86.2 ± 3.8 and 50.5 ± 0.84 for M0 and 82.03 ± 1.3 and 44.5 ± 0.65 for M0.2, respectively (Fig. 5.16c-d). The Na_2SO_4 rejection enhancement in the RhB/Na_2SO_4 solution can be attributed to cationic property of RhB dye. By increasing RhB concentration, the adsorption and accumulation of positively charged RhB dye increased on the surface of negatively charged membranes leading to a reduction of the prepared membranes' pore size. In other words, enhancement of RhB adsorption on the membrane surface improved the effect of steric exclusion leading to Na_2SO_4 rejection enhancement in the RhB/Na_2SO_4 solution compared with the MB/Na_2SO_4 solution. Furthermore, by increasing dye concentration from 50 ppm to 1000 ppm, dye rejection decreased for M0 and M0.2 that can be attributed to the Donna effect. As mentioned earlier, M0 and M0.2 membranes showed less rejection for RhB because their MWCO is lower than the molecular weights of RhB (479.02 Da). Thus, since the RhB rejection is mainly dominated by the Donnan effect, by increasing the dye concentration, its rejection rate decreased consequently.

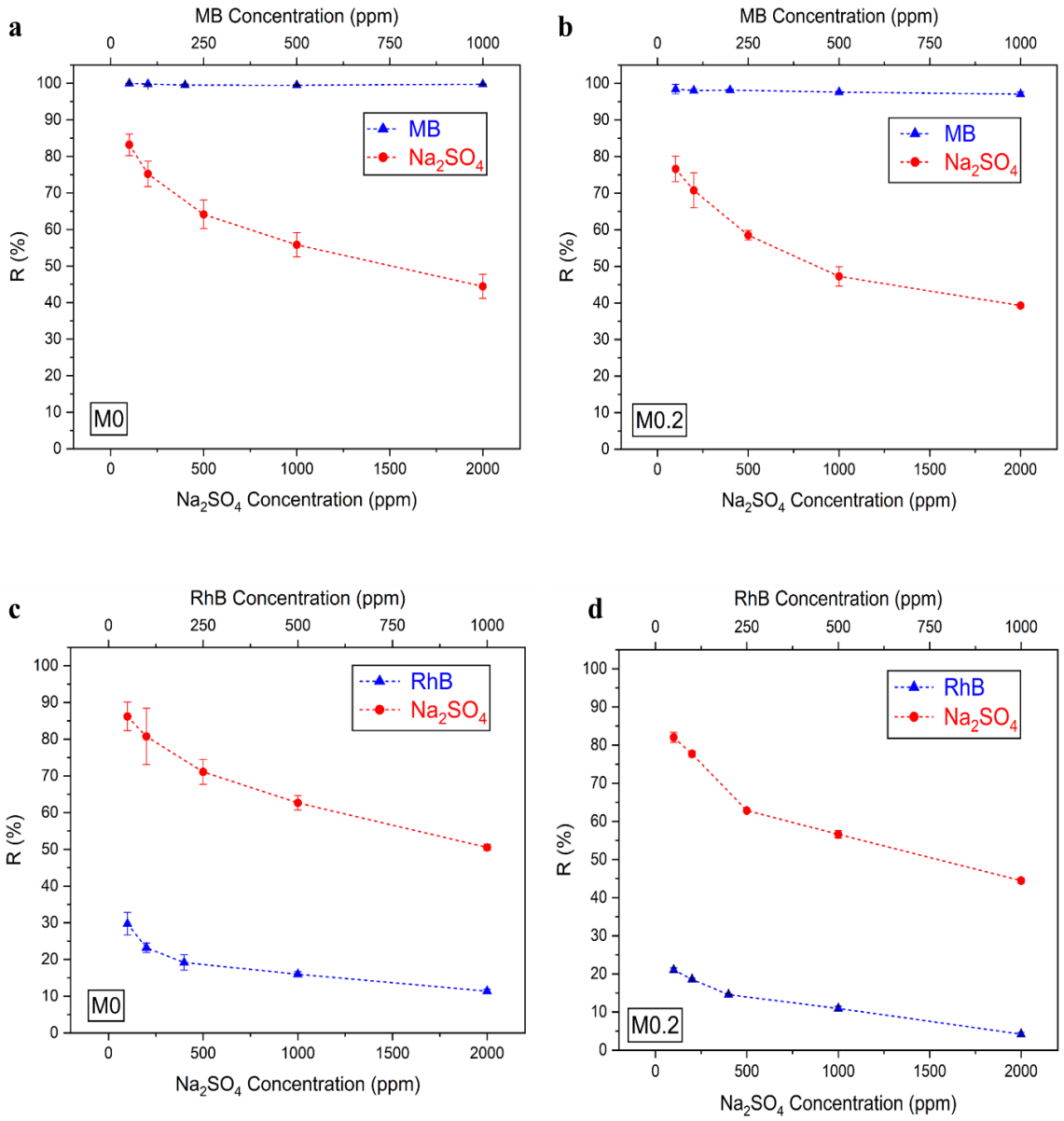

Fig. 5.16. Performance of M0 and M0.2 for dye/salt solution treatment.

5.3.5.5. Study antifouling property of the prepared membranes

Fouling is a major issue in membrane technology leading to the reduction in flux and lifetime of the membranes. The hydrophilicity, pore size, and roughness of the membrane surface play a significant role in the fouling behavior of the membranes. Super hydrophilic membranes with larger pore size and lower surface roughness might result in better fouling-resistance membranes [200]. In order to study the antifouling properties of the prepared membranes, a Bovine serum albumin (BSA) solution was utilized for filtration in this study. First, the membranes were tested for pure

water for 120 minutes. Then, the feed solution was switched from pure water to BSA solution, and the water flux for the prepared membranes was obtained (Fig. 5.17a). As shown in Fig. 5.17a, the water flux for the BSA solution for all the prepared membranes suddenly reduced and stayed almost stable over 120 min of BSA filtration. The reduction might be attributed to BSA agglomeration, and deposition on the membrane surface resulted in blocking some membrane pores since BSA protein has a high tendency to stick on the membrane surface [207]. After that, the fouled membranes were taken out, washed with DI water for 10 min, and then immersed in DI water for 20 min. Finally, the washed membranes were tested to calculate pure water flux after switching back the feed solution from BSA to DI water for the third 120 min. As exhibited in Fig. 5.17a, M0 and M0.2 showed the highest and lowest pure water flux before and after BSA flux, respectively, contributing to better fouling-resistant property of M0.2. Additionally, M0.2 showed higher BSA flux because of its higher hydrophilicity. As explained before, by incorporating MIL-101 (Cr)-NH_2 nanoparticles, the hydrophilicity of the membranes increased. During the phase inversion process, the nanoparticles moved toward the top surface of the membranes. The hydrophilic nanoparticles on the top surface of membranes make a strong interaction with a water molecule, which creates a very thin layer of water on the top surface of the membranes. In this case, the thin film plays a significant role in improving the membranes' antifouling property and drastically decreasing the BSA protein deposition on the membrane surface. To better understand the antifouling property of the prepared membranes, FRR was calculated. As exhibited in Fig. 5.17b, FRR increased from 54.3% ± 2.4 for M0 to 82% ± 2.5 for M0.2, which might be explained based on higher hydrophilic property of M0.2. However, FRR decreased slightly from 82% ± 2.5 for M0.2 to 77.2% ± 4.7 which is attributed to agglomeration of nanoparticles on the membrane surface. The surface roughness is another parameter that significantly impacts the fouling behavior. As shown in Table 5.4, by adding MIL-101 (Cr)-NH_2 into the CA membrane matrix, the roughness decreased, which helped in improving the antifouling property of membranes since there are fewer channels for the containments on membranes surface to deposit.

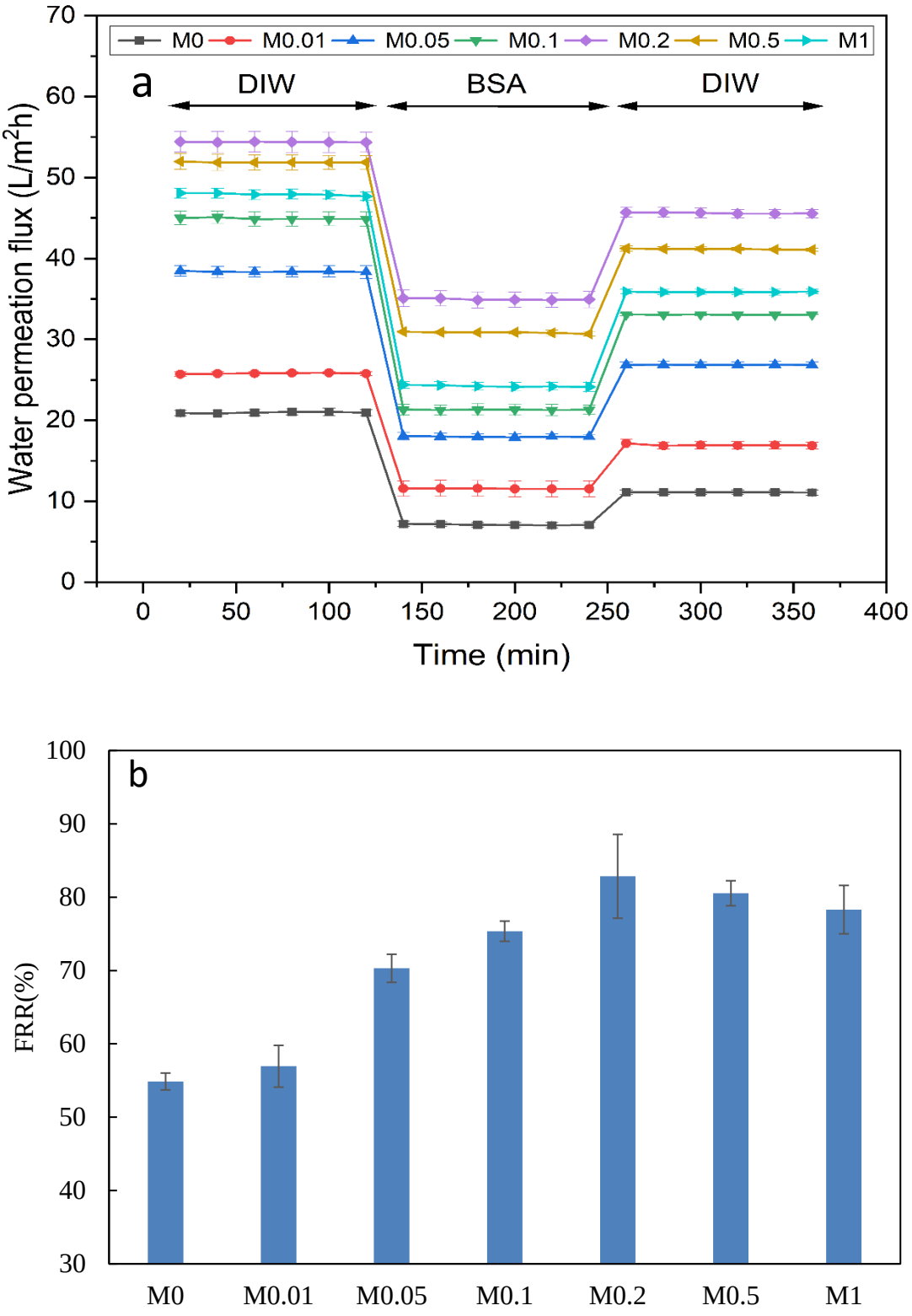

Fig. 5.17. Permeated water flux (a) vs time, and (b) FRR (flux recovery ratio) of the prepared membranes.

5.4. Conclusion

In this study, MIL-101(Cr)-NH_2 nanoparticles were incorporated into CA membranes, which helped improved membranes hydrophilicity and reduced the roughness of the modified membranes. Improve hydrophilicity and reduce the roughness of the membranes resulted in anti-fouling property improvement of the membranes. Water contact angle results showed that the WCA decreased from 65.1 ± 0.5 for M0 to 50.3 ± 1.9 for M1, which led to pure water flux enhancement. The Zeta potential measurements showed that by incorporating MIL-101 nanoparticles up to 0.5 wt%, the zeta potential increased from -27.6 ± 0.25 mV for M0 to -19 ± 0.35 mV for M0.5. However, by adding more MIL-101 nanoparticles from 0.5 to 1 wt%, the zeta potential increased from to -19 ± 0.35 mV for M0.5 to -10.4 ± 0.36 for M1 which can be attributed to the agglomeration of MIL-101 nanopartilces. MWCO results showed that enhancing MIL-101-(Cr)-NH_2 nanoparticles into the CA matrix from 0 to 0.2 wt% caused an enhancement of the mean pore diameter. However, by incorporating more MIL-101-(Cr)-NH_2 nanoparticles in the CA matrix membrane from 0.2 to 1 wt%, a reduction observed in the mean pore diameter that could be explained based on the accumulation of MIL-101-(Cr)-NH_2 nanoparticles and enhancing the viscosity of the casting solution. PWF at various pressure (0.2, 0.4, and 0.6 MPa) was obtained and results showed that PWF of all the prepared membranes was enhanced by increasing the applied pressure from 0.2 to 0.6 MPa. Although M0.2 showed the highest PWF at pressure 0.2 and 0.4 MPa, M1 showed the highest amount of PWF at pressure 0.6 MPa. For applied pressure (0.2, 0.4, and 0.6MPa), M0 showed the lowest PWF that can be attributed to its water contact angle and smaller pore size compared with other prepared membranes. Na_2SO_4, $MgSO_4$, and NaCl solution were considered to study the performance of prepared membranes for salt rejection and according to the results, for the prepared membranes, salt rejections reduced in the order of Na_2SO_4> $MgSO_4$ > NaCl that explained based on the electrostatic interaction and size exclusion.

CHAPTER VI

IMPROVING ANTIFOULING PROPERTY OF ALUMINA TUBULAR MICROFILTRATION MEMBRANES BY COATING HYDROPHILIC SILICA NANOPARTICLES FOR OIL/WATER TREATMENT

6.1. Introduction

Oily wastewater is a major environmental concern. Several industrial processes release oily wastewater into the environment, such as metallurgy, transportation, food processing, and the oil and gas industry, which negatively impacts the environment [208, 209]. “Produced water”, the water that is produced concomitantly with oil and gas extraction, is another source of oily wastewater which can cause significant environmental damage [210, 211]. It is important to look at oily wastewater to understand and design an efficient purification process for produced water. Various technologies have been tried for purifying oily wastewater and oil/water emulsions such as flocculation, membrane filtration, flotation, absorption, ultrasonic separation, coagulation, heating, ozonation, and electric fields [212-217]. Membrane technology is increasingly becoming a viable option for treating oily wastewater. Investigation for membrane separation technology for dealing with oily wastewater started in 1973 and since then gained appreciable momentum [218]. The main advantage that membrane separation provides over other technologies is efficient separation performance while maintaining a relatively simplistic operational process [219].

Among the various modes available for membrane separation processes, microfiltration (MF) and ultrafiltration (UF) can be efficient for oil/water separation [220, 221]. Different types of materials have been studied for MF and UF including polymer composites, metal meshes, filter paper, manganese oxide nanowire, textiles, silicon, and plastics [222-225]. Recently, there have been many reports wherein separation has been carried out in using the MF mode using polymer and ceramic membranes that showed promising results [226-228]. Membranes made out of ceramic materials such as alumina, zirconia, titania, and silica have attracted far more attention than other materials because of their biological stability and thermal, chemical, and mechanical resistances [229-231]. Many membranes (including paper, textile, and polymeric membranes) are cheaper than ceramic membranes but corrode far more easily. Alumina membranes are highly chemically inert and thus can be employed in a varied pH range [219]. Muller et al. applied an α-alumina membrane with a pore size of 0.8 μm for O/W emulsion separation with oil droplet size and concentration of 4 μm and 250 ppm, respectively. They reported stable permeability and rejection rate of 30 $L\ m^{-2}\ h^{-1}\ bar^{-1}$ and 30 %, respectively [232]. Hua et al. studied the performance of α-Al_2O_3 membrane with 50 nm pore size for oily wastewater treatment with 500 ppm oil concentration. The results showed stable permeability and rejection rate of 63.9 $L\ m^{-2}\ h^{-1}\ bar^{-1}$ and 98.1%, respectively [233].

Grafting and coating are two commonly used methods for modifying membranes to improve their fouling properties and enhance the efficiency of operation [234]. Zhang et al. improved the antifouling property of α-Al_2O_3 ceramic membrane by grafting the Zwitterionic monolayer. The results showed that zwitterion can immensely improve the flux and antifouling property of modified ultrafiltration membrane for O/W emulsions separation [235]. The coating has been practised using hydrophobic and hydrophilic substrates on membranes [236]. The main disadvantage of hydrophobic coating is the rapid increase in membrane fouling. The filtration process suffers and in the end, leads to a rise in this operational cost. To overcome these issues hydrophilic coatings can be used with high efficiency [237, 238]. Chang et al. improved the hydrophilicity of commercial Al_2O_3 membrane by coating it with nano-sized Al_2O_3 coating. The coating increased

the hydrophilicity of the membrane by altering the character of its surface that resulted in pure water flux enhancement by 27%. The authors also reported the water flux enhancement of the modified membrane by 20% compared with the pristine one.

This current work modifies α-alumina membranes with different loadings of hydrophilic fumed silica particles to improve the hydrophilicity of the membranes and increase their performance characteristics. Tests were conducted using pure DI water and oil in water (O/W) emulsions to evaluate the resistance to fouling and rejection of the oil phase.

6.2. Experimental

6.2.1. Materials

In this study, α-alumina tubular membrane (70mm length, 11mm outer diameter, 8mm inner diameter, 0.2 μm pore size) was provided from Ceramco, USA. Hydrophilic Si NPs (16 nm, A200, AEROSIL) were provided from Evonik, Germany. Polyvinyl alcohol (PVA, 80% hydrolyzed, average molecular weight 9000-10000) was purchased from Sigma-Aldrich.

6.2.2. Membrane preparation

Initially, the α-alumina tubular membrane was washed with DI water to remove dust and pollutants and then dried in an oven at 60 ℃ overnight. A coating solution was prepared by dispersing the hydrophilic silica NPs into deionized water and stirred for two hr to form a homogeneous silica-NPs solution at various weight percentages of 0.25%, 0.5%, 1%, and 3%. All the prepared membranes are named as shown in Table 6.1. Before coating Si NPs on the surface of the α-alumina tubular membrane, a pre-treatment process was applied using a PVA solution. For the pre-treatment process, the α-alumina tubular membrane was immersed in 10 wt.% PVA solution [20] and then dried in the oven at 60 °C overnight (Fig. 6.1a and b). The pre-treated membranes were then immersed in Si NPs solution at various weight percentages of 0.25%, 0.5%, 1%, and 3% several times and dried for a day (Fig. 6.1c). The fabricated membranes were then calcinated at 550 ºC for 3 hours to remove PVA (PVA melting point is 200 °C) and form mesoporous Silica coated membranes (Fig. 6.1d).

Table 6.1: The prepared membranes with various concentrations of Si NPs.

Membrane	Silica NPs (%)
M0	The pristine α-alumina
M0.25	0.25
M0.5	0.5
M1	1
M3	3

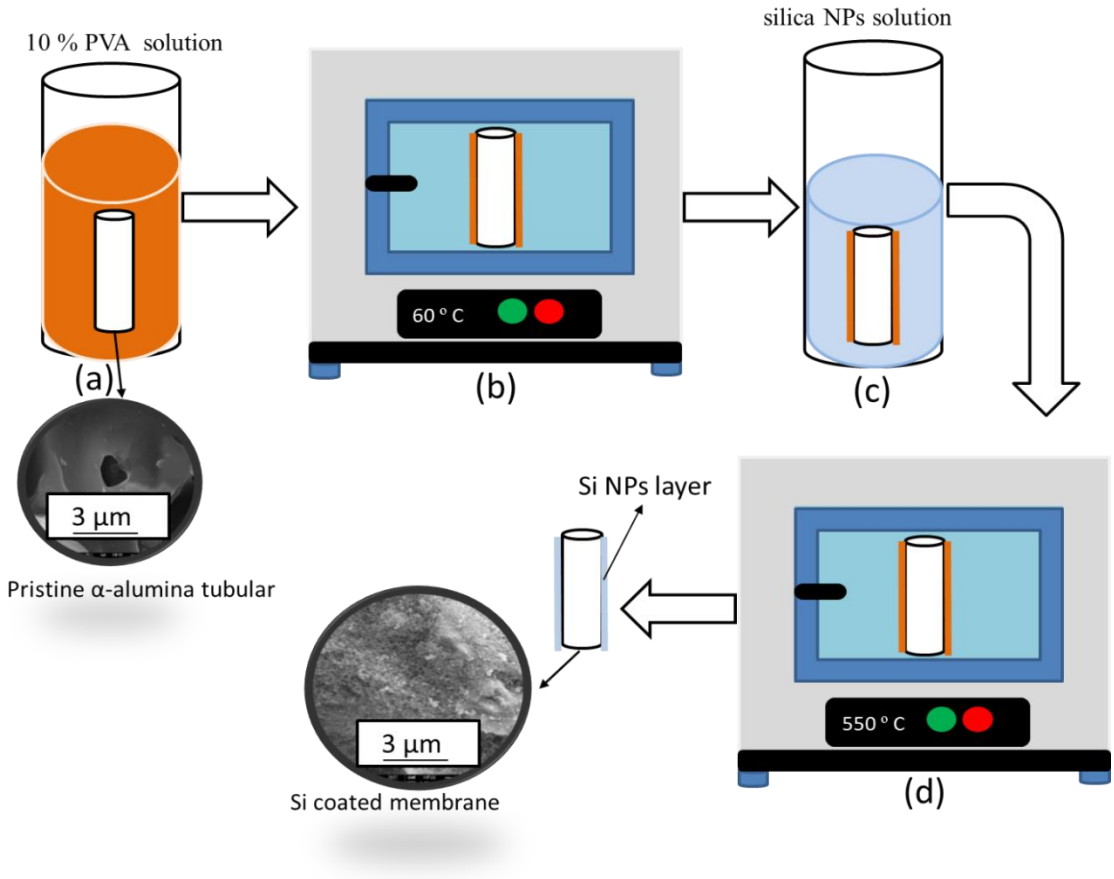

Fig. 6.1. The schematic diagram for the preparation process of the Si NPs coating on α-alumina tubular microfiltration membranes.

6.2.3. Membrane test

Microfiltration experiments were conducted in a cross-flow filtration system with the tubular membrane module with a membrane surface area of 16.2 cm^2 and at room temperature. The setup consists of a 37.8 L feed tank equipped with a Stenner Peristaltic Metering Pumps (USA) to pump the feed to the membrane module. A needle valve was installed in the output of the membrane module to pressurize the system. A by-pass line and a pressure gauge were used to set the pressure at a given value, and a flowmeter adjusted the feed flow rate on the retentate side. The permeate flow across the membrane was continuously collected and weighed by a digital balance. The retentate flow from the output of the membrane module was recycled to the feed tank. A scheme of the cross-flow filtration system is shown in Fig. 6.2.

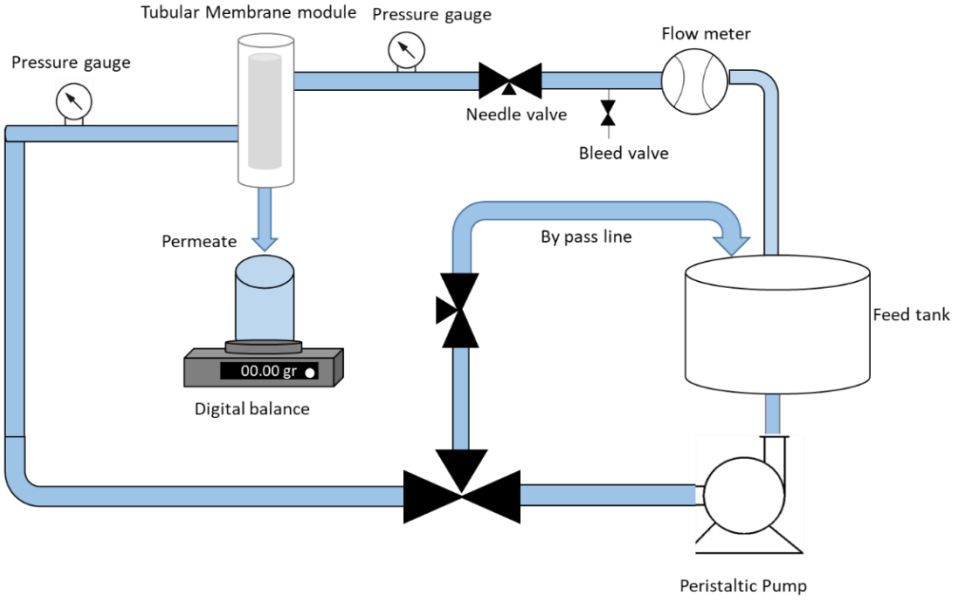

Fig. 6.2. Schematic of microfiltration cross-flow experimental set-up.

The performance of unmodified (the pristine α-alumina) and modified membranes was evaluated with pure water and O/W emulsion filtration. The permeate flux and oil rejection are significant parameters to assess membrane performance. The oil rejection was obtained as follows:

$$R\ (\%) = (1 - \frac{TOC_P}{TOC_F}) \times 100 \quad (1)$$

where R is oil rejection (%), and TOC_F and TOC_P are the total organic carbon concentration (Oil concentration) on feed and permeate side, respectively. The permeation flux was obtained using the following equation:

$$J = \frac{V}{A \times t} \quad (2)$$

where J is permeation flux (L m^{-2} h^{-1}), V (L) is the volume of water that passes through the membranes as permeate, A (m^2) is the effective membrane surface area, and t (h) is the permeation time.

6.2.4. Membrane characterization

An FEI Quanta 600F field emission scanning electron microscope (SEM) equipped with an energy dispersive spectrometry (EDS) was applied to observe the membranes' surface morphology and elemental composition. The prepared samples were coated with a thin layer gold layer with a thickness of 4-5 nm to avoid any charges. The oil contact angle (OCA) of the membrane surface was measured by a contact angle goniometer (Core Laboratories IFT-10) at room temperature. OCA was measured for three different spots of the membrane surface and the average amount was reported as the OCA of the α-alumina tubular and the prepared membranes. To measure the TOC, DR 5000™ UV-Vis spectrophotometer (HACH Company, USA) was applied in this study using Method 10173 (15 to 150 mg/L C). To study surface topology and membrane roughness before and after Si NPs coating, AFM, and MFP-3D Infinity Asylum Research (Santa Barbara, CA, USA) was used to study surface topography and membrane roughness. The samples were fixed on a holder double-side tape and 5 μm×5 μm areas of membranes were selected. Three different spots of the surface of the membrane were tested, and the average values of roughness were reported.

6.2.5. Emulsion analysis

O/W emulsions were prepared using cyclohexane as the oil phase, and DI water with a resistivity of 18.2 million ohm-cm was used as the continuous phase. A surfactant, Sodium Dodecyl Sulphate

(SDS), was used to make the emulsions. SDS is a water-soluble surfactant having an HLB value of 40. An Ultra-Turrax digital homogenizer was used for preparing the emulsions. An RPM of 15,000 was used. The homogenizer was kept running for 10 minutes after the last drop of cyclohexane was added to the water. The surfactant SDS was added to the continuous phase beforehand and the homogenizer was operated at 3000 RPM for 5 minutes to mix the surfactant in perfect dropwise addition of cyclohexane followed this example. The concentration of the oil phase was 1000 ppm and the weight percentage of surfactant was 0.13%. The optical analysis was carried out using an Olympus BX53 cross-polarized optical microscope. The microscope is equipped with a high-speed camera to analyze the droplet size of the emulsion accurately. Image J was used to analyze the images obtained from the microscope. Details of the methods for determining the emulsion droplet size distribution may be found elsewhere [239]. Fig. 6.3 shows the droplet size distribution of the emulsion used for the membrane tests. The mean droplet size (diameter) was found to be 3.07 ± 1.75 μm. Emulsions were prepared right before the start of an experiment.

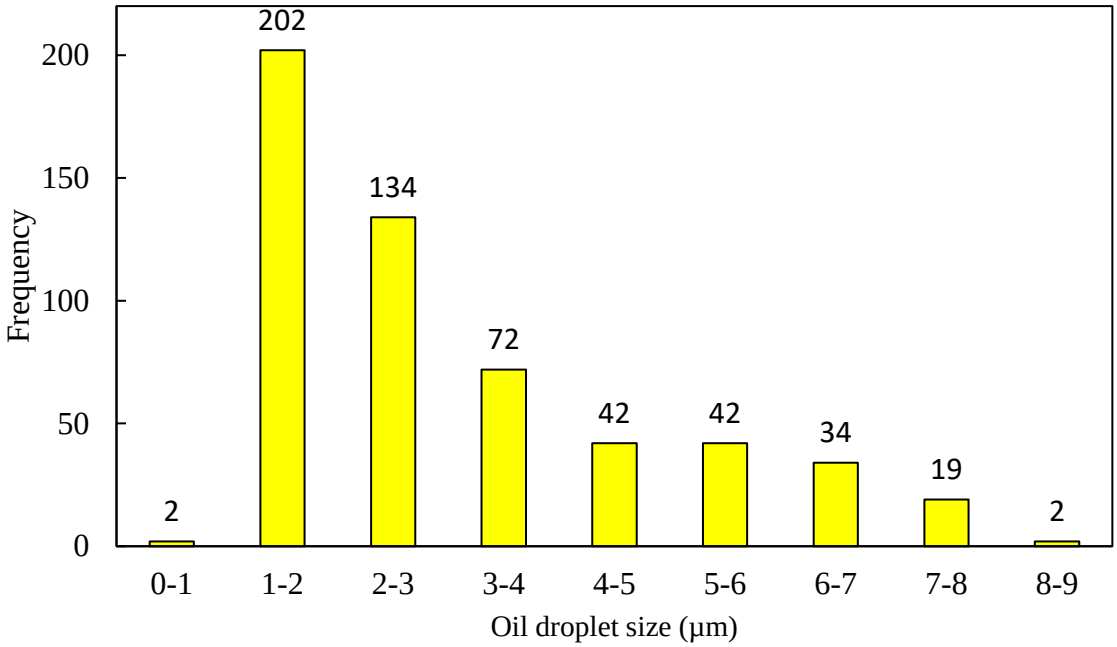

Fig.6.3 The oil droplet size distribution (diameter) of O/W emulsion.

6.3. Results and Discussion

6.3.1. Membrane Characterization

Fig. 6.4 shows the SEM cross-section of M0 and M3. The cross-section SEM with higher magnification shows that M0 has a rough structure. However, after coating Si NPs with a 3% concentration, a thin layer of Si with a thickness of 29 µm was coated on the surface of the α-alumina tubular membrane and the surface became smoother (Fig. 6.4 M3-b1-b2). The surface images of the α-alumina tubular membrane (M0) and modified membranes (M0.25-3) with Si NPs are given in Fig. 6.5. The Si NPs were coated on the surface and gradually covered the pore channels of the α-alumina tubular membrane (Fig. 6.5 M0.25-M3). With increasing Si NPs coating from 1% to 3%, the surface and most of the pore channels of the membrane were almost covered. (Fig. 6.5 M3-e1-2). In this case, the pores of the membrane were partially blocked.

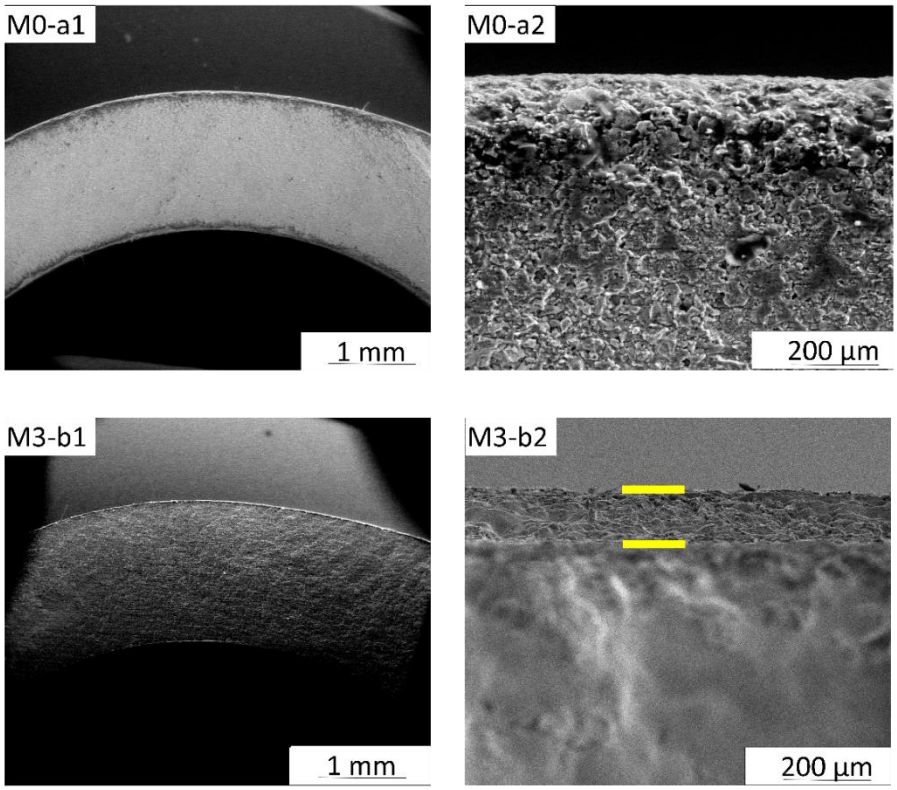

Fig. 6.4. The cross-section SEM images of (a1-2) M0 and (b1-2) M3.

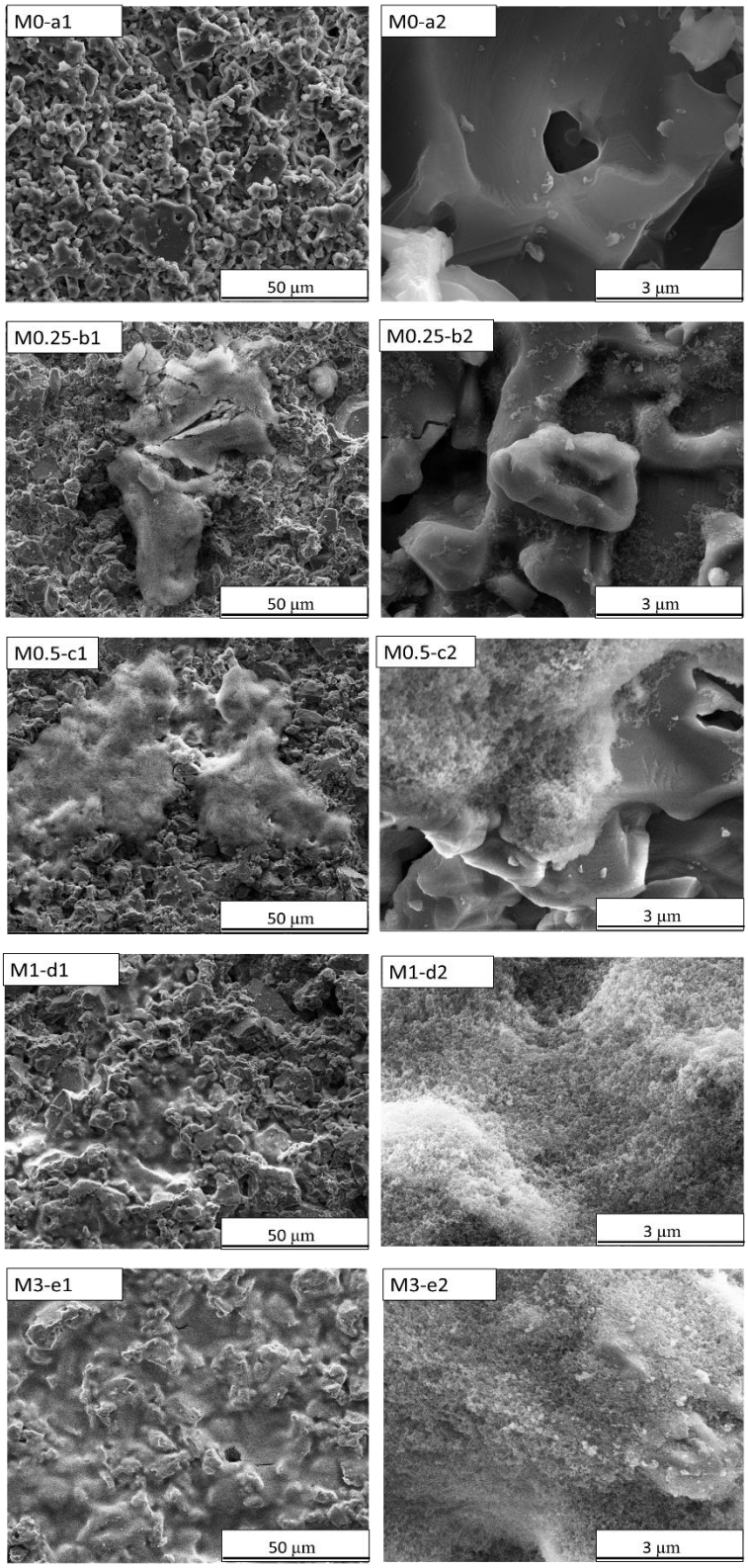

Fig. 6.5. The surface SEM images of (a) M0, (b) M0.25, (c) M0.5, (d) M1, (e) and M3.

Surface roughness plays an important role in the membrane fouling phenomena [240, 241]. The membrane becomes more vulnerable to fouling with the enhancement of membrane roughness because the rougher surface has more surface traps for particles to deposit [240]. After coating Si NPs, the AFM analysis was performed to study the changes in surface roughness. The AFM images (scan size of 20 μm × 20 μm) of uncoated and coated membranes are shown in Fig. 6.5, and the values of the surface roughness parameters of the membranes such as average roughness (Sa), root means square height (Sq), and the height difference between the highest peak and the lowest valley (St) are presented in Table 6.2. As indicated in Fig. 6.5a, the M0 membrane with "hill-and-valley" morphology has the roughest surface than the modified membranes. Fig. 6.6a-e confirmed that the surface of the modified membranes became smoother coating Si NPs. The decrement of roughness in surface properties of fabricated membranes leads to lower fouling since with reduction of the membrane roughness, traps on the membrane surface for containment immensely decreased. Si NPs coating turned the surface of the membrane into a smoother layer. More specifically, Sa, Sq, and St are 708 ± 40 nm, 877 ± 21 nm, and 6142 ± 451 nm for M0, respectively, while the corresponding roughness values decreased to 498 ± 161 nm, 623 ± 200 nm, and 4123 ± 1169 nm for M3.

Table 6.2. The surface roughness parameters of the membranes

Membrane name	Roughness Parameters		
	S_a (nm)	Sq (nm)	S_t (nm)
M0	708 ± 40	877 ± 21	6142 ± 451
M0.25	662 ± 33	825 ± 46	5678 ± 775
M0.5	593 ± 99	751 ± 121	5110 ± 1128
M1	505 ± 128	627 ± 160	4608 ± 1320
M3	498 ± 161	623 ± 200	4123 ± 1169

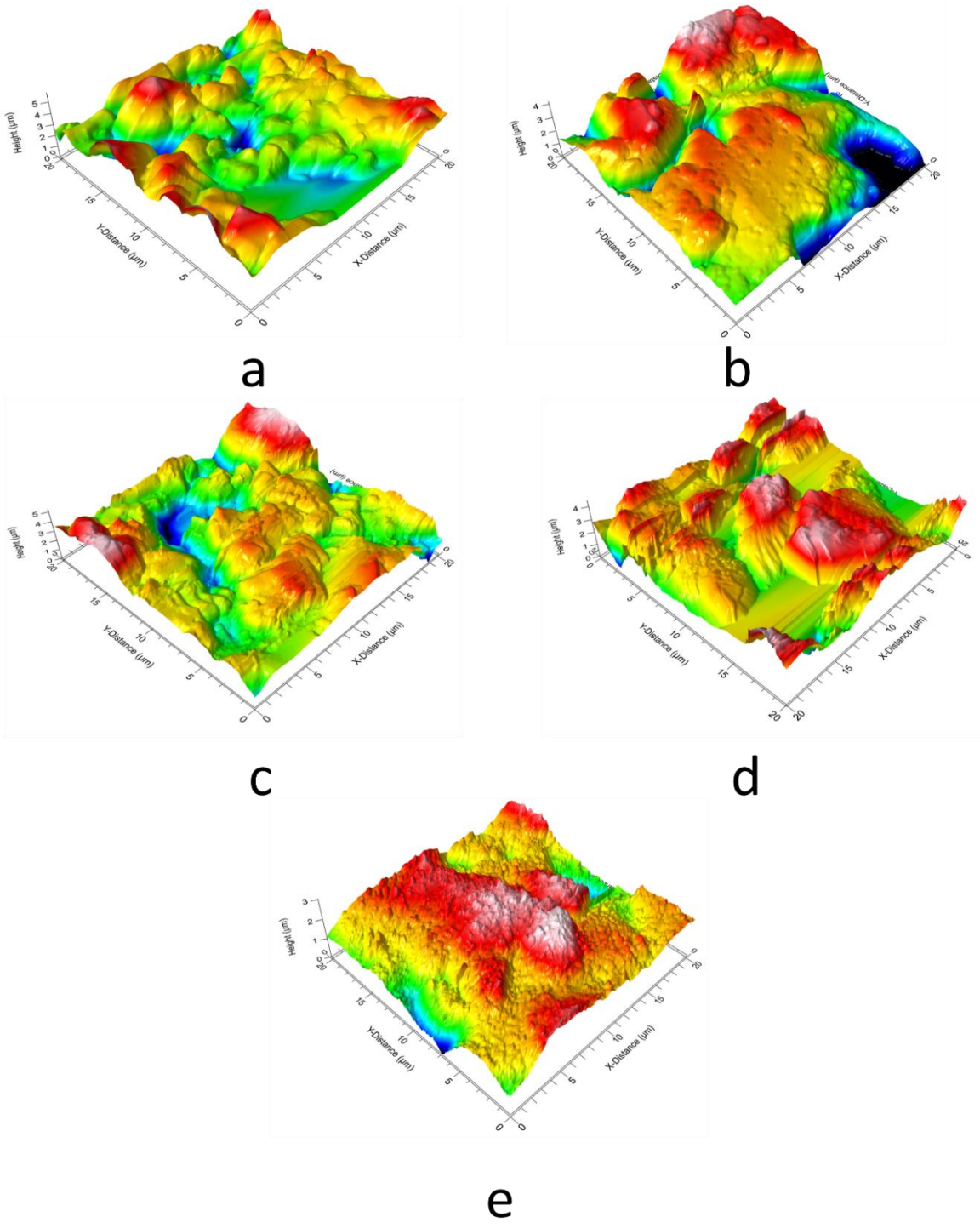

Fig. 6.6. AFM images of M0 (a), M0.25 (b), M0.5 (c), M1 (d), and M3 (e).

6.3.2. Si NPs leaching

To investigate the amount of Si NPs coating on the surface of the α-alumina membrane, EDS was performed on the M3 membrane. To study the effect of the pre-treatment process using PVA, we measured EDX for M3 fabricating without and with the PVA pre-treatment process. Three spots on the surface of M3 were selected to measure EDX as shown in Fig. 6.7. The spots were 1 cm apart from each other on the active surface area of the membrane. We marked the membrane on the inner side to recognize the area of the spots and used the SEM ruler to capture the same spots to get reliable data (Fig. 6.7). The EDX results for the amount of Si NPs coating are summarized in Table 6.3. According to the EDX result, the pre-treatment process using PVA improved Si NPs coating on the surface of the α-alumina membrane. The amount of Si NPs coated on α-alumina membrane spots 1, 2, and 3 increased from 4.28 %, 86%, and 3.99 % for the M3 membrane without the pre-treatment process to 34.22 %, 26.98 %, and 44.63 % for M3 membrane with the pre-treatment process, respectively. The coated Si NPs can be attributed to the sticky property of PVA, which helped to enhance Si NPs coating.

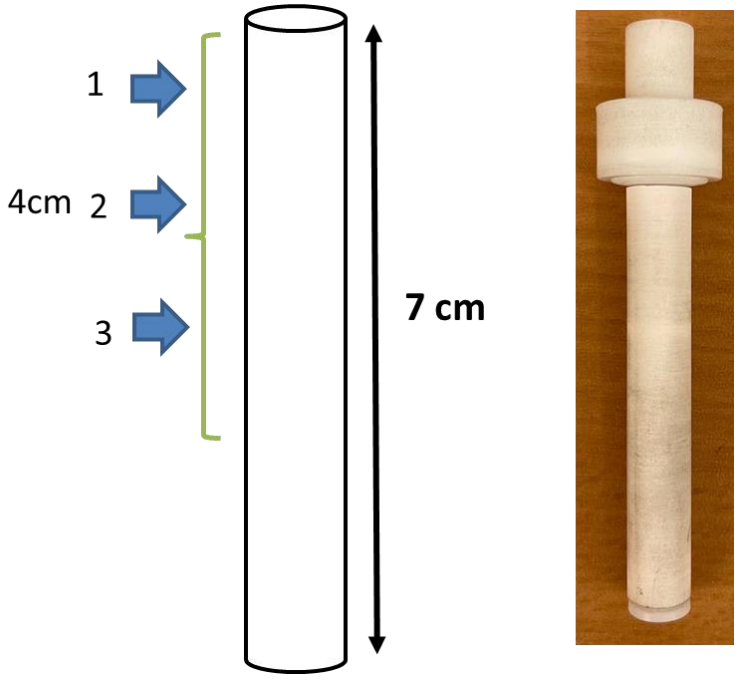

Fig. 6.7 The image of selected spots on membrane surface for performing EDX and its active surface area.

Table 6.3: The amount of Si NPs coated for M3 membrane synthesizing without and with the pre-treatment process.

Spots	Elements	The elemental membrane composition of M3 without the PVA pre-treatment	The elemental membrane composition of M3 with the PVA pre-treatment
1	Al	95.7	65.8
	Si	4.3	34.2
2	Al	93.1	73.0
	Si	6.9	26.9
3	Al	96.0	55.4
	Si	4	44.6

Using PVA as the pre-treatment process not only improved Si NPs coating but also decreased Si NPs leaching from the surface of the modified membranes. Si NPs leaching from the surface of M3 fabricating without and with PVA pre-treatment are summarized in Table 6.4. Using PVA before coating Si NPs helped stabilize Si NPs on the surface of the α-alumina tubular membrane. Even after 12 hours of O/W emulsion operation, a very small amount of Si NPs leached from the surface of M3 fabricating with PVA than without the PVA pre-treatment process. Silica leaching from spots 1, 2, and 3 on the surface of M3 increased from 0, 38.7%, and 9.4% for M3 fabricating with PVA to 21.7%, 76.7%, and 75% for M3 fabricating without PVA after 12 h operation of O/W emulsion filtration. Given that, the pre-treatment process using PVA stabilized Si NPs on the surface of the α-alumina tubular membrane.

Table 6.4: Si NPs leaching from surface of M3 fabricating with and without PVA after 12 h operation of O/W emulsion filtration.

spots	Silica leaching from M3 fabricating with PVA after 12 h operation of O/W emulsion filtration (%)	Silica leaching from M3 fabricating without PVA after 12 h operation of O/W emulsion filtration (%)
1	No leaching	21.7
2	38.7	76.7
3	9.4	75

6.3.3. Wettability Study as a function of ZnO ALD cycles

The wettability study of the unmodified membrane (M0) was evaluated by calculating Oil contact angel (OCA). We used the α-alumina tubular membranes and modified them by coating super hydrophilic Si NPs. To study the effect of Si NPs coating on the wettability of membranes, underwater OCA was calculated using cyclohexane (2 μL). As shown in Fig. 6.8, by coating Si NPs, OCA increased consequently, which means the Si NPs endowed hydrophilic property to the membranes. For instance, OCA increased from 133.9° for M0 to 171.4° for the M3 membrane.

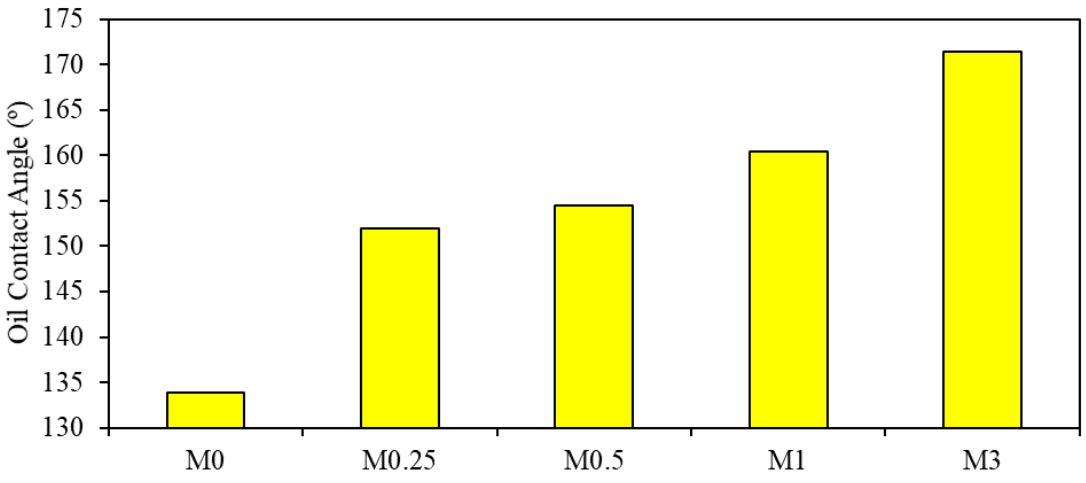

Fig. 6.8. Underwater oil contact angles of cyclohexane on the unmodified and modified membrane by coating Si NPs.

6.3.4. The membrane performance in terms of TOC rejection and flux

Fig. 6.9 represents water permeance of α-alumina membrane and modified membranes vs. time. As shown in Fig. 6.9, for all the membranes, the water permanence decreased during the O/W filtration operation because oil components were immediately deposited on the surface of the membrane, leading to the formation of a fouling (cake) layer. In this study, the steady permeate flux obtained after forming the stable cake layer started relatively from the third hour of O/W filtration operation (Fig. 6.9). The initial and stable permanence increased from 406 ± 8.5 and 246 ± 2.2 L m^{-2} h^{-1} bar^{-1} for M0 to 482 ± 3.4 and 312 ± 8.5 L m^{-2} h^{-1} bar^{-1} for M1, respectively (Table 6.5). The water permanence enhancement can be assigned to the hydrophilic improvement of M1 by coating Si NPs. After increasing Si NPs coating from %1 to %3, the corresponding values decreased to 459 ± 3.96 and 279 ± 5.9 L m^{-2} h^{-1} bar^{-1} because after coating more Si NPs pore channels of the modified membranes became blocked (Fig. 6.3 e1-2). The water permanence for the M3 membrane that was fabricated without PVA pre-treatment decreased significantly compared with other membranes attributed to Si NPs leaching from the membrane surface

Table 6.5: Initial and stable permanence of the α-alumina and modified membranes.

Membranes	Initial permeance (L m^{-2} h^{-1} bar^{-1})	Stable permeance (L m^{-2} h^{-1} bar^{-1})
M0	406 ± 8.5	246 ± 2.2
M0.25	420 ± 3	244 ± 4.1
M0.5	450 ± 11.9	264 ± 4
M1	482 ± 3.4	312 ± 8.5
M3	459 ± 3.96	279 ± 5.9
M3 without the PVA pre-treatment	417 ± 1.7	229 ± 2.4

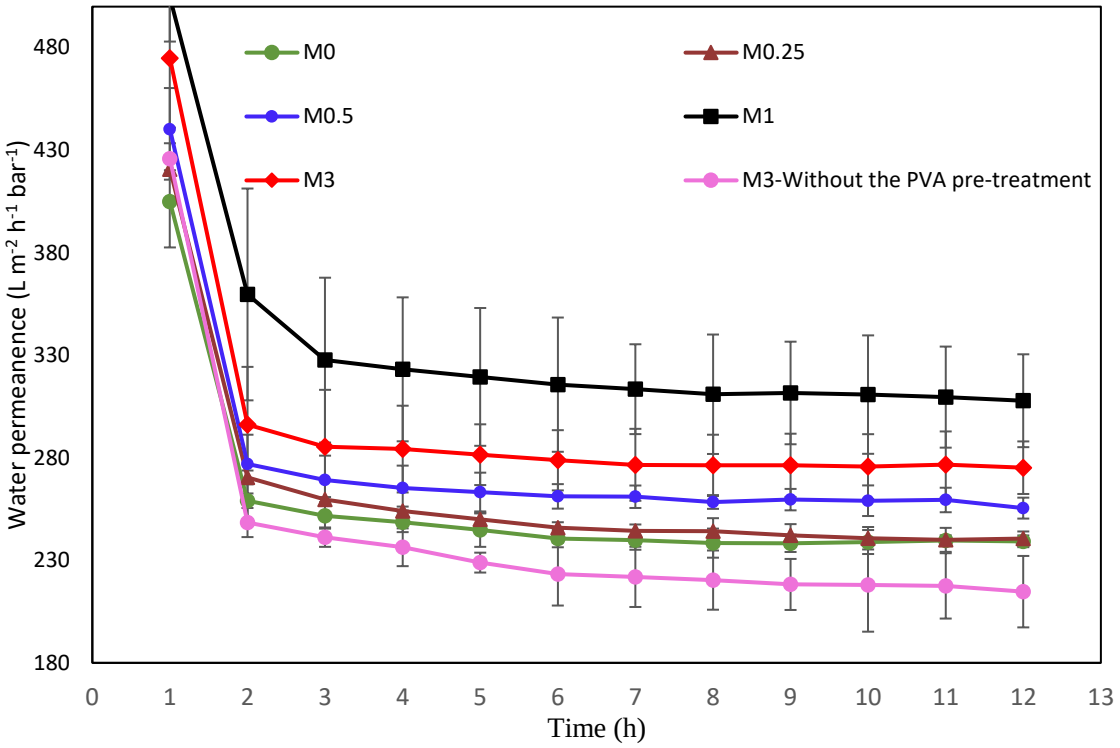

Fig. 6.9. Water permeance for various membranes vs. time.

Fig. 6.10 indicates the performance of membranes in terms of organic components removal for the first three hours of O/W operation filtration. The modified membranes showed better performance than an unmodified membrane (M0). TOC rejection increased from 93.1% ± 0.4 for M0 to 97.7% ± 0.25 for M3 because of hydrophilic improvement of the modified membranes (Fig. 6.8). In addition, by coating Si NPs on the membrane surface, the pore size of membranes decreased (Fig. 6.4b1-2). The TOC rejection increased from 1st hour to 3rd hour of O/W filtration operation for almost all the tested membranes. The reason is that by running the O/W filtration process, since pure water was extracted from O/W emulsion over time, the oil concentration increased in the feed tank. Consequently, the membranes' pore channels were mostly covered and blocked, and then oily particles were added into a cake layer over the membrane surface [110, 242]. Thus, increasing the oil concentration, resulted in an extra decline in penetration through the membrane which caused higher TOC rejection [242, 243].

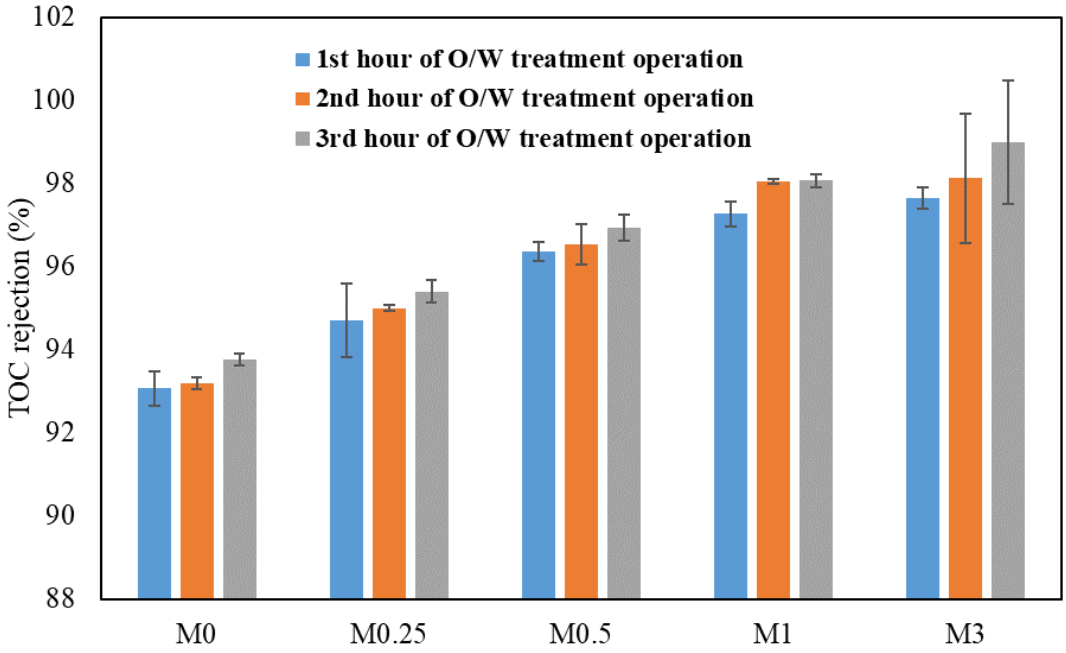

Fig. 6.10. TOC rejection of various membranes for the first three hours of O/W treatment filtration.

6.3.5. Anti-fouling properties of the membranes

The anti-fouling property of the unmodified and modified membranes immensely depends upon the hydrophilic property of the membranes. Therefore, we studied the fouling-resistant property of the prepared membranes by treating O/W emulsion. Fig. 6.11 shows the FRR (flux recovery ratio) of the unmodified (M0) and modified membranes by Si NPs coating. As exhibited, in all O/W treatment operations, FRR increased from 71.3% for M0 to 85.9% for M1, which can be attributed to the hydrophilic improvement of modified membranes after coating super hydrophilic Si NPs (Fig. 6.8). However, by coating more Si NPs, FRR decreased immensely from 85.9% for M1 to 67.7% for M3 attributed to Si NPs accumulation on the membrane surface that blocked the pores of the modified membranes. Another possible explanation for increasing FRR can be roughness reduction after coating Si NPs resulting in lower valleys and alleys for oil components to stick on the membrane surfaces.

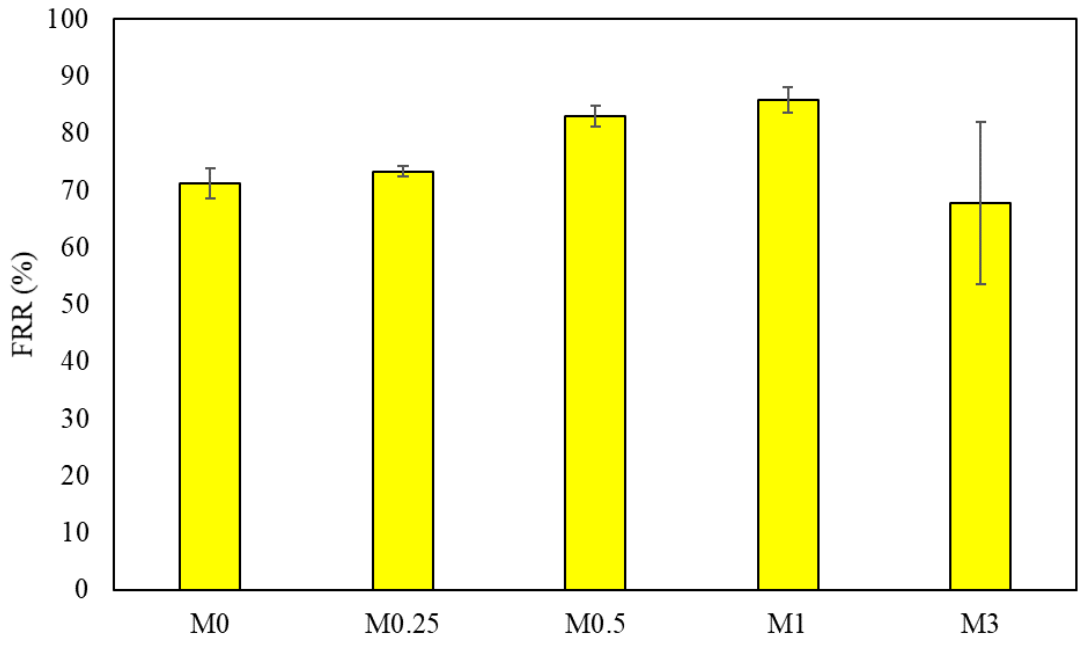

Fig. 6.11 Flux recovery ratios (FRR) of the unmodified and modified membranes.

6.3.6. Comparison of membranes in the literature

As shown in Table 6.6, various membranes for filtering oil-in-water emulsion are summarized in terms of the membrane material and configuration, oil concentration, filtration operation condition, and performance of the membranes in terms of flux and oil rejection. Although we filtered out O/W emulsion at the lowest pressure to find a potential membrane for industry application, flux, and oil rejection in this study were relatively high compared with most of the other studies.

Table 6.6 performance comparison of ceramic MF membranes for treating oil-in-water emulsion in the literature.

Materials	configuration	Pore size (μm)	Oil concentration (ppm)	TMP (bar)	Droplet size (μm)	Permeance ($Lm^{-2}h^{-1}$ bar^{-1})	R(%)	Refs
Mullite	Hollow fiber	0.7	500	0.15	1	880	97	[258]
Modified Al_2O_3	Tubular	0.14	1000	1.6	1.79	505	98.5	[252]
Fly ash/Al_2O_3	Cylindrical	0.1	200	0.5	0.06-10	165	99.2	[249]
Mullite monolith	Tubular	0.4	1000	1	1.09	35	93.8	[260]
Kaolin-Quartz	Flat	1.06	100	2.07	0.99	96	87	[261]
Mullite monolith	Tubular	0.45	1000	2.07	2	48.6	97.6	[259]
Silicon Carbide	Circular disk	0.4	500	0.5	1	324	98.5	[262]
α-Al_2O_3	Tubular	0.2	1000	0.35	1-9	311.5	96.5	This study

6.4. Conclusion

Si NPs were coated on the α-alumina tubular membrane support using dip-coating that improved membrane hydrophilicity and reduced the roughness of the modified membranes. The modified membranes with Si NPs coating showed excellent flux and antifouling property. Using PVA helped to stabilize Si NPs on the membranes surface more efficiently. Embedding Si NPs increased oil contact angle which this factors endow the membrane high flux. M1 showed better performance compared with other membranes and we have plan to evaluate the performance of M1 membrane for real produced water. The decrement of roughness in surface properties of fabricated membranes leads to lower fouling since with reduction of the membrane roughness, traps on the membrane surface for containment immensely decreased. Si NPs coating turned the surface of the membrane into a smoother layer and among the membranes, M1 showed excellent fouling resistant. The initial and stable permanence increased from 406.2 ± 8.5 and 245.7 ± 2.2 L m^{-2} h^{-1} bar^{-1} for M0 to 482.4 ± 3.4 and 311.5 ± 8.5 L m^{-2} h^{-1} bar^{-1} for M1, respectively. In addition, TOC rejection increased from 93.1% ± 0.4 for M0 to 97.7% ± 0.25 for M3 because of hydrophilic improvement of the modified membranes.

CHAPTER VII

SUMMARY AND FUTURE WORK

7.1. Microporous membranes for oil/water separation and desalination

This work aimed to fabricate and assess ceramic and polymeric membranes to identify potential commercial membranes for removing organic and salt components. In this dissertation, three inorganic and one organic membranes including NaA zeolite-coated mesh, α-alumina flat sheet, α-alumina tubular and cellulose acetate membranes were synthesized and tested successfully. All of membranes were applied to the treatment of oil/water emulsion and desalination purposes. The first membrane, NaA zeolite-based membrane was fabricated on a stainless steel mesh by secondary growth method through optimizing aluminum/silicon ratio (ASR) to effectively separate oily water. The NaA zeolite-coated mesh with the highest superoleophobic property had an ASR of 1.21 and an oil contact angle of 163.7o. The highest membrane flux obtained was 13,513 L m^{-2} h^{-1} for ASR = 0.91 and the highest separation efficiency was 99.5% for ASR = 1.21. NaA zeolite meshes were recycled and reused for 15 cycles by rinsing the membrane with DI water between each test.

The oil rejection rate of the mesh for ASR = 0 decreased approximately 2.7% after 4 cycles of separation, but the oil rejection rate of the meshes for ASRs = 0.3-182 did not change with 4 cycles of oil water separation, which is attributed to the uniformity of the NaA zeolite coating and its thermal stability.

For the second membrane, ZnO atomic layer deposition (ALD) modified membranes were developed for treating produced water from wells in Oklahoma, as a model of produced water, having very high salt and oil content. ZnO ALD membranes increased hydrophilicity with an oil contact angle increasing from 165° for an α-alumina support to 171° for a ZnO ALD membrane (120 cycles), which induced a dramatic rise in the pure water flux from 148 to 192 L m^{-2} h^{-1}. ZnO ALD on the membranes enhanced Total Organic Carbon (TOC) rejection from 96% to 99% and decreased Total Dissolved Solids (TDS) content from 53,205 ppm to 10 ppm. The results showed that the average roughness (Sa) was 509 nm for the pristine α-alumina support and was reduced to 332 nm for the ZnO ALD membrane (120 cycles). Additionally, the anti-fouling property of membranes with flux recovery ratio increased from 93% to 99%. Overall, the ZnO ALD membrane showed great potential to purify produced water.

In the third study, mixed matrix membranes were developed by embedding hydrophilic nanoparticles (MIL-101 (Cr)-NH_2) into cellulose acetate (CA) matrix to enhance hydrophilicity. This helped in countering the inevitable problem of fouling that membranes face when used for the treatment of industrial wastewater, by enhancing hydrophilicity. Synthesized membranes were characterized by Fourier transform infrared (FTIR) spectroscopy, transmission electron microscopy (TEM), scanning electron microscopy (SEM), water contact angle, and atomic force microscopy (AFM). These mixed matrix membrane structures showed impressive stability with a negligible change in water contact angle even after 30 days. The inclusion of MIL-101(Cr)-NH_2 into the CA membrane helped in reducing the water contact angle from ~ 65.1˚ to ~ 50.3˚, thus improving hydrophilicity. Adding as little as 1 wt. % MIL-101(Cr)-NH_2 into the CA matrix enhanced the pure water flux to 68.1 ± 0.87 LMH, an increase of ~ 150% compared to pristine CA membrane owing

to its enhanced hydrophilicity and higher pore size while maintaining similar salt rejection. The prepared membranes also showed impressive rejection (>97%) on the basis of size exclusion mechanism for Methyl Blue (MB) dye. Moreover, flux recovery ratio (FRR) increased from ~ 54.3% for pristine CA to ~ 82% for mixed matrix membrane having 0.2 wt.% containing MIL-101(Cr)-NH_2, thus showing significant enhancement of the antifouling property of the prepared membrane.

Lastly, super hydrophilic silica nanoparticles (Si NPs) were used to modify tubular α-alumina membranes to improve their performance in terms of flux, oil rejection, and antifouling properties. The prepared membranes were applied for oil/water (O/W) emulsion treatment. By coating the membranes with Si NPs, their hydrophilicity was improved, and the oil contact angle (OCA) reached 133.8 for M0 to 171.4 for M3. To prevent Si NP leaching from the surface of the α-alumina tubular membrane, a polyvinyl alcohol (PVA) coating was first used as a pre-treatment step. By coating the membrane with Si NPs, the surface roughness and associated containment traps on the membrane surface decreased, which resulted in less fouling. TOC rejection increased from 93.1% ± 0.4 for M0 to 97.7% ± 0.25 for M3 because of hydrophilic improvements of the modified membranes. The Si NP coating improved the anti-fouling property of membranes with flux recovery ratio increased from 71.3% for M0 to 85.9% for M1. SEM (Scanning Electron Microscopy), EDS (Energy-dispersive X-ray spectroscopy), OCA, and AFM (Atomic Force Microscopy) characterization tests were applied to study morphology, the amount of Si NPs, wettability, and surface roughness of the fabricated membranes, respectively.

7.2 Comparison with other researchers

We utilized a novel and robust nanofiltration membrane in aim III with low energy consumption and chemical free to treat underground water and surface water to convert to portable water which meets the EPA requirements. The membrane worked in nanofiltration scale which demands tremendously lower energy than a reverse osmosis (RO) membrane since nanofiltration membranes operate at lower pressure than RO. The longevity of the membrane was superior due to its anti-

fouling properties. The prepared membranes were re-used using inexpensive backwash techniques with water unlike current membranes that require chemical cleaning. All these benefits combined has helped us reduce the operational cost of running a membrane unit of filtration by 50%. Based on our current pricing strategy the customer will get a 1.6X benefit for the investment they make on our membrane. In Summary, our nano filter membrane is easy to use and pocket friendly. The membranes were developed a novel nanofiltration membrane by taking advantage of interfacial polymerization. Nanofiltration membranes are between non-porous reverse osmosis (RO) membranes and porous ultrafiltration (UF) membranes. These allow ions to be separated through a combination of size & electrical effects of ultrafiltration (UF) membranes and ion interaction mechanisms of reverse osmosis (RO) membranes. The membrane preparation includes two major steps. First, synthesizing nanoparticles known as metal organic framework (MOF) and functionalize it to increase its hydrophilicity. In the second step, the polyamide membrane was prepared by the phase inversion method. The polyamide solution was poured on the surface of non-woven to stabilize the membrane structure. The polyamide film was then placed inside water for the phase inversion process. Finally, nanoparticles were embedded inside the polyamide. The lab-scale membrane dimension is (8-inch length, 4-inch width, 140-micrometer thickness). Another important feature is the flexibility of our product in terms of scalability. We will be able to provide industrial membrane in any dimension because phase inversion is a facile method to scale up from bench to pilot scale. The industrial membrane preparation is as follows:

- The first step is MOF preparation. Based on our estimation, it takes two weeks to prepare 10 kg of MOF using industrial equipment.
- Second, full-scale membrane casting. Each industrial bath of membrane consists of 10,000 m^2.
- Third, the prepared flat membrane sheet should be tested to make sure that the scale-up process does not decrease the membrane performance, and this step can be called quality control.
- Then, the prepared membranes are rolled into a spiral form and sent to the next section.

- The final step will be gluing and winding of spiral-wound membrane. The envelopes are glued to separate feed and permeate sides. The envelopes are rolled into a spiral and taped for curing. The final product will be applied to membrane modules for treating water and wastewater. Various dimensions (in terms of length, width, and diameter) of industrial membranes are prepared using different prototypes. These porotypes are used to make sure that the final product meets standard dimensions.

Intellectual Property The intellectual property for this technology belongs to Oklahoma State University Technology Development Center (TDC). Since this technology will be owned by Oklahoma State University, the OSU Intellectual Property Office will manage and complete all paperwork associated with the pursuit of intellectual property filings, including patent protection. Furthermore, the university will cover the full capital cost and take all risk associated with patent filing and procurement.

Our sales strategy is a B2B strategy, and our immediate customers are Nanofiltration module distributors and Nanofiltration equipment makers. Our end users are the food and beverage companies, municipalities, farmers, and homeowners. Currently the customers using the nano filters present in the market face the following issues:

- They will have to replace the Nanofilters every 12 months
- They will have to use expensive cleaning technologies to clean their membranes which not only increases the overall cost but also increases the carbon footprint.

With our filter the customer can replace the filter every 18months meaning our Nanofilters provide a 1.5 more longevity compared to the ones present in the market. Third, the prepared membrane can be re-used using inexpensive backwash techniques with water unlike current membranes that require chemical cleaning. The surge in the utilization of Nanofiltration membranes in most of the industrial sectors, especially food and beverages, chemicals, and wastewater treatment industry, is a major Nanofiltration membrane market growth driver and this surge seems to be huge in both the

developing and developed countries. In developing countries, the need for efficient, low-cost water filters are surging as the availability of water continue to reduce.

7.3 Future work

To identify a potential industrial membrane, one must overcome membrane drawbacks such as fouling. Besides that, improve fabrication process of membranes in terms of cost is another parameter that should be considered. In this dissertation, the various fabrication and modification techniques were applied to enhance anti-fouling property of the membranes for water treatment purposes. It has been found that modification of membranes using hydrophilic nanoparticles can improve fouling-resistance property. We also studied stabilizing the hydrophilic nanoparticles in the membrane structure while keeping anti-fouling property of the membranes.

as explained in chapters 3, 4, 5, and 6, the fabricated inorganic membranes (NaA zeolite-coated mesh, α-alumina flat sheet, and α-alumina tubular) and organic membrane (cellulose acetate) showed excellent performance on a lab-scale for water treatment purposes. Nevertheless, to scale up these membranes for commercial application, we need to test the membrane for longer time to assure anti-fouling property remains unchanged. Then, results reproducibility of the fabricated membranes should be examined by national labs to make certain our results are re-creatable. After recreating the results, testing membranes in industrial scale is challengeable since operating condition and membrane dimensions might affect results. Hence, further study on numerical simulation of the membrane fouling process and optimal operational condition might be helpful to fabricate membranes for industrial application with lower cost.

REFERENCES

1. Liu, H., et al., Review on the aerogel-type oil sorbents derived from nanocellulose. Acs.Sustain.Chem.Eng. , 2016. 5(1): p. 49-66. 2. Liu, Y., et al.,
2. Zhang, C., et al., Synthesis of MnO2/poly (n-butylacrylate-co-butyl methacrylate-co-methyl methacrylate) hybrid resins for efficient oils and organic solvents absorption. Journal of Cleaner Production, 2017. **148**: p. 398-406.
3. Zhang, C., et al., Synthesis of MnO2/poly (n-butylacrylate-co-butyl methacrylate-co-methyl methacrylate) hybrid resins for efficient oils and organic solvents absorption. J.cleaner.produ. , 2017. **148**: p. 398-406.
4. Zhang, T., et al., A novel multi-wall carbon nanotubes/poly (n-butylacrylate-co-butyl methacrylate) hybrid resin: synthesis and oil/organic solvents absorption. Fibers and Polymers, 2017. **18**(10): p. 1865-1873.
5. Li, Z., et al., Facile one-step fabrication of highly hydrophobic, renewable and mechanically flexible sponge with dynamic coating for efficient oil/water separation. J.Tai. Instit.Chem.Eng. , 2019. **95**: p. 515-524.
6. Li, J.-J., L.-T. Zhu, and Z.-H. Luo, Electrospun fibrous membrane with enhanced swithchable oil/water wettability for oily water separation. Chem. Eng. J., 2016. **287**: p. 474-481.
7. Zheng, X., et al., Underwater self-cleaning scaly fabric membrane for oily water separation. ACS Appl. Mater. Interfaces., 2015. **7**(7): p. 4336-4343.
8. Yue, X., et al., Design and fabrication of superwetting fiber-based membranes for oil/water separation applications. Chem. Eng. J., 2019.
9. Pan, Z., et al., Anti-fouling TiO2 nanowires membrane for oil/water separation: Synergetic effects of wettability and pore size. J.Membr.Sci., 2019. **572**: p. 596-606.
10. Xiong, Z., et al., Robust superhydrophilic polylactide (PLA) membranes with a TiO 2 nano-particle inlaid surface for oil/water separation. J. Mater. Chem. A, 2017. **5**(14): p. 6538-6545.
11. Chen, W., et al., The improved oil/water separation performance of cellulose acetate-graft-polyacrylonitrile membranes. Journal of Membrane Science, 2009. **337**(1-2): p. 98-105.
12. De Guzman, M.R., et al., Increased performance and antifouling of mixed-matrix membranes of cellulose acetate with hydrophilic nanoparticles of polydopamine-sulfobetaine methacrylate for oil-water separation. Journal of Membrane Science, 2020: p. 118881.
13. Zhao, C., et al., Modification of polyethersulfone membranes–a review of methods. Progress in Materials Science, 2013. **58**(1): p. 76-150.
14. Ikhsan, S.N.W., et al., Efficient separation of oily wastewater using polyethersulfone mixed matrix membrane incorporated with halloysite nanotube-hydrous ferric oxide nanoparticle. Separation and Purification Technology, 2018. **199**: p. 161-169.
15. Guo, X., et al., Engineering polydopamine-glued sandwich-like nanocomposites with antifouling and antibacterial properties for the development of advanced mixed matrix membranes. Separation and Purification Technology, 2020. **237**: p. 116326.

16. Efome, J.E., et al., Insight studies on metal-organic framework nanofibrous membrane adsorption and activation for heavy metal ions removal from aqueous solution. ACS applied materials & interfaces, 2018. **10**(22): p. 18619-18629.
17. Kausar, A., Scientific potential of chitosan blending with different polymeric materials: A review. Journal of Plastic Film & Sheeting, 2017. **33**(4): p. 384-412.
18. Loos, C., et al., Functionalized polystyrene nanoparticles as a platform for studying bio–nano interactions. Beilstein journal of nanotechnology, 2014. **5**(1): p. 2403-2412.
19. Jiang, J.-H., et al., Improved hydrodynamic permeability and antifouling properties of poly (vinylidene fluoride) membranes using polydopamine nanoparticles as additives. Journal of membrane science, 2014. **457**: p. 73-81.
20. Kim, Y.S. and S.M. Yang, Preparation of continuous mesoporous silica thin film on a porous tube. Advanced Materials, 2002. **14**(15): p. 1078-1081.
21. Van der Bruggen, B., et al., A review of pressure-driven membrane processes in wastewater treatment and drinking water production. Environmental progress, 2003. **22**(1): p. 46-56.
22. Ahmad, N.N.R., et al., Nanofiltration membrane processes for water recycling, reuse and product recovery within various industries: A review. Journal of Water Process Engineering, 2022. **45**: p. 102478.
23. Manikandan, S., et al., A critical review of advanced nanotechnology and hybrid membrane based water recycling, reuse, and wastewater treatment processes. Chemosphere, 2022. **289**: p. 132867.
24. Bera, S.P., M. Godhaniya, and C. Kothari, Emerging and advanced membrane technology for wastewater treatment: A review. Journal of Basic Microbiology, 2022. **62**(3-4): p. 245-259.
25. Selatile, M.K., et al., Recent developments in polymeric electrospun nanofibrous membranes for seawater desalination. RSC advances, 2018. **8**(66): p. 37915-37938.
26. Saleh, T.A., M. Mustaqeem, and M. Khaled, Water treatment technologies in removing heavy metal ions from wastewater: A review. Environmental Nanotechnology, Monitoring & Management, 2022. **17**: p. 100617.
27. Breck, D., Structure, Chemistry and Use of Zeolite Molecular Sieves. 1974, Wiley, New York.
28. Asif, M.B. and Z. Zhang, Ceramic membrane technology for water and wastewater treatment: A critical review of performance, full-scale applications, membrane fouling and prospects. Chemical Engineering Journal, 2021. **418**: p. 129481.
29. Scott, K., Handbook of industrial membranes. 1995: Elsevier.
30. Hubadillah, S.K., et al., Recent progress on low-cost ceramic membrane for water and wastewater treatment. Ceramics International, 2022.
31. Vatanpour, V., et al., Nanomaterials in membrane bioreactors: Recent progresses, challenges, and potentials. Chemosphere, 2022. **302**: p. 134930.
32. Tavangar, T., et al., Textile waste, dyes/inorganic salts separation of cerium oxide-loaded loose nanofiltration polyethersulfone membranes. Chemical Engineering Journal, 2020. **385**: p. 123787.
33. Buekenhoudt, A., et al., Unravelling the solvent flux behaviour of ceramic nanofiltration and ultrafiltration membranes. Journal of membrane science, 2013. **439**: p. 36-47.
34. Peng, B., et al., Cellulose-based materials in wastewater treatment of petroleum industry. Green Energy & Environment, 2020. **5**(1): p. 37-49.
35. Wang, W., et al., Dual super-amphiphilic modified cellulose acetate nanofiber membranes with highly efficient oil/water separation and excellent antifouling properties. Journal of hazardous materials, 2020. **385**: p. 121582.

36. Shoba, B., J. Jeyanthi, and S. Vairam, Synthesis, characterization of cellulose acetate membrane and application for the treatment of oily wastewater. Environmental technology, 2020. **41**(12): p. 1590-1605.
37. Tynell, T. and M. Karppinen, Atomic layer deposition of ZnO: a review. Semiconductor Science and Technology, 2014. **29**(4): p. 043001.
38. Liang, R., et al., Fundamentals on adsorption, membrane filtration, and advanced oxidation processes for water treatment, in Nanotechnology for Water Treatment and Purification. 2014, Springer. p. 1-45.
39. Cui, Z., Y. Jiang, and R. Field, Fundamentals of pressure-driven membrane separation processes, in Membrane technology. 2010, Elsevier. p. 1-18.
40. Liu, H., et al., Review on the aerogel-type oil sorbents derived from nanocellulose. 2016. **5**(1): p. 49-66.
41. Liu, Y., et al., Fabrication of functional biomass carbon aerogels derived from sisal fibers for application in selenium extraction. 2018. **111**: p. 93-103.
42. Liu, Y., et al., Superhydrophobic, ultralight and flexible biomass carbon aerogels derived from sisal fibers for highly efficient oil–water separation. 2018. **25**(5): p. 3067-3078.
43. Rong, J., et al., A facile strategy toward 3D hydrophobic composite resin network decorated with biological ellipsoidal structure rapeseed flower carbon for enhanced oils and organic solvents selective absorption. 2017. **322**: p. 397-407.
44. Fragouli, D. and A.J.N.n. Athanassiou, Oil spill recovery: Graphene heaters absorb faster. 2017. **12**(5): p. 406.
45. Banerjee, S.S., M.V. Joshi, and R.V.J.C. Jayaram, Treatment of oil spill by sorption technique using fatty acid grafted sawdust. 2006. **64**(6): p. 1026-1031.
46. Zhang, T., et al., Enhanced oils and organic solvents absorption by polyurethane foams composites modified with MnO2 nanowires. 2017. **309**: p. 7-14.
47. Zhang, C., et al., Synthesis of MnO2/poly (n-butylacrylate-co-butyl methacrylate-co-methyl methacrylate) hybrid resins for efficient oils and organic solvents absorption. 2017. **148**: p. 398-406.
48. Zhang, T., et al., A novel multi-wall carbon nanotubes/poly (n-butylacrylate-co-butyl methacrylate) hybrid resin: synthesis and oil/organic solvents absorption. 2017. **18**(10): p. 1865-1873.
49. Li, Z., et al., Facile one-step fabrication of highly hydrophobic, renewable and mechanically flexible sponge with dynamic coating for efficient oil/water separation. 2019. **95**: p. 515-524.
50. Li, J.-J., L.-T. Zhu, and Z.-H.J.C.E.J. Luo, Electrospun fibrous membrane with enhanced swithchable oil/water wettability for oily water separation. 2016. **287**: p. 474-481.
51. Zheng, X., et al., Underwater self-cleaning scaly fabric membrane for oily water separation. 2015. **7**(7): p. 4336-4343.
52. Yue, X., et al., Design and fabrication of superwetting fiber-based membranes for oil/water separation applications. 2019.
53. Pan, Z., et al., Anti-fouling TiO2 nanowires membrane for oil/water separation: Synergetic effects of wettability and pore size. 2019. **572**: p. 596-606.
54. Xiong, Z., et al., Robust superhydrophilic polylactide (PLA) membranes with a TiO 2 nano-particle inlaid surface for oil/water separation. 2017. **5**(14): p. 6538-6545.
55. Wang, Z.-X., et al., Mussel-inspired tailoring of membrane wettability for harsh water treatment. 2015. **3**(6): p. 2650-2657.
56. Nguyen, T., F. Roddick, and L.J.M. Fan, Biofouling of water treatment membranes: a review of the underlying causes, monitoring techniques and control measures. 2012. **2**(4): p. 804-840.
57. Li, C., et al., Polysulfide-blocking microporous polymer membrane tailored for hybrid Li-sulfur flow batteries. 2015. **15**(9): p. 5724-5729.

58. Elia, G.A. and J.J.S.S.I. Hassoun, A gel polymer membrane for lithium-ion oxygen battery. 2016. **287**: p. 22-27.
59. Servatan, M., et al., Zeolite-based catalysts for exergy efficiency enhancement: The insights gained from nanotechnology. 2018. **5**(7): p. 15868-15876.
60. Feng, X., et al., Kr/Xe separation over a chabazite zeolite membrane. 2016. **138**(31): p. 9791-9794.
61. Baerlocher, C., L.B. McCusker, and D.H. Olson, Atlas of zeolite framework types. 2007: Elsevier.
62. Wei, X.-L., et al., Patching NaA zeolite membrane by adding methylcellulose into the synthesis gel. 2017. **530**: p. 240-249.
63. Lee, S.M., et al., Gas permeation properties of NaA zeolite membranes: effect of silica source on hydrogel synthesis and layer thickness. 2019: p. 1-9.
64. al., A.D.K.e., Fabrication, characterization, and application of palladium composite membrane on porous stainless steel substrate with Nay zeolite as an intermediate layer for hydrogen purification. Journal of HYDROGEN ENERGY, 2019. **44**(2019): p. 2889-2904.
65. Jiang, J., et al., Effect of Si/Al ratio in the framework on the pervaporation properties of hollow fiber CHA zeolite membranes. 2019. **273**: p. 196-202.
66. Li, X.-Q., et al., Facial build-up of acid-resistance skin for high-stability zeolite NaA membrane. 2019. **573**: p. 55-63.
67. Liu, F., M.M. Abed, and K. Li, Preparation and characterization of poly (vinylidene fluoride)(PVDF) based ultrafiltration membranes using nano γ-Al2O3. Journal of membrane science, 2011. **366**(1-2): p. 97-103.
68. Ju, H., et al., Crosslinked poly (ethylene oxide) fouling resistant coating materials for oil/water separation. 2008. **307**(2): p. 260-267.
69. Li, H.-J., et al., Development and characterization of anti-fouling cellulose hollow fiber UF membranes for oil–water separation. 2006. **279**(1-2): p. 328-335.
70. Kasemset, S., et al., Effect of polydopamine deposition conditions on fouling resistance, physical properties, and permeation properties of reverse osmosis membranes in oil/water separation. 2013. **425**: p. 208-216.
71. Zhang, S., et al., Bio-inspired anti-oil-fouling chitosan-coated mesh for oil/water separation suitable for broad pH range and hyper-saline environments. 2013. **5**(22): p. 11971-11976.
72. Wang, Z. and S.J.W.r. Lin, Membrane fouling and wetting in membrane distillation and their mitigation by novel membranes with special wettability. 2017. **112**: p. 38-47.
73. Feng, L., et al., A super-hydrophobic and super-oleophilic coating mesh film for the separation of oil and water. 2004. **43**(15): p. 2012-2014.
74. Xue, Z., et al., A novel superhydrophilic and underwater superoleophobic hydrogel-coated mesh for oil/water separation. 2011. **23**(37): p. 4270-4273.
75. Tian, D., et al., Photo-induced water–oil separation based on switchable superhydrophobicity–superhydrophilicity and underwater superoleophobicity of the aligned ZnO nanorod array-coated mesh films. 2012. **22**(37): p. 19652-19657.
76. Tian, D., et al., Micro/nanoscale hierarchical structured ZnO mesh film for separation of water and oil. 2011. **13**(32): p. 14606-14610.
77. Yan, L., et al., A photo-induced ZnO coated mesh for on-demand oil/water separation based on switchable wettability. 2016. **163**: p. 247-249.
78. Li, J., et al., Facile fabrication of underwater superoleophobic TiO2 coated mesh for highly efficient oil/water separation. 2016. **489**: p. 441-446.
79. Li, J., et al., Facile fabrication of underwater superoleophobic SiO2 coated meshes for separation of polluted oils from corrosive and hot water. 2016. **168**: p. 209-214.
80. Kang, M.K. and R.J.S.M. Huang, Effect of surface tension on swell-induced surface instability of substrate-confined hydrogel layers. 2010. **6**(22): p. 5736-5742.

81. Zhang, J. and W.J.J.o.m.s. Liu, Thin porous metal sheet-supported NaA zeolite membrane for water/ethanol separation. 2011. **371**(1-2): p. 197-210.
82. Li, J., et al., A prewetting induced underwater superoleophobic or underoil (super) hydrophobic waste potato residue-coated mesh for selective efficient oil/water separation. 2016. **18**(2): p. 541-549.
83. Liu, J., et al., Continuous removal of Cr (VI) and Orange II over a novel Fe0-NaA zeolite membrane catalyst. 2019. **209**: p. 734-740.
84. Loiola, A., et al., Structural analysis of zeolite NaA synthesized by a cost-effective hydrothermal method using kaolin and its use as water softener. 2012. **367**(1): p. 34-39.
85. Liu, R., et al., Hydrophilicity-controlled MFI-type zeolite-coated mesh for oil/water separation. Sep. Purif. Technol., 2018. **195**: p. 163-169.
86. Wen, Q., et al., Zeolite-coated mesh film for efficient oil–water separation. Chem. Sci., 2013. **4**(2): p. 591-595.
87. Li, J., et al., A prewetting induced underwater superoleophobic or underoil (super) hydrophobic waste potato residue-coated mesh for selective efficient oil/water separation. Green.Chem. , 2016. **18**(2): p. 541-549.
88. Liu, R., et al., Boron substituted MFI-type zeolite-coated mesh for oil-water separation. Colloids Surf., A, 2018. **550**: p. 108-114.
89. Liu, R., et al., Hydrophilicity-controlled MFI-type zeolite-coated mesh for oil/water separation. 2018. **195**: p. 163-169.
90. Kota, A.K., et al., Hygro-responsive membranes for effective oil–water separation. 2012. **3**: p. 1025.
91. Huang, A., et al., Fabrication of zinc oxide nanostructure coated membranes for efficient oil/water separation. 2018. **566**: p. 249-257.
92. Guisnet, M., Q. Wang, and G.J.C.l. Giannetto, Dealumination of NH 4 NaY zeolites through hydrothermal treatment: Kinetic order with respect to aluminium. 1990. **4**(4-6): p. 299-302.
93. Malola, S., et al., Detailed reaction paths for zeolite dealumination and desilication from density functional calculations. 2012. **51**(3): p. 652-655.
94. Tanudjaja, H.J., et al., Membrane-based separation for oily wastewater: A practical perspective. Water research, 2019.
95. Holdich, R., I. Cumming, and I. Smith, Crossflow microfiltration of oil in water dispersions using surface filtration with imposed fluid rotation. Journal of membrane science, 1998. **143**(1-2): p. 263-274.
96. Chen, A., et al., Removal of oil, grease, and suspended solids from produced water with ceramic crossflow microfiltration. SPE production engineering, 1991. **6**(02): p. 131-136.
97. Zouboulis, A. and A. Avranas, Treatment of oil-in-water emulsions by coagulation and dissolved-air flotation. Colloids and Surfaces A: Physicochemical and Engineering Aspects, 2000. **172**(1-3): p. 153-161.
98. Rattanapan, C., et al., Enhanced efficiency of dissolved air flotation for biodiesel wastewater treatment by acidification and coagulation processes. Desalination, 2011. **280**(1-3): p. 370-377.
99. Yang, C., et al., Solvent extraction process development and on-site trial-plant for phenol removal from industrial coal-gasification wastewater. Chemical Engineering Journal, 2006. **117**(2): p. 179-185.
100. Sadeghalvad, B., A. Azadmehr, and A. Hezarkhani, A new approach to improve sulfate uptake from contaminated aqueous solution: Metal layered double hydroxides functionalized metasomatic rock. Separation Science and Technology, 2019. **54**(4): p. 447-466.
101. Ramaswamy, B., D. Kar, and S. De, A study on recovery of oil from sludge containing oil using froth flotation. Journal of environmental management, 2007. **85**(1): p. 150-154.

102. Sadeghalvad, B. and A. Azadmehr, Comparative study effects of calcinations, electrolytes, and Fe-bentonite, CaCO3-bentonite on the removal of Cd (II) ions from aqueous solution. Desalination and Water Treatment, 2016. **57**(25): p. 11879-11892.
103. Suehara, K.-i., et al., Biological treatment of wastewater discharged from biodiesel fuel production plant with alkali-catalyzed transesterification. Journal of bioscience and bioengineering, 2005. **100**(4): p. 437-442.
104. Pitakpoolsil, W. and M. Hunsom, Adsorption of pollutants from biodiesel wastewater using chitosan flakes. Journal of the Taiwan Institute of Chemical Engineers, 2013. **44**(6): p. 963-971.
105. Sadeghalvad, B., B.K. Moghaddam, and S.A. Hamidi. Evaluation of Bassanite Efficiency as an Adsorbent for Iron Decontamination in Aqueous Solution. in World Environmental and Water Resources Congress 2019: Groundwater, Sustainability, Hydro-Climate/Climate Change, and Environmental Engineering. 2019. American Society of Civil Engineers Reston, VA.
106. Yang, Z., V.V. Tarabara, and M.L. Bruening, Adsorption of anionic or cationic surfactants in polyanionic brushes and its effect on brush swelling and fouling resistance during emulsion filtration. Langmuir, 2015. **31**(43): p. 11790-11799.
107. Salahi, A., et al., Experimental performance evaluation of polymeric membranes for treatment of an industrial oily wastewater. Desalination, 2010. **262**(1-3): p. 235-242.
108. Madaeni, S.S., et al., Removal of coke particles from oil contaminated marun petrochemical wastewater using PVDF microfiltration membrane. Industrial & engineering chemistry research, 2011. **50**(20): p. 11712-11719.
109. Mahmodi, G., et al., NaA Zeolite-Coated Meshes with Tunable Hydrophilicity for Oil-Water Separation. Separation and Purification Technology, 2020: p. 116630.
110. Ebrahimi, M., et al., Investigations on the use of different ceramic membranes for efficient oil-field produced water treatment. Desalination, 2010. **250**(3): p. 991-996.
111. Mahmodi, G., et al., From microporous to mesoporous mineral frameworks: An alliance between zeolite and chitosan. 2020. **489**: p. 107930.
112. Yang, X., et al., Polyphenol-sensitized atomic layer deposition for membrane interface hydrophilization. Advanced Functional Materials, 2020. **30**(15): p. 1910062.
113. Pinson, J. and D. Thiry, Surface modification of polymers: methods and applications. 2020: John Wiley & Sons.
114. Abadi, S.R.H., et al., Ceramic membrane performance in microfiltration of oily wastewater. Desalination, 2011. **265**(1-3): p. 222-228.
115. Madaeni, S.S., et al., Coke removal from petrochemical oily wastewater using γ-Al2O3 based ceramic microfiltration membrane. Desalination, 2012. **293**: p. 87-93.
116. Shih, J.-S., et al., Characterization and analysis of liquid waste from Marcellus Shale gas development. Environmental science & technology, 2015. **49**(16): p. 9557-9565.
117. Zhang, Z., et al., Effective treatment of shale oil and gas produced water by membrane distillation coupled with precipitative softening and walnut shell filtration. Desalination, 2019. **454**: p. 82-90.
118. Chen, X., et al., Plasma-induced poly (acrylic acid)-TiO2 coated polyvinylidene fluoride membrane for produced water treatment: Synchrotron X-Ray, optimization, and insight studies. Journal of cleaner production, 2019. **227**: p. 772-783.
119. Kusworo, T.D. and D.P. Utomo, Performance evaluation of double stage process using nano hybrid PES/SiO2-PES membrane and PES/ZnO-PES membranes for oily waste water treatment to clean water. Journal of environmental chemical engineering, 2017. **5**(6): p. 6077-6086.
120. Zinadini, S., et al., Preparation of a novel antifouling mixed matrix PES membrane by embedding graphene oxide nanoplates. Journal of Membrane Science, 2014. **453**: p. 292-301.

121. Servatan, M., et al., Zeolites in drug delivery: progress, challenges and opportunities. 2020.
122. Hesas, R.H., et al., An investigation on the capability of magnetically separable Fe3O4/mordenite zeolite for refinery oily wastewater purification. Journal of environmental management, 2019. **241**: p. 525-534.
123. Huang, Z.-Q., et al., Effect of ferrosoferric oxide content on the performances of polysulfone–ferrosoferric oxide ultrafiltration membranes. Journal of Membrane Science, 2008. **315**(1-2): p. 164-171.
124. Kull, K.R., M.L. Steen, and E.R. Fisher, Surface modification with nitrogen-containing plasmas to produce hydrophilic, low-fouling membranes. Journal of membrane science, 2005. **246**(2): p. 203-215.
125. Zhang, C.-H., et al., Preparation and characterization of hydrophilic modification of polypropylene non-woven fabric by dip-coating PVA (polyvinyl alcohol). Separation and Purification Technology, 2008. **61**(3): p. 276-286.
126. Ulbricht, M. and G. Belfort, Surface modification of ultrafiltration membranes by low temperature plasma II. Graft polymerization onto polyacrylonitrile and polysulfone. Journal of Membrane Science, 1996. **111**(2): p. 193-215.
127. Bruening, M.L., et al., Creation of functional membranes using polyelectrolyte multilayers and polymer brushes. Langmuir, 2008. **24**(15): p. 7663-7673.
128. Yang, H.-C., et al., Surface engineering of polymer membranes via mussel-inspired chemistry. Journal of Membrane Science, 2015. **483**: p. 42-59.
129. Weber, M., et al., Atomic layer deposition for membranes: Basics, challenges, and opportunities. Chemistry of Materials, 2018. **30**(21): p. 7368-7390.
130. Yang, H.-C., et al., Atomic layer deposition for membrane interface engineering. Nanoscale, 2018. **10**(44): p. 20505-20513.
131. Li, F., et al., Modification of ceramic membranes for pore structure tailoring: The atomic layer deposition route. Journal of membrane science, 2012. **397**: p. 17-23.
132. Juholin, P., et al., Comparison of ALD coated nanofiltration membranes to unmodified commercial membranes in mine wastewater treatment. Separation and Purification Technology, 2018. **192**: p. 69-77.
133. Xu, Q., et al., Hydrophilization of porous polypropylene membranes by atomic layer deposition of TiO2 for simultaneously improved permeability and selectivity. Journal of membrane science, 2013. **448**: p. 215-222.
134. Chen, H., et al., Ceramic tubular nanofiltration membranes with tunable performances by atomic layer deposition and calcination. Journal of Membrane Science, 2017. **528**: p. 95-102.
135. Xu, Q., et al., Atomic layer deposition of alumina on porous polytetrafluoroethylene membranes for enhanced hydrophilicity and separation performances. Journal of membrane science, 2012. **415**: p. 435-443.
136. Li, F., et al., Precise pore size tuning and surface modifications of polymeric membranes using the atomic layer deposition technique. Journal of membrane science, 2011. **385**: p. 1-9.
137. Li, N., et al., Hydrophilic modification of polyvinylidene fluoride membranes by ZnO atomic layer deposition using nitrogen dioxide/diethylzinc functionalization. Journal of Membrane Science, 2016. **514**: p. 241-249.
138. Li, N., et al., Static adsorption of protein-polysaccharide hybrids on hydrophilic modified membranes based on atomic layer deposition: Anti-fouling performance and mechanism insight. Journal of Membrane Science, 2018. **548**: p. 470-480.
139. Nikkola, J., et al., Surface modification of thin film composite polyamide membrane using atomic layer deposition method. Journal of membrane science, 2014. **450**: p. 174-180.

140. Ras, R.H., et al., Hollow inorganic nanospheres and nanotubes with tunable wall thicknesses by atomic layer deposition on self-assembled polymeric templates. Advanced Materials, 2007. **19**(1): p. 102-106.
141. Johs, B., et al. Overview of variable-angle spectroscopic ellipsometry (VASE): II. Advanced applications. in Optical Metrology: A Critical Review. 1999. International Society for Optics and Photonics.
142. Wang, Q., et al., PVDF membranes with simultaneously enhanced permeability and selectivity by breaking the tradeoff effect via atomic layer deposition of TiO2. Journal of membrane science, 2013. **442**: p. 57-64.
143. Minahan, D.M. and G.B. Hoflund, Study of Cs-Promoted, α-Alumina-Supported Silver Ethylene-Epoxidation Catalysts: I. Characterization of the Support and As–Prepared Catalyst. Journal of Catalysis, 1996. **158**(1): p. 109-115.
144. Ahmad, N., C. Leo, and A. Ahmad, Superhydrophobic alumina membrane by steam impingement: minimum resistance in microfiltration. Separation and Purification Technology, 2013. **107**: p. 187-194.
145. Shen, L., et al., Preparation and characterization of ZnO/polyethersulfone (PES) hybrid membranes. Desalination, 2012. **293**: p. 21-29.
146. McCloskey, B.D., et al., A bioinspired fouling-resistant surface modification for water purification membranes. Journal of membrane science, 2012. **413**: p. 82-90.
147. Jia, X., et al., Atomic layer deposition of Al2O3 on porous polypropylene hollow fibers for enhanced membrane performances. Chinese journal of chemical engineering, 2018. **26**(4): p. 695-700.
148. Xiong, S., et al., Dye adsorption on zinc oxide nanoparticulates atomic-layer-deposited on polytetrafluoroethylene membranes. AIChE Journal, 2016. **62**(11): p. 3982-3991.
149. Li, Y., et al., Controlling wettability, wet strength, and fluid transport selectivity of nanopaper with atomic layer deposited (ALD) sub-nanometer metal oxide coatings. Nanoscale Advances, 2020.
150. Alam, J., et al., Atomic layer deposition of TiO 2 film on a polyethersulfone membrane: separation applications. Journal of Polymer Research, 2016. **23**(9): p. 183.
151. Ruppert, T.K., Water Quality Trading and Agricultural Nonpoint Source Pollution: An Analysis of the Effectiveness and Fairness of EPA's Policy on Water Quality Trading. Vill. Envtl. LJ, 2004. **15**: p. 1.
152. Korin, E., I. Ladizhensky, and E. Korngold, Hydrophilic hollow fiber membranes for water desalination by the pervaporation method. Chemical Engineering and Processing: Process Intensification, 1996. **35**(6): p. 451-457.
153. Korngold, E., E. Korin, and I. Ladizhensky, Water desalination by pervaporation with hollow fiber membranes. Desalination, 1996. **107**(2): p. 121-129.
154. Copeland, C., S. Resources, and I. Division. Animal waste and water quality: EPA regulation of concentrated animal feeding operations (CAFOs). 2006. Congressional Research Service, the Library of Congress.
155. Nady, N., et al., Modification methods for poly (arylsulfone) membranes: A mini-review focusing on surface modification. Desalination, 2011. **275**(1-3): p. 1-9.
156. Ghiasi, S., et al., Effect of surface charge and roughness on ultrafiltration membranes performance and polyelectrolyte nanofiltration layer assembly. Colloids and Surfaces A: Physicochemical and Engineering Aspects, 2019. **580**: p. 123753.
157. Sobel, N., et al., Conformal SiO2 coating of sub-100 nm diameter channels of polycarbonate etched ion-track channels by atomic layer deposition. Beilstein journal of nanotechnology, 2015. **6**(1): p. 472-479.
158. Yang, H.-C., et al., Crude-oil-repellent membranes by atomic layer deposition: oxide interface engineering. ACS nano, 2018. **12**(8): p. 8678-8685.

159. Zhang, H., et al., Drawing on Membrane Photocatalysis for Fouling Mitigation. ACS Applied Materials & Interfaces, 2021. **13**(13): p. 14844-14865.
160. Zhang, H., et al., Visible-light-activated photocatalytic films toward self-cleaning membranes. Advanced Functional Materials, 2020. **30**(34): p. 2002847.
161. Holkar, C.R., et al., A critical review on textile wastewater treatments: possible approaches. Journal of environmental management, 2016. **182**: p. 351-366.
162. Lin, J., et al., Tight ultrafiltration membranes for enhanced separation of dyes and Na2SO4 during textile wastewater treatment. Journal of Membrane Science, 2016. **514**: p. 217-228.
163. Othman, M.H.D., et al., Advanced Membrane Technology for Textile Wastewater Treatment, in Membrane Technology Enhancement for Environmental Protection and Sustainable Industrial Growth. 2021, Springer. p. 91-108.
164. Rezakazemi, M., et al., Fouling-resistant membranes for water reuse. Environmental Chemistry Letters, 2018. **16**(3): p. 715-763.
165. Vatanpour, V., et al., Nanostructured polyethersulfone nanocomposite membranes for dual protein and dye separation: Lower antifouling with lanthanum (III) vanadate nanosheets as a novel nanofiller. Polymer Testing, 2020: p. 107040.
166. Zhang, S., et al., Water-soluble MOF nanoparticles modified polyethersulfone membrane for improving flux and molecular retention. Applied Surface Science, 2020. **505**: p. 144553.
167. Lin, Y., et al., Preparation of high-performance Al2O3/PES composite hollow fiber UF membranes via facile in-situ vapor induced hydrolyzation. Journal of Membrane Science, 2017. **539**: p. 65-75.
168. Zhong, W., et al., Superhydrophobic membranes via facile bio-inspired mineralization for vacuum membrane distillation. Journal of Membrane Science, 2017. **540**: p. 98-107.
169. Abidin, M.N.Z., et al., Antifouling polyethersulfone hemodialysis membranes incorporated with poly (citric acid) polymerized multi-walled carbon nanotubes. Materials Science and Engineering: C, 2016. **68**: p. 540-550.
170. Zare, S. and A. Kargari, Membrane properties in membrane distillation, in Emerging Technologies for Sustainable Desalination Handbook. 2018, Elsevier. p. 107-156.
171. Song, X., et al., Effects of sulphur on the performance of an anaerobic membrane bioreactor: Biological stability, trace organic contaminant removal, and membrane fouling. Bioresource technology, 2018. **250**: p. 171-177.
172. Zhu, X., et al., A charge-density-tunable three/two-dimensional polymer/graphene oxide heterogeneous nanoporous membrane for ion transport. ACS nano, 2017. **11**(11): p. 10816-10824.
173. Miller, D.J., et al., Surface modification of water purification membranes. Angewandte Chemie International Edition, 2017. **56**(17): p. 4662-4711.
174. Lee, X.J., et al., Surface grafting techniques on the improvement of membrane bioreactor: State-of-the-art advances. Bioresource technology, 2018. **269**: p. 489-502.
175. Li, X., et al., Progress and perspectives for synthesis of sustainable antifouling composite membranes containing in situ generated nanoparticles. Journal of Membrane Science, 2017. **524**: p. 502-528.
176. Zhao, X., et al., Constructing Antifouling Hybrid Membranes with Hierarchical Hybrid Nanoparticles for Oil-in-Water Emulsion Separation. ACS omega, 2019. **4**(1): p. 2320-2330.
177. Vatanpour, V., et al., Enhancing the permeability and antifouling properties of cellulose acetate ultrafiltration membrane by incorporation of ZnO@ graphitic carbon nitride nanocomposite. Carbohydrate Polymers, 2021. **256**: p. 117413.
178. Mohammadnezhad, F., M. Feyzi, and S. Zinadini, A novel Ce-MOF/PES mixed matrix membrane; synthesis, characterization and antifouling evaluation. Journal of industrial and engineering chemistry, 2019. **71**: p. 99-111.

179. Vetrivel, S., et al., Cellulose acetate nanocomposite ultrafiltration membranes tailored with hydrous manganese dioxide nanoparticles for water treatment applications. Polymers for Advanced Technologies, 2019. **30**(8): p. 1943-1950.
180. Hong, D.Y., et al., Porous chromium terephthalate MIL-101 with coordinatively unsaturated sites: surface functionalization, encapsulation, sorption and catalysis. Advanced Functional Materials, 2009. **19**(10): p. 1537-1552.
181. Babaee, S., et al., Synthesis of metal–organic frameworks MIL-101 (Cr)-NH2 containing phosphorous acid functional groups: Application for the synthesis of N-Amino-2-pyridone and pyrano [2, 3-c] pyrazole derivatives via a cooperative vinylogous anomeric-based oxidation. ACS omega, 2020. **5**(12): p. 6240-6249.
182. Yoo, D.K., et al., Metal-organic framework MIL-101 loaded with polymethacrylamide with or without further reduction: Effective and selective CO2 adsorption with amino or amide functionality. Chemical Engineering Journal, 2020. **380**: p. 122496.
183. Nightingale Jr, E., Phenomenological theory of ion solvation. Effective radii of hydrated ions. The Journal of Physical Chemistry, 1959. **63**(9): p. 1381-1387.
184. Xu, S., et al., Polyphenol engineered membranes with dually charged sandwich structure for low-pressure molecular separation. Journal of Membrane Science, 2020. **601**: p. 117885.
185. Thong, Z., et al., Novel nanofiltration membranes consisting of a sulfonated pentablock copolymer rejection layer for heavy metal removal. Environmental science & technology, 2014. **48**(23): p. 13880-13887.
186. Peydayesh, M., T. Mohammadi, and O. Bakhtiari, Water desalination via novel positively charged hybrid nanofiltration membranes filled with hyperbranched polyethyleneimine modified MWCNT. Journal of industrial and engineering chemistry, 2019. **69**: p. 127-140.
187. Al Lafi, A.G., B. Assfour, and T. Assaad, Metal Organic Framework MIL-101 (Cr): Spectroscopic Investigations to Reveal Iodine Capture Mechanism. Journal of Inorganic and Organometallic Polymers and Materials, 2020. **30**(4): p. 1218-1230.
188. Zhou, Z., et al., Flexible and mechanically-stable MIL-101 (Cr)@ PFs for efficient benzene vapor and CO 2 adsorption. RSC advances, 2015. **5**(114): p. 94276-94282.
189. Jouyandeh, M., et al., Synthesis, characterization, and high potential of 3D metal–organic framework (MOF) nanoparticles for curing with epoxy. Journal of Alloys and Compounds, 2020. **829**: p. 154547.
190. Mubashir, M., et al., Efficient CO2/N2 and CO2/CH4 separation using NH2-MIL-53 (Al)/cellulose acetate (CA) mixed matrix membranes. Separation and Purification Technology, 2018. **199**: p. 140-151.
191. Lim, C.-R., S. Lin, and Y.-S. Yun, Highly efficient and acid-resistant metal-organic frameworks of MIL-101 (Cr)-NH2 for Pd (II) and Pt (IV) recovery from acidic solutions: Adsorption experiments, spectroscopic analyses, and theoretical computations. Journal of hazardous materials, 2020. **387**: p. 121689.
192. Butler, E., C. Petit, and A. Livingston, Poly (piperazine trimesamide) thin film nanocomposite membrane formation based on MIL-101: Filler aggregation and interfacial polymerization dynamics. Journal of Membrane Science, 2020. **596**: p. 117482.
193. Majeed, S., et al., Multi-walled carbon nanotubes (MWCNTs) mixed polyacrylonitrile (PAN) ultrafiltration membranes. Journal of Membrane Science, 2012. **403**: p. 101-109.
194. Kamari, S. and A. Shahbazi, High–performance nanofiltration membrane blended by Fe3O4@ SiO2–CS bionanocomposite for efficient simultaneous rejection of salts/heavy metals ions/dyes with high permeability, retention increase and fouling decline. Chemical Engineering Journal, 2021. **417**: p. 127930.
195. Abdi, G., et al., Removal of dye and heavy metal ion using a novel synthetic polyethersulfone nanofiltration membrane modified by magnetic graphene oxide/metformin hybrid. Journal of membrane science, 2018. **552**: p. 326-335.

196. Ayyaru, S. and Y.-H. Ahn, Application of sulfonic acid group functionalized graphene oxide to improve hydrophilicity, permeability, and antifouling of PVDF nanocomposite ultrafiltration membranes. Journal of membrane science, 2017. **525**: p. 210-219.
197. Elimelech, M., et al., Role of membrane surface morphology in colloidal fouling of cellulose acetate and composite aromatic polyamide reverse osmosis membranes. Journal of membrane science, 1997. **127**(1): p. 101-109.
198. Zhang, Q., et al., Multivariable sieving and hierarchical recognition for organic toxics in nonhomogeneous channel of MOFs. Chem, 2019. **5**(5): p. 1337-1350.
199. Bhattacharjee, S., C. Chen, and W.-S. Ahn, Chromium terephthalate metal–organic framework MIL-101: synthesis, functionalization, and applications for adsorption and catalysis. RSC advances, 2014. **4**(94): p. 52500-52525.
200. Zhu, J., et al., Fabrication of a novel "loose" nanofiltration membrane by facile blending with Chitosan–Montmorillonite nanosheets for dyes purification. Chemical Engineering Journal, 2015. **265**: p. 184-193.
201. Zhang, H., et al., Carboxyl-functionalized graphene oxide polyamide nanofiltration membrane for desalination of dye solutions containing monovalent salt. Journal of Membrane Science, 2017. **539**: p. 128-137.
202. Kamari, S. and A. Shahbazi, Biocompatible Fe3O4@ SiO2-NH2 nanocomposite as a green nanofiller embedded in PES–nanofiltration membrane matrix for salts, heavy metal ion and dye removal: Long–term operation and reusability tests. Chemosphere, 2020. **243**: p. 125282.
203. Gregor, H.P., Gibbs-Donnan equilibria in ion exchange resin systems. Journal of the American Chemical Society, 1951. **73**(2): p. 642-650.
204. Sperelakis, N., Gibbs-Donnan equilibrium potentials, in Cell Physiology Source Book. 2001, Elsevier. p. 243-247.
205. Afonso, M.D. and M.N. de Pinho, Transport of MgSO4, MgCl2, and Na2SO4 across an amphoteric nanofiltration membrane. Journal of membrane science, 2000. **179**(1-2): p. 137-154.
206. Huang, S., et al., Poly (1-amino-5-chloroanthraquinone): highly selective and ultrasensitive fluorescent chemosensor for ferric ion. Journal of fluorescence, 2013. **23**(4): p. 621-627.
207. Liu, C., et al., High-performance nanofiltration membrane with structurally controlled PES substrate containing electrically aligned CNTs. Journal of Membrane Science, 2020. **605**: p. 118104.
208. Li, L., et al., Recovery of linseed oil dispersed within an oil-in-water emulsion using hydrophilic membrane by rotating disk filtration system. Journal of Membrane Science, 2009. **342**(1-2): p. 70-79.
209. Nguyen, V.H.T., et al., One-pot preparation of alumina-modified polysulfone-graphene oxide nanocomposite membrane for separation of emulsion-oil from wastewater. Journal of Nanomaterials, 2020. **2020**.
210. Somerville, H., et al., Environmental effect of produced water from North Sea oil operations. Marine Pollution Bulletin, 1987. **18**(10): p. 549-558.
211. Fakhru'l-Razi, A., et al., Review of technologies for oil and gas produced water treatment. Journal of hazardous materials, 2009. **170**(2-3): p. 530-551.
212. He, K., et al., Cleaning of oil fouling with water enabled by zwitterionic polyelectrolyte coatings: overcoming the imperative challenge of oil–water separation membranes. ACS nano, 2015. **9**(9): p. 9188-9198.
213. Kang, W., et al., Flocculation, coalescence and migration of dispersed phase droplets and oil–water separation in heavy oil emulsion. Journal of Petroleum Science and Engineering, 2012. **81**: p. 177-181.
214. Fragouli, D. and A. Athanassiou, Graphene heaters absorb faster. Nature Nanotechnology, 2017. **12**(5): p. 406-407.

215. Teh, C.Y., et al., Recent advancement of coagulation–flocculation and its application in wastewater treatment. Industrial & Engineering Chemistry Research, 2016. **55**(16): p. 4363-4389.
216. Zhang, W., et al., Salt-induced fabrication of superhydrophilic and underwater superoleophobic PAA-g-PVDF membranes for effective separation of oil-in-water emulsions. Angewandte Chemie International Edition, 2014. **53**(3): p. 856-860.
217. Etchepare, R., et al., Separation of emulsified crude oil in saline water by dissolved air flotation with micro and nanobubbles. Separation and Purification Technology, 2017. **186**: p. 326-332.
218. Zhong, J., X. Sun, and C. Wang, Treatment of oily wastewater produced from refinery processes using flocculation and ceramic membrane filtration. Separation and Purification Technology, 2003. **32**(1-3): p. 93-98.
219. Tang, H., et al., Surface modification to fabricate superhydrophobic and superoleophilic alumina membranes for oil/water separation. Energy & Fuels, 2018. **32**(3): p. 3627-3636.
220. Hubadillah, S.K., et al., Superhydrophilic, low cost kaolin-based hollow fibre membranes for efficient oily-wastewater separation. Materials Letters, 2017. **191**: p. 119-122.
221. Padaki, M., et al., Membrane technology enhancement in oil–water separation. A review. Desalination, 2015. **357**: p. 197-207.
222. Maguire-Boyle, S.J. and A.R. Barron, A new functionalization strategy for oil/water separation membranes. Journal of Membrane Science, 2011. **382**(1-2): p. 107-115.
223. Xue, Z., et al., A novel superhydrophilic and underwater superoleophobic hydrogel-coated mesh for oil/water separation. Advanced Materials, 2011. **23**(37): p. 4270-4273.
224. Cheng, Q., et al., Facile fabrication of superhydrophilic membranes consisted of fibrous tunicate cellulose nanocrystals for highly efficient oil/water separation. Journal of Membrane Science, 2017. **525**: p. 1-8.
225. Wang, S., M. Li, and Q. Lu, Filter paper with selective absorption and separation of liquids that differ in surface tension. ACS Applied Materials & Interfaces, 2010. **2**(3): p. 677-683.
226. Lahiere, R.J. and K.P. Goodboy, Ceramic membrane treatment of petrochemical wastewater. Environmental progress, 1993. **12**(2): p. 86-96.
227. Zou, D., et al., One step co-sintering process for low-cost fly ash based ceramic microfiltration membrane in oil-in-water emulsion treatment. Separation and Purification Technology, 2019. **210**: p. 511-520.
228. Ohya, H., et al., Effects of pore size on separation mechanisms of microfiltration of oily water, using porous glass tubular membrane. Journal of membrane science, 1998. **145**(1): p. 1-14.
229. Nandi, B., et al., Treatment of oily wastewater using low cost ceramic membrane: Comparative assessment of pore blocking and artificial neural network models. chemical engineering research and design, 2010. **88**(7): p. 881-892.
230. Gao, N., et al., Improving the filtration performance of ZrO2 membrane in non-polar organic solvents by surface hydrophobic modification. Journal of membrane science, 2011. **375**(1-2): p. 276-283.
231. Zhao, Y., et al., Fouling and regeneration of ceramic microfiltration membranes in processing acid wastewater containing fine TiO2 particles. Journal of Membrane Science, 2002. **208**(1-2): p. 331-341.
232. Mueller, J., Y. Cen, and R.H. Davis, Crossflow microfiltration of oily water. Journal of Membrane Science, 1997. **129**(2): p. 221-235.
233. Hua, F., et al., Performance study of ceramic microfiltration membrane for oily wastewater treatment. Chemical Engineering Journal, 2007. **128**(2-3): p. 169-175.
234. Kang, G., et al., A novel method of surface modification on thin-film composite reverse osmosis membrane by grafting poly (ethylene glycol). Polymer, 2007. **48**(5): p. 1165-1170.

235. Zhang, T., et al., Zwitterionic monolayer grafted ceramic membrane with an antifouling performance for the efficient oil–water separation. Chinese Journal of Chemical Engineering, 2021.
236. Shi, Q., et al., Poly (p-phenylene terephthamide) embedded in a polysulfone as the substrate for improving compaction resistance and adhesion of a thin film composite polyamide membrane. Journal of Materials Chemistry A, 2017. **5**(26): p. 13610-13624.
237. Chang, Q., et al., Hydrophilic modification of Al2O3 microfiltration membrane with nano-sized γ-Al2O3 coating. Desalination, 2010. **262**(1-3): p. 110-114.
238. Zhou, J.-e., et al., Separation of stable oil–water emulsion by the hydrophilic nano-sized ZrO2 modified Al2O3 microfiltration membrane. Separation and Purification Technology, 2010. **75**(3): p. 243-248.
239. Raman, A.K.Y., et al., Emulsion stability of surfactant and solid stabilized water-in-oil emulsions after hydrate formation and dissociation. Colloids and Surfaces A: Physicochemical and Engineering Aspects, 2016. **506**: p. 607-621.
240. Mahmodi, G., et al., Improving antifouling property of alumina microfiltration membranes by using atomic layer deposition technique for produced water treatment. Desalination, 2022. **523**: p. 115400.
241. Sadeghi, I., et al., Surface modification of polyethersulfone ultrafiltration membranes by corona air plasma for separation of oil/water emulsions. Journal of Membrane Science, 2013. **430**: p. 24-36.
242. Rashad, M., et al., A novel monolithic mullite microfiltration membrane for oil-in-water emulsion separation. Journal of Membrane Science, 2021. **620**: p. 118857.
243. Wu, H., et al., Treatment of Oily Wastewaters by Highly Porous Whisker-constructed Ceramic Membranes: Separation Performance and Fouling Models. Water Research, 2022: p. 118042.

VITA

Diako Mahmodi

Candidate for the Degree of

Doctor of Philosophy

Dissertation: MICROPOROUS MEMBRANES FOR OIL-WATER SEPARATION AND DESALINATION

Major Field: Chemical Engineering

Biographical:

Education:

Completed the requirements for the Doctor of Philosophy in Chemical Engineering at Oklahoma State University, Stillwater, Oklahoma in December 2022.

Completed the requirements for the Master of Science in Chemical Engineering at Razi University, Kermanshah, Iran in 2011.

Completed the requirements for the Bachelor of Science in Chemical Engineering at Amir Kabir University of Technology, Tehran, Iran in 2009.

Experience:

Graduate Research and Teaching Assistant, Oklahoma State University (Jan 2019 – Oct 2022)

Research AND Development Intern, IX power clean water Golden, CO, US (Jan 2022 – July 2022).

Shift Supervisor, Water & Wastewater Treatment Plant, Erbil Combined Cycle Power Plnat, Kurdistan Regional Government. (June 2013- April 2017)

Professional Memberships:

American Institute of Chemical Engineers (AIChE).